The Chemical Structure, Composition, Extent of Mixing, and the Origin of Heterogeneities in the Earth's Mantle

The Chemical Structure, Composition, Extent of Mixing, and the Origins of Heterogeneities in the Earth's Mantle

A dissertation presented

by

Eugenia Hyung

to

The Department of Earth and Planetary Sciences

In partial fulfillment of the requirements
for the degree of
Doctor of Philosophy
in the subject of
Earth and Planetary Sciences

Harvard University
Cambridge, Massachusetts

July, 2018

Dissertation Advisor: Stein. B. Jacobsen Eugenia Hyung

The Chemical Structure, Composition, Extent of Mixing and the Origins of Heterogeneities in the Earth's Mantle

Abstract

Formation of chemical heterogeneities and the extent of mixing in the mantle are relevant questions to understanding large scale processes that dominate the bulk silicate Earth, which can be addressed using different methods of analyses. A shear wave velocity model was employed to evaluate the composition of the lower mantle. The model takes into account the effect of minor elements i.e., the Ca-bearing lower mantle phase and the effect of Al on Fe-Mg partitioning between bridgmanite and ferropericlase. The fractionation of the lithophile ^{176}Lu-^{176}Hf and ^{147}Sm-^{143}Nd systems in a hypothetical magma ocean was also calculated to constrain the composition of the lower mantle. These two methods demonstrate that the lower mantle composition is likely pyrolitic, and that the mantle is not chemically stratified at the 660-km discontinuity. The reproducibility of ^{142}Nd/^{144}Nd measurements was improved to $2\sigma = \pm 1.6$ ppm (from $2\sigma = \pm 5$–6 ppm). The measurements demonstrate resolvable variability in a modern day mid-ocean ridge basalt (MORB) sample, implying preservation of mantle heterogeneity for >4 Gyr. The distribution and variability of ^{142}Nd/^{144}Nd throughout time, through stochastic modeling, suggest the presence of plate tectonics already operating in the Hadean. Mg isotope measurements and major element analysis of alkalic rocks from the Oslo Rift, show these HIMU (high time-integrated ^{238}U/^{204}Pb) basalts to be from the peridotitic mantle, as the first strong evidence against HIMU compositions as a tracer of recycled oceanic crust. In addition, the major element compositions and Mg isotopes suggest the involvement of CO_2 sourced from the indigenous

mantle, as opposed to carbonated lithologies or carbonatite metasomatism. Modeling of the time scale of homogenization of the late veneer and the evolution of $^{182}W/^{184}W$ isotope signatures of the terrestrial mantle show that the late veneer signature takes a long time to homogenize, during which it is possible to sample the mantle $^{182}W/^{184}W$ values post-core formation into the Archean. It is also possible to resolve the distribution of $^{182}W/^{184}W$ and $^{142}Nd/^{144}Nd$ isotope variations with the same mixing rate. The $^{182}W/^{184}W$ and $^{142}Nd/^{144}Nd$ distribution in the mantle are consistent with the same stirring rate that applies to the long-lived radiogenic isotope systems.

TABLE OF CONTENTS

Acknowledgements

"It takes a village…"

Much like a child, similarly behind an exhausted Ph.D. graduate student at the finishing stages of his/her education is most often a large body of support from various directions that has persisted for many years. I would like to acknowledge those without whom this dissertation would not have been possible.

I would like to dedicate my dissertation to Rick O'Connell (1941–2015), which I believe would have had enjoyed the work that came out of this thesis. His work and research interests were a source of inspiration and encouragement regarding my own questions about the Earth's mantle. I treasure the memories I have of him, particularly his notoriety for falling asleep during seminars and quals exams and waking up at the end to ask the most piercing questions, as well as his sense of humor and his kind and gentle heart and presence. His support and encouragement during the early stages of my work meant the world to me.

I would like to acknowledge my lab and officemates, Shichun, Robert, Rita, Jenny, Kun, Hongming, Fata, Li, Chris, Ben, Yaya, and Zack, with whom I had the privilege of learning from and sharing fun times. I will remember and cherish the conversations had and events celebrated, whether it be paddle ball challenges, field trips, cabin and Cape Cod outings, as well as office birthday parties. In addition, I would like to acknowledge my close department friends, with whom I have had the privilege of sharing both the happy and sad times with, these being Maria, Uyanga, JT, Sunny, and Jocelyn.

I was privileged with the best roommates in the world during my Ph.D. I am grateful to have known Ximin, Ankita, Sabrina, Mili and Li, for their support, company, consideration, big hearts, generosity, and kindness throughout the years.

I would like to acknowledge Chenoweth and Sarah, who are indispensable to the community, having been supportive and knowledgeable in navigating administrative issues, on top of always willing to lend an ear during tough challenges. I especially owe it to Paul Kelly for being supportive with providing funding for certain lab equipment in case of emergency situations and involvement with the prompt restoration of the cosmochemistry clean lab, especially during the multiple floods that occurred on the second floor of Hoffman during my time! I would also like to thank Tracey Newman of the Graduate Student Financial Aid office for her encouragement and support, in sorting out funding issues with fellowships, and helping with my medical bills.

I thank my committee member Shichun Huang, for playing the role of a hands-on mentor especially during the early stages of my Ph.D. years, providing support through generous advice, encouragement, direction, and perspective. I thank Jerry X. Mitrovica, who has been generous with his time and support in times of difficulty, with whom I have enjoyed company through his presence in classes, and light-hearted sense of humor. I express gratitude to my fourth committee member, Dimitar Sasselov for his helpful feedback on the contents of this thesis. In addition, I would like to extend a special thanks to Misha Petaev, who was a part of my "internal peer review" committee during the developing stages of my ideas and work especially at the beginning of my graduate school career, as well as being a source of wisdom and support, not to mention good tea.

I thank my parents who have been supportive for offering various pieces of life advice, and also in lending an ear whenever I needed to rant about difficult a scientific problem! I thank my brother David for his kind words and confidence in me, and my sister Soojinn for fun conversations.

Finally, I have my advisor, Stein B. Jacobsen to thank, who with a big heart and infinite patience, has been a source of encouragement and unwavering support. I learned immensely from not only from his scientific acumen and endless body of knowledge, but also his capability to maintain calmness throughout what may have otherwise been a frantic Ph.D.! I want to thank him for helping me learn that it is worthwhile to stand up for an important idea or difficult endeavor, even if the rest of the world does not agree.

CHAPTER 1

Introduction

The Earth's mantle, sandwiched between the crust and the core, takes up 80% of the Earth by volume. Understanding the chemical structure and evolution of the silicate mantle is integral to understanding the evolution of the crust, and the differentiation of the core. Furthermore, the study of the terrestrial mantle is tied to understanding the origins of the Earth, from its state early in solar system history, and its evolution throughout time. Constraining chemical heterogeneities on a large scale is relevant to understanding what sources and mechanisms have contributed to their development, and under what the conditions the Earth was subjected to that generated such features. The problem of mantle mixing is tied to the mode of convection that must have been dominated during the evolution of the Earth, and understanding the conditions necessary to give rise to the diversity of geological conditions on the Earth. The delivery of accretionary material to the Earth after core formation is relevant to the delivery of volatiles such as water. All of these problems have implications for understanding the origins of life.

One enduring problem with respect to the large-scale chemical structure of the mantle, has been of understanding whether the Earth's mantle has been chemically stratified at the 660-km discontinuity, like a layered cake. The upper mantle is widely presumed to be pyrolitic, but the bulk composition of the Earth's lower mantle has been a subject of debate. A chemically stratified mantle on such a large scale has implications for understanding the early state of the Earth; whether there was an early magma ocean, to what extent its depth

extended, and whether there are features still preserved through layered-mantle convection, or whether whole-mantle convection has mixed away early features.

Tools such as the short-lived ^{146}Sm-^{142}Nd isotope system are relevant to the problem of exploring the extent of mixing in the mantle. With a short half-life of 68 or 103 Myr, the lithophile ^{146}Sm-^{142}Nd system can be used as a tracer of silicate differentiation that has occurred within the first 500 Myr of solar system history. Positive and negative anomalies well into the Archean have been discovered as evidence of this early differentiation. The preservation of ^{142}Nd/^{144}Nd signatures well beyond after the extinction of ^{146}Sm, serves as a tracer for the extent of mixing in the mantle.

Modern-day ^{142}Nd/^{144}Nd anomalies were previously unresolved at 2σ = 5–6 ppm external precision. It was recognized that the development of ultra-high precision measurements of ^{142}Nd/^{144}Nd isotope ratios on the thermal ionization mass spectrometer, had the potential of resolving whether there are traces of Hadean differentiation that are still preserved at present day for over 4 billion years. In addition, understanding the distribution of ^{42}Nd/^{144}Nd anomalies with respect to time helps elucidate the state of mantle convection in the early part of Earth's history, on whether the isotope distributions would be more indicative of sluggish mixing, stagnant lid convection, or plate tectonics.

HIMU (high time-integrated ^{238}U/^{204}Pb isotope content), one of the four major geochemical components along with EM1, EMII (enriched mantle I, II), and DMM (depleted MORB mantle), is an isotopic component that is traditionally understood to be from recycled oceanic crust. Understanding HIMU is tied into tracing the extent of involvement of recycled material in the production of geochemical heterogeneities, as consequences of subduction and convection. It is also relevant to quantifying the extent of

contribution of recycled material to the genesis of chemical heterogeneities, and formation of alkalic rocks with HIMU signatures at ridge spreading as well as continental rift zones. The extent of the involvement of recycled oceanic material in the genesis of chemical heterogeneities is in need of better constraints.

Highly siderophile ("iron-loving") element (HSE) are present in elevated abundances in chondritic proportions in the terrestrial mantle, in conflict with silicate-metal partition coefficients of HSEs from high-pressure experiments, as the sequestration of HSEs in the Earth's core is predicted. Such a discrepancy has led to the hypothesis of a "late veneer," accretionary material that is thought to have been added and thoroughly mixed with the terrestrial mantle, which would have comprised 0.2–0.9% of the Earth's mantle. A late veneer roughly CI meteorite composition could also have delivered the volatiles into the Earth's atmosphere and oceans.

^{182}Hf decays into ^{182}W with a short half-life of 8.9 Myrs. While ^{182}Hf is lithophile, ^{182}W is siderophile, making it an ideal tracer for understanding the timing of core-formation. Owing to the moderately siderophile nature of W, the delivery of late veneer is expected to have affected the bulk silicate Earth ^{182}W/^{184}W ratio and W concentration. The distribution of the W isotope data with respect to time however, is not well understood. Modeling the time scale of mixing of the late veneer may clarify the early conditions of late veneer delivery, and the relation of measured ^{182}W/^{184}W ratios, to the mixing of the mantle.

This work is presented in four chapters. Chapter 2 is already published in *Earth and Planetary Sciences Letters* and tests whether the terrestrial mantle is chemically stratified on the scale of the upper and lower mantle volumes. The additional collaborators who have been involved in this study include Shichun Huang, Michail Petaev, and Stein B. Jacobsen.

Chapter 3 has been submitted and is under review in *Nature Communications.* The study tests whether the modern-day Earth still preserves heterogeneities from silicate differentiation events produced in the Hadean with improved $^{142}Nd/^{144}Nd$ measurements for modern day samples. In addition, the data distribution of $^{142}Nd/^{144}Nd$ isotopes throughout time is used to infer the style of tectonics in the Hadean. The main collaborator who has been involved in this study is Stein B. Jacobsen. Chapter 4 has been submitted to *Proceedings of the National Academy of Sciences*. The study pinpoints the source of highly alkalic HIMU basalts, a geochemical component traditionally understood be a tracer of oceanic crust. Additional collaborators who have been involved in this study include Fatemeh Sedaghatpour, Bjorn T. Larsen, Else-Ragnhild Neumann, and Stein B. Jacobsen. Chapter 5 tests the evolution and distribution of $^{182}W/^{184}W$ isotopes in relation to the terrestrial mantle post-core formation and the delivery of the late veneer.

Through addressing such topics, I elucidate extent of mixing in the terrestrial mantle and its relationship to chemical heterogeneities through time.

CHAPTER 2

Is the mantle chemically stratified? Insights from sound velocity modeling and isotope evolution of an early magma ocean

This chapter has been published in *Earth and Planetary Science Letters.* The collaborators that were involved include (in the order of authorship) Shichun Huang, Michail I. Petaev, and Stein B. Jacobsen.

Abstract

The upper mantle is widely accepted to be pyrolitic, but the bulk composition of the lower mantle remains highly disputed. Recent modeling of the lower mantle shear wave velocity profile has suggested that the lower mantle is enriched in bridgmanite, therefore implying a higher Si/Mg than that of the upper mantle. We improve upon such modeling by taking into account Ca-perovskite and considering the distribution of Fe between bridgmanite and ferropericlase, more appropriate for Al-bearing systems. Using available experimental data, we derive a means to constrain Al-Fe-partitioning for bridgmanite and ferropericlase, constrain suitable values for the lower mantle, and apply these to lower mantle shear wave velocity calculations. We also model chemical fractionations of the ^{147}Sm-^{143}Nd and ^{176}Lu-^{176}Hf systems induced by a crystallizing magma ocean that would produce a putative Si-enriched lower mantle. The comparison of the calculated $^{143}Nd/^{144}Nd$ and $^{176}Hf/^{177}Hf$ signatures with those of the terrestrial array shows that a Si-enriched lower mantle, if ever formed, no longer exists. Calculations that consider the effects of minor chemical components such as Ca and Al suggest that the lower mantle shear wave velocities can resolve PREM for a pyrolitic composition to within 1%. Both mineralogical

calculations and geochemical magma ocean modeling support the idea that the Earth's lower mantle is likely pyrolitic and that the mantle as a whole need not be chemically stratified.

1.Introduction

The solid Earth is composed of three major chemical layers–the crust, the mantle, and the core. These features were first identified by analyzing seismic waves generated by large-scale earthquakes, penetrating into the interior of the Earth (e.g., Williamson and Adams, 1923). Later, when the physical properties of putative inner Earth materials were measured in high pressure and temperature experiments, inner Earth seismic wave velocities and density profiles were linked to the chemical compositions of these layers (e.g., Birch, 1952).

The silicate mantle is the Earth's volumetrically largest division. Its chemical composition and structure are a constant subject of inquiry and debate as they tie into many issues pertaining to the origin of the Earth and its evolution (e.g., Javoy et al., 2010). One of the most prominent seismic features of the mantle is the 660-km discontinuity, characterized by a sharp jump in seismic velocity. This discontinuity, which serves as the boundary between the upper and lower mantles, has traditionally been attributed to the temperature and pressure-induced breakup of ringwoodite, $(Mg,Fe)_2SiO_4$, into bridgmanite, $(Mg,Fe)SiO_3$, (formerly referred to as "Mg-silicate-perovskite"), and ferropericlase, (Mg,Fe)O (Ito and Takahashi, 1989).

There is yet no consensus on whether this discontinuity is also a chemical boundary (e.g., Irifune et al., 2010; Murakami et al., 2012), which would imply different compositions for the lower and upper mantles. The upper mantle composition is well established from

samples of mid-ocean ridge volcanism and mantle peridotites, and is widely presumed to be pyrolitic (Ringwood, 1962). Pyrolite, a theoretical composition calculated as three parts peridotite and one part normal mid-ocean ridge basalt (Ringwood, 1962), is depleted in Si compared to chondrites. Chondrites are often considered to be the building blocks of the Earth. If the bulk Earth has a CI-chondritic Si/Mg ratio, then the compensation for the apparent depletion of Si in the upper mantle is explained either by sequestering of some Si into the core (e.g., Allegre et al., 1995; Georg et al., 2007), or having a higher Si/Mg ratio in the lower mantle (e.g., Taylor and McLennan, 1985), or both.

Such a chemical stratification in the mantle, if it exists, would have most likely been caused by the gravitational settling of dense bridgmanite crystals during the solidification of magma ocean not long after the Earth formation (Agee and Walker, 1988). The preservation of such a chemically layered mantle throughout billions of years would imply a lack of material transport between the upper and lower mantles throughout the history of the Earth. Although seismic tomography has revealed slabs penetrating the 660-km discontinuity (van der Hilst et al., 1997), the extent of material exchange between the upper and lower mantles remains unclear.

The composition of the lower mantle has been evaluated by modeling sound velocity profiles using experimentally derived physical properties of mantle minerals under proper *P-T* conditions (Lee et al., 2004; Stixrude et al., 1992). However, in most experiments, the chemical composition of the lower mantle is approximated by the Fe-Mg-Si-O system, neglecting the less abundant major elements such as Al and Ca. The effect of Al on the shear properties of bridgmanite, having only been explored in the past decade (Jackson, 2004; Murakami et al., 2012), has profound implications for interpreting the lower mantle

composition. Using experimental data obtained under lower mantle *P-T* conditions, recent modeled seismic shear wave velocities of a pyrolitic lower mantle (Murakami et al., 2012) were found to have large discrepancies from the shear wave velocities of the 1D seismic profile, PREM (Dziewonski and Anderson, 1981). Specifically, their modeled shear wave velocity profile for a pyrolitic lower mantle was much lower than PREM (~3% offset), that was resolved by increasing the bridgmanite/ferropericlase ratio assumed in the lower mantle compared to the pyrolitic composition.

The approach of Murakami et al., (2012) neglects the contribution of a Ca-bearing phase and the effect of Al on Fe-Mg partitioning between bridgmanite and ferropericlease, which in turn, affects the sound wave speeds of these minerals. Here, we model the shear wave velocities of the lower mantle, taking these effects into account. The pyrolitic mantle contains ~3–4 wt% CaO (e.g., McDonough and Sun, 1995), which in the lower mantle resides in Ca-perovskite, $CaSiO_3$, occurring alongside two other minerals, bridgmanite and ferropericlase. Although the shear properties of Ca-perovskite have not been measured experimentally, *ab initio* calculations (Karki and Crain, 1998) of cubic Ca-perovskite have demonstrated high shear velocities which can potentially resolve the discrepancy between a pyrolitic lower mantle and observed seismic wave velocities.

Calculations of lower mantle sound wave velocities usually consider bridgmanite and ferropericlase with Fe-Mg partitioning characteristic of Al-free systems (e.g., Zhang et al., 2013). Al, however, residing exclusively in bridgmanite, affects Fe-Mg partitioning to a substantial degree. Although Al is reported to increase the amount of Fe in bridgmanite due to the coupled substitution of (Fe^{3+} and Al^{3+}) for (Mg^{2+} and Si^{4+}) (Wood and Rubie, 1996), the extreme variability in the data (Fig. 1) has made the subject controversial. In particular,

relations among pressure, temperature and Fe-Mg partitioning behavior in coexisting Al-bearing bridgmanite and ferropericlase have so far remained unclear. Another possible complication is the spin transition occurring in ferropericlase, a high pressure effect involving a change in an electron configuration from high spin to low, which subsequently affects both the bulk and shear properties of ferropericlase. As Fe-Mg partitioning between Al-bridgmanite and ferropericlase in the lower mantle can affect shear wave velocity calculations, there is a necessity to critically assess and analyze the available experimental data. Through such an analysis, we present a statistically significant correlation that is capable of predicting K_D values, use this relation to derive K_D suitable for the lower mantle, and apply these to shear wave velocity calculations.

In addition, our study also explores the fractionation of lithophile trace elements in a putative Si-enriched lower mantle that would have formed in a differentiating magma ocean, by taking advantage of primordial fractionation effects in the ^{176}Lu-^{176}Hf and ^{147}Sm-^{143}Nd radiogenic isotope systems between a silicate melt and high-pressure lower mantle phases.

Using approaches from mineral physics and geochemistry, we evaluate the likelihood of a chemically stratified mantle, with the lower mantle being enriched in Si compared to the upper mantle.

2.Methods

2.1 Shear wave velocity modeling

Modeling a seismic velocity profile of a planetary layer such as the lower mantle involves a series of calculations for different depths of the layer. Each step calculates the

compound shear wave velocities for a mineral aggregate representing a bulk chemical composition at a given pressure and temperature. For the calculations of the aggregate shear wave velocity of a pyrolitic lower mantle, the mineral proportions of lower mantle minerals (~77.5 vol% bridgmanite [Al-(Mg,Fe)SiO_3] ~15 vol% ferropericlase [(Mg,Fe)O], and ~7.5 vol% Ca-perovskite [$CaSiO_3$]) (e.g., Irifune, 1994) are used. Since the amount of Fe in ferropericlase or bridgmanite affects the wt% proportions of these minerals, we consider minor variations in the volume and weight proportions of lower mantle minerals corresponding to different K_D values, to account for small volume and density changes that Fe inflicts for each corresponding phase. The lower mantle Fe/(Fe+Mg) is set to 0.107 (McDonough and Sun, 1995), similar to earlier estimates by Green et al., (1979) and Jagoutz et al., (1979).

For the calculation of the shear wave velocity profile of the lower mantle, we utilize the third-order Eulerian finite-strain equation (Stixrude and Lithgow-Bertelloni, 2005) to calculate shear modulus (G), where the non-thermal portion is expressed as follows:

$$G = (1 + 2f)5/2[G_0 + (3K_{S0}G'_0 - 5G_0)f + (6Ks_0G'_0 - 24Ks_0 - 14G_0 + 9/2Ks_0K'_0)f^2] \quad (1)$$

Here, G_0 is the shear modulus at zero pressure, G'_0 is the pressure derivative of the shear modulus, K_0, the bulk modulus, and K'_0, the pressure derivative of the bulk modulus. This expression is thermodynamically self-consistent to f^2, where f, the finite strain, is defined as:

$$f = \frac{1}{2}\left[\left(\frac{\rho}{\rho_0}\right)^{\frac{2}{3}} - 1\right] \quad (2)$$

where ρ is density at corresponding depth, and ρ_0 is the density at zero pressure. K_{S0} is the isentropic bulk modulus at zero pressure:

$$K_{S0} = K_{T0}(1 + \alpha_0 \gamma_0 T). \qquad (3)$$

Here, T is the temperature at ambient pressure; K_{T0}, the isothermal bulk modulus; α_0, the thermal expansion coefficient; and γ_0, the Grüneisen parameter. Temperature corrections for shear modulus are made using linear projections (e.g., Anderson, 1989; Deschamp and Trampert, 2002). We adopted the Voigt-Reuss Hill averaging method (Hill, 1952) for the aggregate shear modulus of Mg-perovskite, ferropericlase, and Ca-perovskite of the lower mantle. Model calculations are performed along an adiabatic geotherm (Brown and Shankland, 1981).

For the shear properties (G, G') of bridgmanite, we use experimentally derived values from Murakami et al., (2012), which were used to argue for a Si-enriched lower mantle. The Fe-content in bridgmanite has been experimentally shown to have no bearing on its shear modulus (Chantel et al., 2012). In contrast, the shear properties of ferropericlase are affected by Fe. When calculating the change in the shear properties of ferropericlase with respect to its Fe/Mg ratio, we refer to the studies of Jacobsen et al., (2002) and Murakami et al., (2012). The pressure derivatives of the shear modulus (G') in the original experiments are derived using the second order Eulerian finite-strain equation (Davies and Dziewonski, 1975). For internal consistency in calculations, G' is re-derived using the third order expansion of the Eulerian finite strain equation (Stixrude and Lithgow-Bertelloni, 2005) by

refitting the raw data if reported, or refitting synthetic data generated using the published elastic constants as described in the footnote of Table 1. As there are no experimental data on the shear properties of Ca-perovskite, following Matas et al., (2007), we use *ab initio* calculations of Karki and Crain (1998).

2.2 Deriving K_D: finding a correlation between different chemical components

The partitioning of Mg and Fe between bridgmanite (pv) and ferropericlase (fp) in Al-free systems is described by the following reaction:

$$MgSiO_3(pv) + FeO(fp) \leftrightarrow FeSiO_3(pv) + MgO(fp) \qquad (4)$$

Where the partition coefficient, K_D, expresses the distribution of Fe and Mg between the two coexisting phases:

$$K_D = (X_{Fe}^{Pv} / X_{Mg}^{Pv}) / (X_{Fe}^{Fp} / X_{Mg}^{Fp}) \qquad (5)$$

Here, X_i^a is the mole fraction of component *i* in phase *a*. Typical K_D values in the Fe-Mg-Si-O systems range from 0.2 to 0.3 (Auzende et al., 2008; Kobayashi et al., 2005; Mao et al., 1997; Sakai et al., 2009), implying higher molar Fe/Mg ratios in ferropericlase than in bridgmanite. In Al-bearing systems, however, K_D values are higher by a factor of two or more and show large variations (Fig. 1). This phenomenon is largely attributed to the coupled substitution of (Fe^{3+} +Al^{3+}) for (Mg^{2+}+Si^{4+}) in bridgmanite, where Fe^{3+} is thought to

Table 1. Elastic constants used in shear wave velocity calculations

			Ferropericlase	
	Bridgmanite	Ca-pv	high spin	low spin
ρ_0 (g/cm^3)	set to vary*	4.23 (Ricolleau et al., 2009)	set to vary*	set to vary*
K_{T0} (GPa)	267.6(9) (Andrault et al., 2007; Fiquet et al., 2000)	244 (Ricolleau et al., 2009)	158 (Ricolleau et al., 2009) (fixed)	170 (Ricolleau et al., 2009) (fixed)
K'_0	3.78(3) (Fiquet et al., 2000)	4†	4†	4†
G_0 (GPa)	164(2) (Murakami et al., 2012)	165 (Karki and Crain, 1998)	varies*‡	varies*‡
G'_0	1.71(2)‡	2.50 (Karki and Crain, 1998)	varies*‡	varies*‡
α_0 (K^{-1})	2.2 x 10^{-5} (Funamori et al., 1996)	2.2x10^{-5} (Shim and Duffy, 2000)	3.15 x 10^{-5} (Dubrovinsky and Saxena, 1997)	
γ_0	1.5 (Murakami et al., 2012)	1.53 (Shim and Duffy, 2000)	1.5 (Murakami et al., 2012)	
$(dG/dT)_P$ (GPaK^{-1})	-0.020(1) (Murakami et al., 2012)	-0.023(6) (Cammarano et al., 2003)	-0.020(1) (Murakami et al., 2012)	

*Set to vary as a function of iron content: Mg-perovskite: $\rho_0 = 4.11+0.01$ x (100–Mg#)
Ferropericlase: calculated assuming $V_0 = 24.305$ g/cm^3 (Ricolleau et al., 2009) for both spin states, where V_0 is the volume at zero pressure.
†Fixed. See e.g., Ricolleau et al., 2009
‡G values are adapted from (Jacobsen et al., 2002) for the high spin state of ferropericlase, and (Murakami et al., 2012) for the low spin states of ferropericlase, which vary as a function of iron content. Suitable G' values for the third-order Eulerian finite strain equation are rederived by either performing a least squares fitting of existing data to the formulation of Stixrude ad Lithgow-Bertelloni (2005), where available, or fitting synthetic data that was generated by applying G and G' values to the second-order Eulerian finite strain equation (Davies and Dziewonski, 1975). All other elastic constants were chosen from the literature.

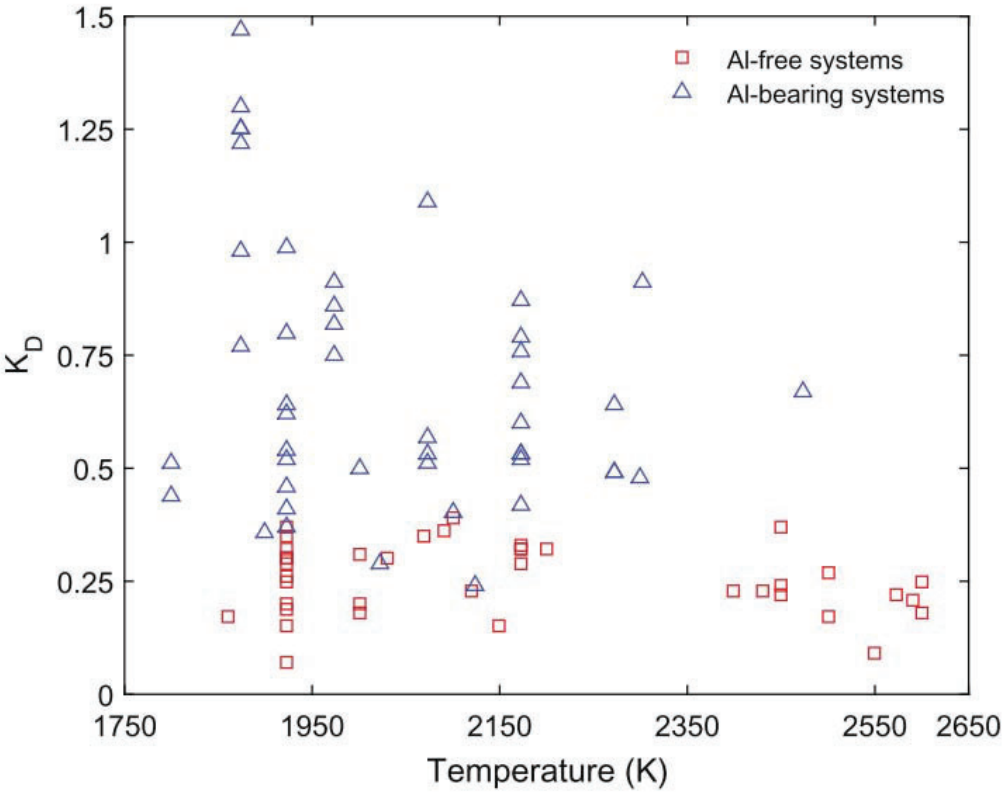
Al-free systems
Al-bearing systems
K_D
Temperature (K)
1.5
1.25
1
0.75
0.5
0.25
0
1750
1950
2150
2350
2550
2650

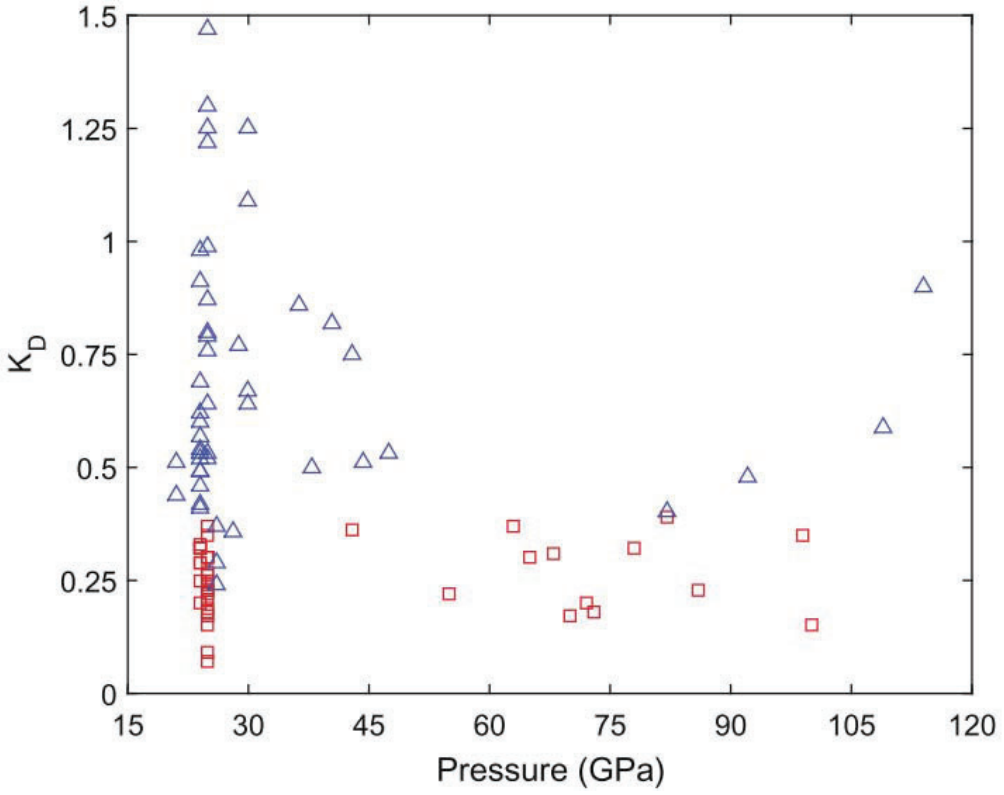
K_D
Pressure (GPa)
1.5
1.25
1
0.75
0.5
0.25
0
15
30
45
60
75
90
105
120

Figure 1. Variations of K_D values with temperature and pressure. Blue, upward-pointing and red downward-pointing triangles denote data for Al-bearing (Frost and Langenhorst, 2002; Irifune et al., 2010; McCammon et al., 2004; Murakami, 2005; Nishiyama and Yagi, 2003; Sinmyo and Hirose, 2013; Wood and Rubie, 1996; Wood, 2000) and Al-free systems (Auzende et al., 2008; Frost and Langenhorst, 2002; Nakajima et al., 2012; Sakai et al., 2009), respectively.

reside preferentially in the dodecahedral (A) site, and Al^{3+} in the octahedral (B) site, in the form of $(Mg^{2+},Fe^{2+},Fe^{3+})(Al^{3+},Si^{4+})O_3$ (Wood and Rubie, 1996). From the stoichiometric considerations alone, contents of Fe^{3+} measured by Mossbauer spectroscopy or EELS (electron energy-loss spectroscopy) imply a "spill over" of Al^{3+} to the dodecahedral site in the form of $(Mg^{2+},Fe^{2+},Fe^{3+},Al^{3+})(Al^{3+},Si^{4+})O_3$, and in some cases, an additional "spill over" of Fe^{3+} from the dodecahedral to the octahedral site as $(Mg^{2+},Fe^{2+},Fe^{3+},Al^{3+})(Al^{3+},Fe^{3+},Si^{4+})O_3$. As literature data typically do not separate Fe^{3+} and Fe^{2+} when reporting K_D, an apparent K_D ($K_{D\text{app}}$) is often reported instead, where $X_{Fe}^{pv} = (Fe^{2+} + Fe^{3+})/(Fe^{2+} + Fe^{3+} + Mg)$. For the sake of simplicity, hereafter we refer to $K_{D\text{app}}$ as K_D.

We examine the correlations between different chemical components and experimental conditions for the purpose of deriving a relationship or model that may be capable of predicting K_D values applicable to the lower mantle. In such an assessment of K_D for Al-bearing systems, different chemical components, Al content in bridgmanite (X_{Al}^{pv}) in atoms per formula unit (apfu), Fe-content ($Fe^{2+} + Fe^{3+}$) in bridgmanite in apfu (X_{Fe}^{pv}), and Fe-content in ferropericlase in apfu (X_{Fe}^{fp}), as well as experimental temperature (K) and pressure (GPa) are compiled from a number of literature sources and treated as variables. The apfu values are directly quoted from studies, or calculated from the reported mineral analyses when necessary (Frost and Langenhorst, 2002; Hirose, 2002; Irifune et al., 2010;

McCammon et al., 2004; Murakami, 2005; Nishiyama and Yagi, 2003; Sinmyo and Hirose, 2013).

Plotting different chemical components in 3D Cartesian coordinates (X_{Fe}^{fp} *vs* X_{Fe}^{Al} *vs* X_{Fe}^{pv}) reveals three groups of data, arranged qualitatively by the bulk Fe/(Fe+Mg) ratio (Fe# hereafter) of the bridgmanite-ferropericlase system. These data groups – labeled 'low', middle' and 'high' hereafter – roughly correspond to the bulk Fe# of below 0.10, 0.10–0.18, and higher than 0.18, respectively. The 'middle' data group that includes the pyrolitic composition (~ 0.107) also contains the highest abundance of data, and therefore was deemed best suited for statistical analysis. This data group was used to derive a model correlation among different chemical components and experimental conditions. Temperatures in this group typically range from 1800 to 2400 K, spanning the range of the lower mantle, while pressures range from 24 to 114 GPa. Coefficients of each of the independent components (any combination of T, P, X_{Fe}^{fp}, X_{Al}^{pv}, X_{Fe}^{pv}, K_D) were derived in relation to one component that was treated as a dependent variable (any of T, P, X_{Fe}^{fp}, X_{Al}^{pv}, X_{Fe}^{pv}) through linear least squares fitting, in the form of:

$$y = a_1x_1 + a_2x_2 + \dots a_nx_n \dots + b. \qquad (6)$$

Here, y is the dependent variable, x_1 to x_n are independent variables, a_1 to a_n are the coefficients of the independent variables, and b, is a constant. Correlations where X_i^a was potentially both a dependent and independent variable (e.g., $K_D = aX_{Fe}^{pv} + b$) were avoided in such an approach, as there would be little to no predictive value. The statistical likelihood of a randomly derived correlation between different chemical components and

experimental conditions was then assessed by calculating *p*-values as a test of statistical significance for the coefficients of independent variables simultaneously. Here the null hypothesis is an absence of a correlation between the dependent and independent variables. Following convention, *p*-values were deemed to indicate statistical significance at a value of 0.05 or less. A correlation was rejected as statistically insignificant and thus unlikely when *p*-values were higher than 0.05 for any coefficient, including the constant.

Components with a high probability of being related to one another were plotted in Cartesian coordinates (Fig. 2) to visually assess the linear least squares fitting. Here the criteria for assessing the quality of the data was more rigorous. Each individual data point that was noted to deviate from the trend was assessed and deemed to be an outlier when its inclusion to the data set caused the *p*-value of a coefficient to surpass 0.01. For the sake of completeness, we also plotted the experimental data that failed the *p*-test and were excluded from calculating regression coefficients. The derived relation was further used to calculate K_D values (Section 3.2).

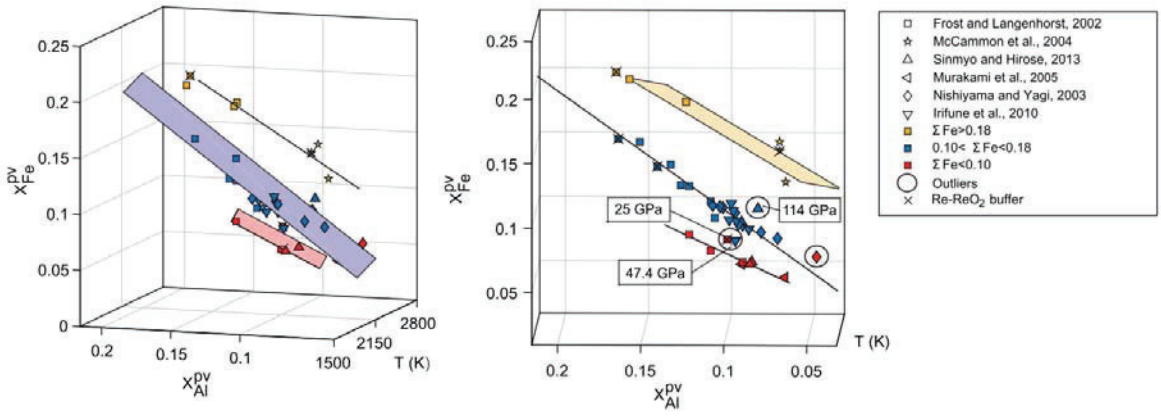

Figure 2. The relationship between X_{Fe}^{pv}, X_{Al}^{pv}, and *T* in Al-bearing systems. The mole fractions are in apfu units, *T* is in K. The data form three planar clusters roughly corresponding to the bulk Fe# of the system: the yellow plane with Fe#>0.18, the blue plane with Fe# of 0.10–0.18 inclusive of the bulk silicate Earth, and the plane red plane with Fe# < 0.10. The data sources are the same as in Fig. 1. To avoid cluttering, only the

most oxidizing experiments buffered by Re-ReO_2 (2 log units above QFM) are marked by crosses. Other experimental data were acquired at more reducing conditions spanning from the CO_2-CO buffer (2 log units below QFM) to IW buffer (~3.5 log units below QFM), provided the equilibration of the experimental charge with Fe capsules has been achieved.

2.3 Magma ocean modeling

It is widely believed that the interior of the early Earth once contained a partially or completely molten reservoir of silicate material referred to as a magma ocean (Elkins-Tanton, 2012). If such a magma ocean was deep enough to include a large, or the entire portion of the lower mantle, then the fractionation of Mg and Si, and thus Si-enrichment in the lower mantle would have most likely been generated during early magma ocean crystallization accompanied by gravitational settling of bridgmanite. The enrichment of the lower mantle in bridgmanite would, in turn, fractionate lithophile trace elements such as Lu, Hf, Sm, and Nd, leaving the upper mantle enriched in some elements and depleted in others. This is because bridgmanite and Ca-perovskite are either greatly depleted or enriched in Sm, Nd, and Lu relative to the melt from which they crystallize (Table 3).

Consequentially, a comparison of modeled trace element patterns produced by a putative bridgmanite settling with available trace element signatures of the upper mantle can shed light on whether this feature is still present if it has ever occurred. We test the hypothesis of a layered mantle through a simplified magma ocean model that explores trace element fractionation in such a scenario. Although the solidification of a magma ocean is expected to produce increasingly denser materials from bottom up due to progressive enrichment of residual liquid in FeO (e.g., Elkins-Tanton et al., 2003), we do not consider this effect in our model, because likely gravitational instability and overturn would erase any features of large scale mantle layering. For comparison of our model with the data, we refer to the Hf-Nd signatures of accessible mantle samples, commonly known as the terrestrial

Table 2. Solid-melt partition coefficients used in modeling

	Sm	Nd	Lu	Hf
Bridgmanite	0.050(2)[1]	0.0161(4)[1]	1.00(2)[1]	1.64(5)[1]
Ca-perovskite	21.1(10)[1,2]	16.7(10)[1,2]	13.5(7)[1,2]	1.70(2)[1,2]

[§]Here the solid-melt partition coefficients of ferropericlase are assumed to be negligible. The numbers in parentheses next to the partition coefficients in the table indicate uncertainty.

[1]Corgne et al., 2005,
[2]Walter et al., 2004

Table 3. Present day CHUR values for magma ocean modeling

Ratios	$^{147}Sm/^{144}Nd$	$^{143}Nd/^{144}Nd$	$^{176}Lu/^{177}Hf$	$^{176}Hf/^{177}Hf$
Values	0.1967[1]	0.512638[1]	0.0336[2]	0.282785[2]

[1]Jacobsen and Wasserburg, 1984
[2]Bouvier et al., 2008

array (hereafter denoted as the terrestrial Hf-Nd array, to avoid confusion with the "mantle array") (Vervoort et al., 2011, 1999). The dataset currently contains $^{176}Hf/^{177}Hf$ and $^{143}Nd/^{144}Nd$ ratios of more than 3500 samples from the continental and ocean crust, and the depleted mantle. These ratios are often expressed in ε-units (ε_{Hf} or ε_{Nd}), which are defined as the isotopic ratio deviations from those of chondrites, or CHUR (the CHondritic Uniform Reservoir), in parts per 10,000.

Following Albarede et al., (2000) and Caro et al., (2005), we assume a magma ocean with chondritic Sm/Nd and Lu/Hf ratios generated by an event such as the Moon-forming giant impact (e.g., Tonks and Melosh, 1993). Although Boyet and Carlson (2005) argued for a superchondritic Sm/Nd ratio of the bulk Earth based on the silicate Earth $^{142}Nd/^{144}Nd$ ratios being about 20 ppm higher than in ordinary chondrites, Huang et al. (2013) showed that the long-lived ^{147}Sm-^{143}Nd isotopic systematics are inconsistent with a superchondritic Sm/Nd ratio for the silicate Earth. A superchondritic Sm/Nd ratio for bulk Earth inferred from the extinct ^{146}Sm-^{142}Nd depends on two assumptions: (i) the bulk Earth is isotopically most similar to ordinary chondrites and (ii) the difference between ordinary chondrites and the Earth results from radioactive decay of ^{146}Sm in a silicate Earth with a higher than O-chondrite Sm/Nd ratio. As discussed by Huang et al (2013) it is not clear whether any of these assumptions are correct. First, the bulk Earth is isotopically more similar to enstatite chondrites than ordinary chondrites. Second, the available Sm-Nd isotopic data for terrestrial rocks do not support a superchondritic Sm/Nd ratio for the Earth. Clearly, there are too many uncertainties in how to use the extinct ^{146}Sm-^{142}Nd isotopic system for the type of modeling done for the long-lived ^{147}Sm-^{143}Nd and ^{176}Lu-^{176}Hf isotopic systems. For this

reason, we do not discuss the issue of possible superchondritic Sm/Nd ratio further in this paper.

Upon cooling the magma ocean crystallized bridgmanite and Ca-perovskite. It is unlikely that the Earth may have evolved from a single magma ocean; however, we assume one for the purposes of testing the hypothesis of a homogeneously Si-enriched lower mantle forming during magma ocean crystallization as suggested by Murakami et al., (2012). We neglect ferropericlase because its trace element fractionation effects are negligible compared to bridgmanite and Ca-perovskite (e.g., Walter et al., 2004).

Although the timing of such a large-scale differentiation event(s) is unclear, the last magma ocean forming event is thought to have been the Moon-forming giant impact, with the estimated timing of this event of about 30 (Jacobsen, 2005) but not exceeding 100 Ma (Yu and Jacobsen, 2011) after the formation of the first Solar System condensates at 4.567 Ga. Here we assume the onset of upper and lower mantle differentiation to occur at 4.467 Ga.

Because Ca-perovskite has the largest effect on the solid-melt partitioning of Sm, Nd, and Lu, and because the crystallization sequence of Ca-perovskite in relation to bridgmanite is unclear, we varied its amount in Si-enriched lower mantle scenarios, ranging from 2 wt% Ca-perovskite (+98 wt% bridgmanite) to 7 wt% Ca-perovskite (+93 wt% bridgmanite), with 1 wt% increments. The calculated model signatures of the upper mantle are plotted in ε-units along with their complementary lower mantle compositions. Here the upper mantle is set to take up 27 wt% of the whole mantle.

We consider two end-member magma ocean crystallization scenarios representing batch (or equilibrium) and fractional crystallization (subscripts “eq” and “fr”, respectively)

using equations from Caro et al., (2005) modified to include the effects of radioactive decay. Described below is the case for the Sm-Nd system, which equally applies to the Lu-Hf system when considering Lu in place of Sm, and Hf in place of Nd.

The bulk solid-liquid partition coefficient, D, is defined as:

$$D_E = \sum_m D_E^m \alpha^m \qquad (7)$$

where α^m is the mass fraction of mineral m, and D_E^m represents the crystal/melt partition coefficient of element E in mineral m.

First, the upper mantle $^{147}Sm/^{144}Nd$ ratio (R^{UM}) is calculated after assuming complete solidification of the lower mantle:

$$R_{eq}^{UM} = {}^{147}\mathrm{Sm}/{}^{144}\mathrm{Nd}_{\mathrm{CHUR}} \frac{(1-f)(D_{Nd}-1)+1}{(1-f)(D_{Sm}-1)+1} \qquad (8)$$

$$R_{fr}^{UM} = {}^{147}\mathrm{Sm}/{}^{144}\mathrm{Nd}_{\mathrm{CHUR}} \frac{f^{D_{Sm}-1}}{f^{D_{Nd}-1}} \qquad (9)$$

where t is the presumed time between differentiation of the upper and lower mantle and present day, $1-f$ is the weight fraction of the lower mantle compared to the whole mantle, where f is the melt fraction (upper mantle).

The complementary lower mantle $^{147}Sm/^{144}Nd$ ratios (R^{LM}) for the two crystallization models was calculated as follows:

$$R_{eq}^{LM} = {}^{147}\mathrm{Sm}/{}^{144}\mathrm{Nd}_{\mathrm{CHUR}} \frac{D_{Sm}(1-f)(D_{Nd}-1)+1}{D_{Nd}(1-f)(D_{Sm}-1)+1} \quad (10)$$

$$R_{fr}^{LM} = {}^{147}\mathrm{Sm}/{}^{144}\mathrm{Nd}_{\mathrm{CHUR}} \frac{1-f^{D_{Sm}}}{1-f^{D_{Nd}}} \quad (11)$$

The evolution of $^{143}\mathrm{Nd}/^{144}\mathrm{Nd}$ ratio before and after magma ocean crystallization is modeled using standard radioactive decay equations. For example, for the upper mantle we have:

$$^{143}\mathrm{Nd}/^{144}\mathrm{Nd}_{\ \mathrm{eq(UM)}} = {}^{143}\mathrm{Nd}/{}^{144}\mathrm{Nd}_{\mathrm{CHUR(today)}} - {}^{147}\mathrm{Sm}/{}^{144}\mathrm{Nd}_{\mathrm{CHUR(today)}}(e^{\lambda t_E} - 1) +$$

$$^{147}\mathrm{Sm}/^{144}\mathrm{Nd}_{\mathrm{CHUR}}(e^{\lambda t_E} - e^{\lambda t}) + R_{eq}^{UM}(e^{\lambda t} - 1) \quad (12)$$

where t_E is the age of the Earth, and t is the time passed from magma ocean crystallization to present, and λ, the decay constant of the radioactive parent isotope. Expressions are analogous for the Lu-Hf system.

The solid-melt partition coefficients and CHUR values used in the modeling are listed in Tables 2 and 3, respectively.

3. Results and discussion

3.1 A statistically significant relationship between chemical components and temperature for Al-bridgmanite

The statistical treatment of experimental data on bridgmanite equilibrated with ferropericlase reveals a correlation in each data group which relates the Al-content in bridgmanite, the Fe-content in bridgmanite, and temperature (K):

$$aX_{Fe}^{pv} + bT + cX_{Al} + d = 0 \qquad (13)$$

Such a formulation naturally forms a plane in 3-dimensional coordinates, whose axes represent X_{Fe}^{pv} *vs* X_{Al} *vs* T (Fig. 2). Pressure as a variable (ranging from 24 to 109 GPa) was found to be statistically insignificant (p-value > 0.6) and thus excluded in relation to other components in Eq. 13. All of the components presented in Fig. 2 are directly quoted from the literature or calculated from reported chemical analyses, with no additional treatment to the data.

For the 'middle' group (Fig. 2; blue), the trend is well-defined. The coefficients of the linear least squares fitting are $a = 1.26$, $b = 3.36\times10^{-5}$, $c = -1$, and $d = -0.0978$. When X_{Al}^{pv} is treated as the dependent variable, the p-value of coefficient b (the temperature component) is $\sim1\times10^{-3}$ for all the data compiled for this range of bulk Fe#, whereas the p-value of coefficient c (X_{Fe}^{pv} component) is closer to 10^{-11}.

P-values for X_{Fe}^{pv} in relation to X_{Al}^{pv} for the 'low' and 'high' groups of data are similarly low, on the order of 10^{-6}. On the other hand, the p-values for the coefficients of the temperature component in the "high" and "low" groups are ~0.06 and ~0.15 respectively, possibly due to a weaker correlation compared to the relationship between X_{Al}^{pv} *vs* X_{Fe}^{pv}, or more likely due to the small data set. Although the 'low' and 'high' data groups are not directly applicable to the BSE, they do give important insights into crystal chemistry of bridgmanite as discussed in section 3.2.

3.2 K_D for Al-bearing systems

The correlations between bridgmanite composition and temperature (Eq. 13) in all three groups with different Fe# imply that the derived trends may be controlled by the crystal chemistry of Al-bearing bridgmanite. It appears that there is a correlation between the Fe# of a group and how Al^{3+} and Fe^{3+} are distributed between different sites. In the 'high' group (Fig. 2, yellow), the Fe^{3+}/Al^{3+} ratio is close to 1 within 1 sigma uncertainty of X_{Fe}^{pv} and $Fe^{3+}/\Sigma Fe$ measurements (Frost and Langenhorst, 2002, McCammon et al., 2004), requiring, by a charge balance, Al^{3+} and Fe^{3+} to occupy the octahedral and dodecahedral sites, respectively. In the 'low' group (Fig. 2, red) the Al^{3+}/Fe^{3+} ratio exceeds 1.5, requiring Al^{3+} to occupy both the octahedral and dodecahedral sites, leading to a chemical formula $(Mg^{2+}, Fe^{2+}, Fe^{3+}, Al^{3+})(Al^{3+},Si^{4+})O_3$ (Frost and Langenhorst, 2002). The latter also applies to the 'middle' group which exhibits a slight overabundance of Al^{3+} compared to Fe^{3+} (Al^{3+}/Fe^{3+}~1.2; Frost and Langenhorst, 2002). Clearly, there is a positive correlation between the bulk Fe# and the amount of Fe^{3+} in the system that would be expected at constant redox conditions expressed as, say, Fe^{3+}/Fe^{2+} ratio. However, experiments conducted under different controlled redox conditions span at least 6 log units of f_{O2} (Fig. 2), hence leaving the reason for such a correlation between the bulk Fe# and Fe^{3+}/Fe^{2+} ratio unclear.

Although the definition of K_D requires the knowledge of the Fe/Mg ratios of both bridgmanite and ferropericlase, as Eq. 13 only constrains the Fe-content of bridgmanite, the amount of Fe in ferropericlase is inferred indirectly. Using Eq. 13 to constrain the Fe-content in Al-bearing bridgmanite, the Fe/Mg ratio of bridgmanite is approximated as:

$$X_{Fe}^{pv}/(1 - X_{Fe}^{pv}). \qquad (14)$$

Then the X_{Fe}^{fp} of ferropericlase is calculated from the mass balances of Fe and Mg:

$$eX_{Fe}^{pv}/(X_{Fe}^{pv}+X_{Mg}^{pv}) + fX_{Fe}^{fp}/(X_{Fe}^{fp}+X_{Mg}^{fp}) = Fe\# \quad (15)$$

where *e* and *f* are the respective mineral proportions of bridgmanite and ferropericlase in the experimental charge. For the pyrolitic composition, *e* and *f* are 0.685 and 0.315.

The calculated Fe-contents in Al-bridgmanite, and ferropericlase (equations 13–15) as well as corresponding K_D values reproduce the experimental data very well (Fig. 3). Despite potential errors associated with approximations of Fe/Mg ratio in bridgmanite (Eq. 14) and the indirect inference of X_{Fe}^{fp} (Eq 15), 75% of the calculated K_D values plot within ±0.10 of the experimental values, while 90% of the calculated K_D values plot within ±0.15 (R^2= 0.87). The effect of the bulk Fe# on the K_D is well demonstrated by two experiments conducted at the same pressure of 24 GPa, near identical X_{Al}^{pv} of ~0.11, similar temperatures of 1923 and 1873 K, but different bulk Fe# of 0.133 and 0.110 by Frost and Langenhorst (2002) and Nishiyama and Yagi (2003), respectively. Although the expected response from a conventional exchange equilibrium reaction dictates that the K_D values should be similar for the same intensive parameters despite different bulk compositions, the experiment at higher Fe# yields K_D of 0.46, while at lower Fe# the K_D is 0.98. Our set of equations that takes into account the bulk Fe# considers such a behavior very well (Fig. 3c).

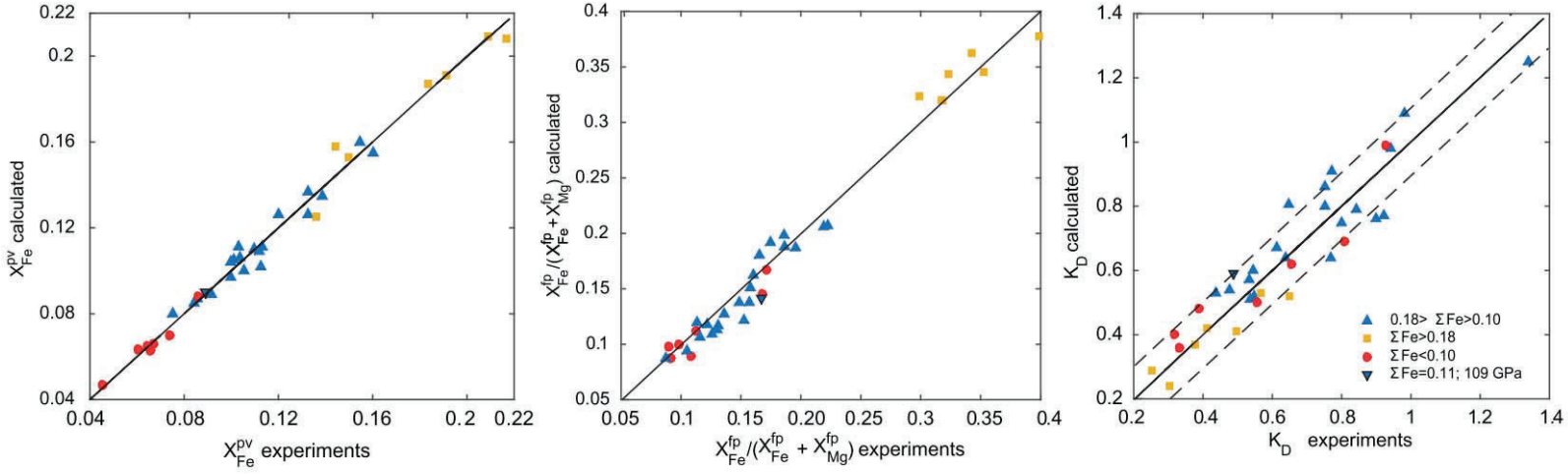

Figure 3. Reproducibility of the X_{Fe}^{pv} (a), $X_{Fe}^{fp}/(X_{Fe}^{fp} + X_{Fe}^{pv})$ (b) and K_D (c) calculated with Eq. 13–15. The dotted lines in (c) delineate the ±0.10 uncertainty band. $R^2 = 0.87$ for all data. The reproducibility of the experimental K_D value at 109 GPa (black open triangle) implies that K_D is unlikely to be significantly (>0.10) affected by the spin transition of ferropericlase. Data that are deemed outliers in Fig. 2 are not included in the plots.

Our finding that the Fe-Mg partitioning between Al-bearing bridgmanite and ferropericlase is strongly controlled by bridgmanite questions the notion (e.g., Irifune et al., 2010) that Fe-partitioning behavior in Al-bearing systems is affected by the spin transition of Fe in ferropericlase. For instance, a substantial decrease (of ~0.3) in K_D at 44 GPa compared to lower pressure values in the study of Irifune et al., (2010) can be explained by the difference in Al content of bridgmanite, with X_{Al}^{pv}= 0.087 apfu and $X_{Al}^{pv} \geq 0.094$, at high and lower pressures, respectively. Here, the decrease in K_D is a reflection of the high sensitivity of K_D to Al-content in bridgmanite rather than due to the spin transition in ferropericlase. Moreover, the 47 GPa data point (Irifune et al., 2010) plots very close to a low pressure (25 GPa) data of Frost and Langenhorst, (2002) (circled; Fig. 2). The deviations of these points from the determined trends in 3D space may be results from errors in electron microprobe analyses or incomplete equilibration of the synthesized sample, or both. In contrast, a data point at 109 GPa (Sinmyo and Hirose, 2013) is shown to conform to trends in Fig. 2, where the calculated K_D value is reproduced to match the experimental value to within 0.10 (Fig. 3). This further suggests that observed variations in K_D values are typically not related to the high pressure (>60 GPa) effects involving the spin transition in ferropericlase.

Although large variations in K_D in Al-bearing systems (Fig. 1) were attributed to the possible lack of equilibrium across experiments (e.g., Frost and Langenhorst, 2002), we find the quality of the data to be more or less consistent from study to study. This is based on the fact that the data follow distinct trends, which are largely defined by experimental conditions such as temperature and the charge composition rather than by lab (study) and/or apparatus type (diamond anvil *vs* multi-anvil cell).

3.3 Calculation of lower mantle seismic profiles when considering Ca-perovskite and K_D

The lower mantle shear wave velocity profile of the mixture of bridgmanite and ferropericlase in pyrolitic proportions (8:2 in volume) using the K_D value of 0.24, typical of Al-free systems yields a maximum offset from PREM of 3.3%, consistent with Murakami et al., (2012). The addition of Ca-perovskite to the mixture while still assuming a K_D of 0.24 reduces the offset of the calculations from PREM to around 1.6%, with the offset normalized to PREM at a maximum at lower pressures (<60 GPa).

However, the primitive mantle composition contains 4.5 wt% Al_2O_3 (McDonough and Sun, 1995), which mostly resides in bridgmanite (~5 wt% Al_2O_3). For the bulk silicate Earth Fe# of 0.107, the solution of Eq. 13–15 yields a K_D value of ~1.05 at 1880 K, corresponding to a depth of 670km (24 GPa) in the lower mantle. K_D decreases along the lower mantle adiabatic temperature profile (Brown and Shankland, 1980) to ~0.65 near 135 GPa (Fig. 4a).

Increasing K_D from 0.24 to higher values characteristic of the BSE diminishes the discrepancy of lower mantle shear wave velocity calculations from PREM to 0.2–0.6%. Meanwhile, considerations in the 1 sigma uncertainties in the thermoelastic constants of Al-bridgmanite alone in these calculations yields an uncertainty in lower mantle shear wave velocity calculations of ~±1%. An uncertainty of ±0.10 in K_D values translates to a ~0.1% uncertainty in shear wave velocity calculations, which is negligible in comparison.

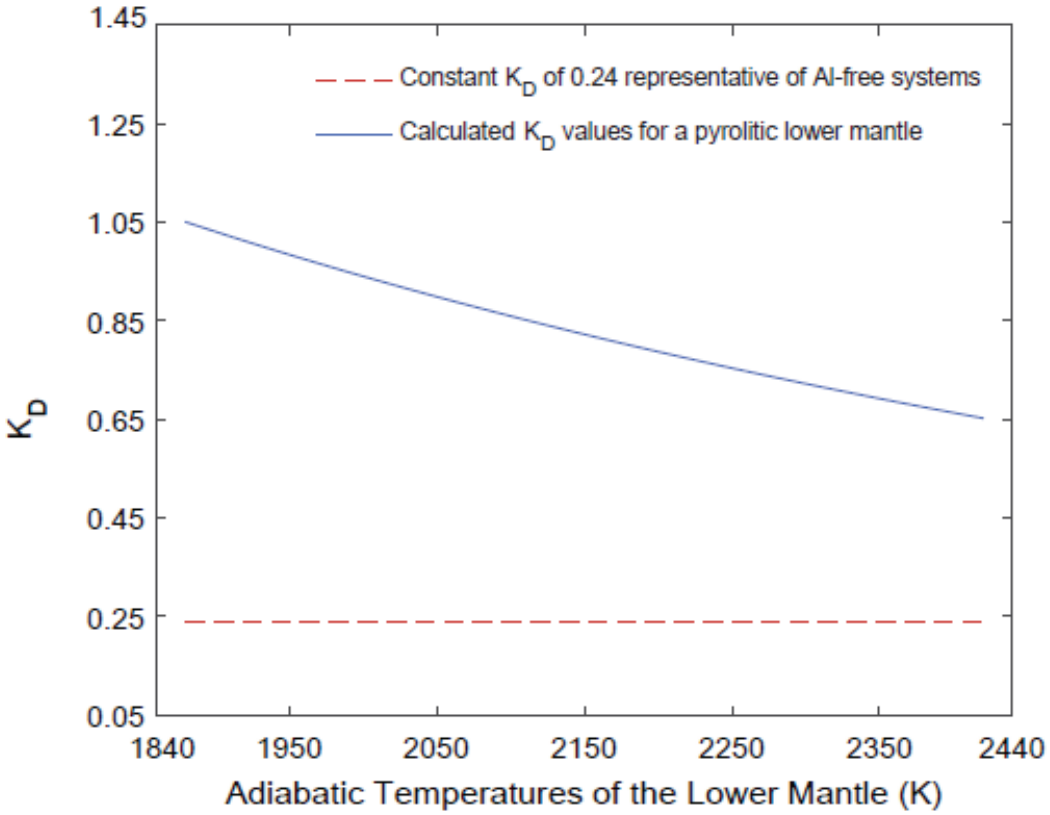
Constant K_D of 0.24 representative of Al-free systems
Calculated K_D values for a pyrolitic lower mantle
K_D
1.45
1.25
1.05
0.85
0.65
0.45
0.25
0.05
1840
1950
2050
2150
2250
2350
2440
Adiabatic Temperatures of the Lower Mantle (K)

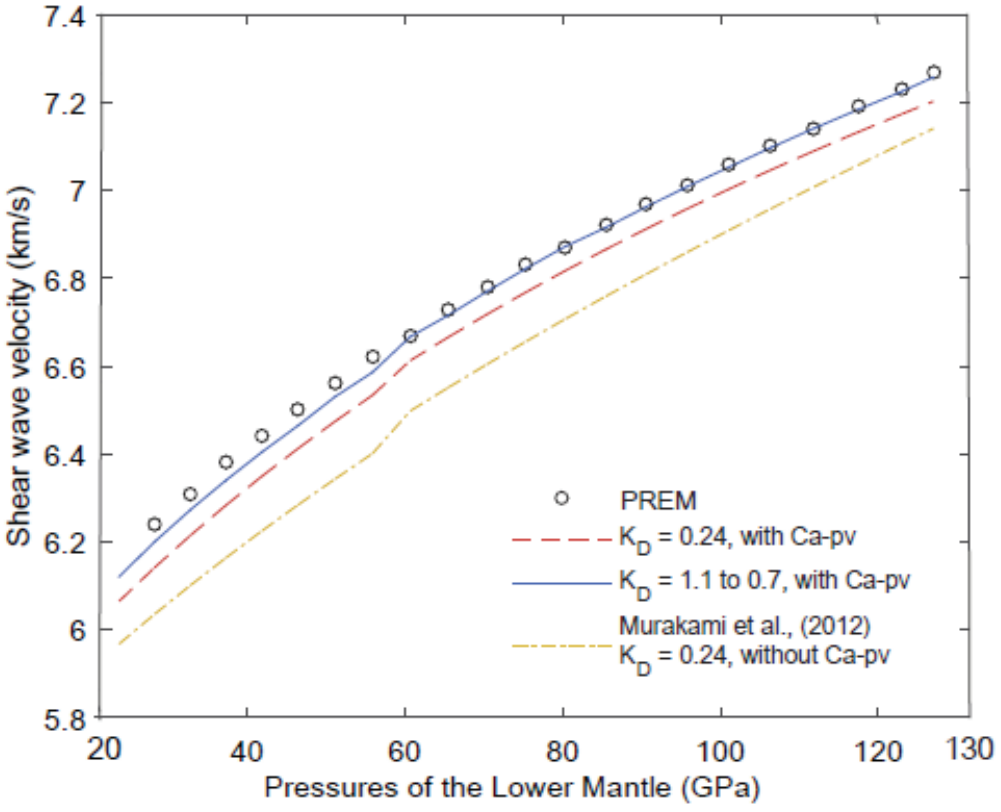
Shear wave velocity (km/s)
7.4
7.2
7
6.8
6.6
6.4
6.2
6
5.8
20
40
60
80
100
120
130
Pressures of the Lower Mantle (GPa)
PREM
K_D = 0.24, with Ca-pv
K_D = 1.1 to 0.7, with Ca-pv
Murakami et al., (2012)
K_D = 0.24, without Ca-pv

Figure 4. Variations of K_D (a) and shear wave velocity (b) along the lower mantle adiabatic geotherm. a) Calculation of projected K_D values of the lower mantle based on analysis of experimental data on an adiabatic geotherm. (a) The blue solid line shows K_D values for a pyrolitic lower mantle (McDonough and Sun, 1995). The dotted red line (K_D= 0.24) is characteristic of Al-free systems. Note that the change of K_D with mantle depth is due to the temperature change along an adiabatic geotherm, independent of corresponding pressure change. There is no effect of the spin transition in ferropericlase (see text for details). (b) Open circles – PREM, yellow dash-dotted line - the model of Murakami et al., (2012) with constant K_D=0.24 and no Ca-perovskite, red dotted line – K_D = 0.24 with Ca-perovskite, solid blue line – variable K_D plus Ca-perovskite. The consideration of Ca-perovskite and high K_D values characteristic of an Al-bearing pyrolitic model allows matching the pyrolitic lower mantle seismic 1D shear wave velocity profile to within 1%.

The changes in shear and bulk properties induced by the spin transition of Fe in ferropericlase are noticeable in pyrolitic lower mantle shear wave velocity calculations as a small jump at ~60 GPa, whereas such features are not apparent in seismic 1D shear wave velocity models. The velocity jump from high spin to low spin at 60 GPa (~1500 km depth from the Earth's surface) is calculated to be 0.3%. In contrast, variations in shear wave velocities in 3D tomographic models such as S40RTS (Ritsema et al., 2011), reveal shear wave velocity anomalies of up to ±1.5%, with no clear indication of a global velocity change occurring at depths corresponding to range ~60 GPa. It may well be that seismic 1D models are incapable of resolving such a small scale discontinuity as one expected around 60 GPa, as inferred from tomographic shear wave velocity variations that are much larger than the change of velocity incurred by the spin transition of Fe in ferropericlase at such depths. Alternatively, an absence of a feature in 1D seismic models may be explained by a gradual spin transition over a range of pressures in the mantle as observed in experiments (e.g., Badro, 2014), rather than by an abrupt change at around 60 GPa.

The calculations in this study demonstrate the importance of less abundant major elements such as Ca and Al in modeling shear wave velocities of the lower mantle. We note

that the large offset of the shear wave velocity calculations of a pyrolitic lower mantle, demonstrated to be incompatible with PREM by up to 3.2% (Murakami et al., 2012), can be resolved by considering Ca-perovskite and Fe-Mg partitioning values characteristic of Al-bearing lower mantle minerals. As Ca and Al cannot be excluded from the bulk silicate Earth, the considerations of a Ca-bearing phase and the effects of Al on the shear wave velocity model of the lower mantle may well support a lower mantle of a pyrolitic composition over one that is Si-enriched.

3.4 Trace element signatures of magma ocean crystallization

Kato et al. (1988) have previously explored possible trace element fractionation during solidification of a terrestrial magma ocean to conclude that the mantle was unlikely to be chemically stratified. Owing to recent claims of a chemically stratified mantle involving the entire volume of the lower mantle, here we explore the fractionation of trace elements due to formation of a Si-enriched lower mantle using the Hf-Nd isotopic systems, while comparing the results to the terrestrial array. Such a test is limited to the layered mantle scenario because only the lack of communication between the upper and lower mantles would have been capable of preserving these signatures.

The gravitational settling of denser crystals during the magma ocean crystallization results in an enrichment of the lower mantle in Si compared to both the chondritic source and the complementary residual melt, which formed the upper mantle. Once the crystallization front rises to a depth where the bridgmanite and Ca-perovskite become unstable, substantial fractionation of trace elements is no longer possible. At this point the silicate magma ocean consists of 73 wt% solids, corresponding to the weight proportion of

the silicate lower mantle, and 27 wt% residual melt which later solidifies to form the primitive, pyrolitic upper mantle ("PUM"; Fig. 5a). Subsequent repeated remelting of the Earth throughout its geologic history produces materials of the terrestrial Hf-Nd array representing the continental and ocean crust, as well as the depleted mantle (Blichert-Toft and Albarede, 1997; Vervoort et al., 2011, 1999).

The differentiation of the bulk chondritic Earth into the model PUM and Si-enriched lower mantle results in a strong fractionation trend in ε_{Hf}-ε_{Nd} space (Fig. 5). The model PUM is enriched in Hf relative to CHUR in all variants of lower mantle model compositions explored here, exhibiting negative ε values. The Sm and Hf content of the upper mantle, on the other hand, are strongly controlled by the assumed Ca-perovskite content in the lower mantle. The ε_{Hf}-ε_{Nd} signatures of the upper and lower mantles fractionate up to dozens of ε-units away from the CHUR in opposite, but complementary directions. The subsequent differentiation of the PUM (arrows in Fig. 5b) into the depleted mantle and crust is anticipated to transform a single PUM ε_{Hf}-ε_{Nd} value (blue points in Fig. 5c) into an array with a slope parallel to that of the terrestrial Hf-Nd array.

The consequences of having a Si-enriched lower mantle formed in a large-scale differentiation event are demonstrated in Fig. 5c by the modeled ε_{Hf} and ε_{Nd} signatures of the upper and lower mantles. Despite wide variations in Ca-perovskite content, the fractionation of the trace elements is so large, that none of the modeled PUM ε_{Hf}-ε_{Nd} values comes close to CHUR, or remotely overlaps with the PUM fractionation line of the present day terrestrial Hf-Nd array.

As the D values for the of the Sm-Nd and Lu-Hf isotope systems used here are measured at pressures close to the 660km discontinuity, it is possible that the partition

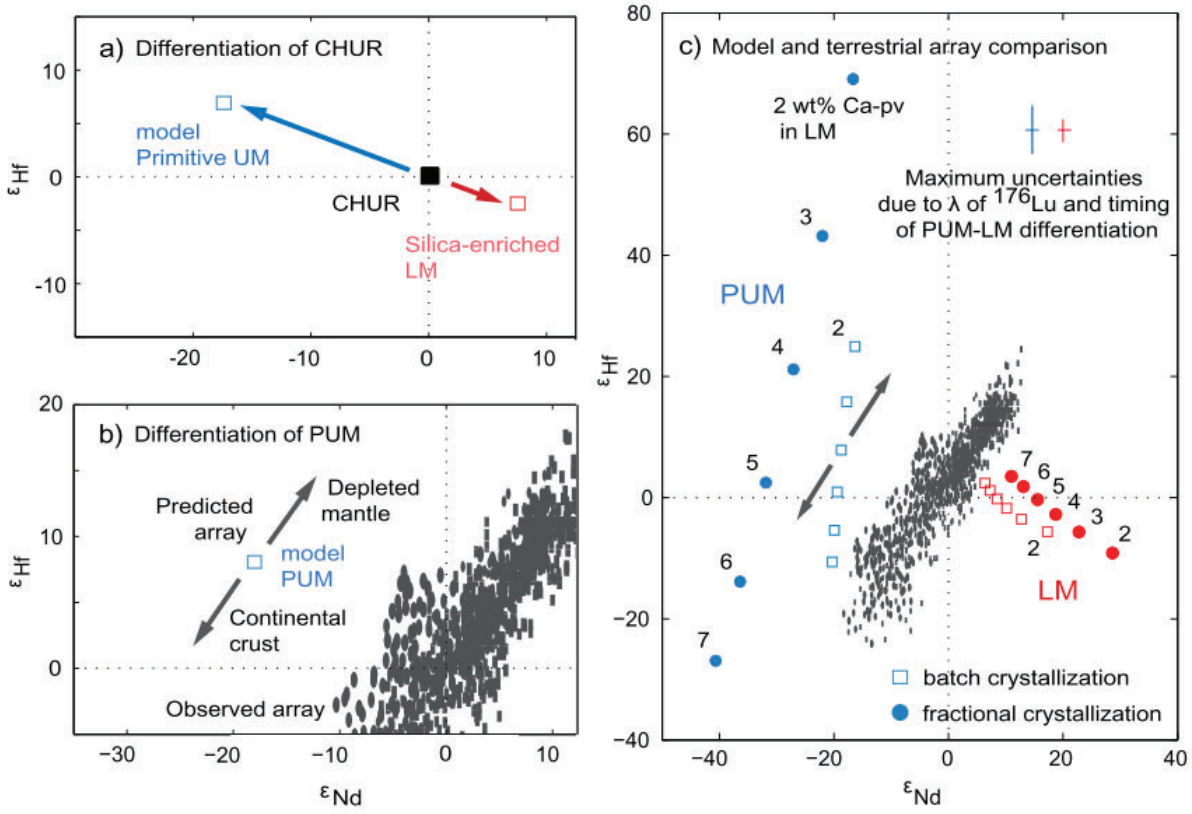

Figure 5. The effect of putative Si-enriched lower mantle on the Hf-Nd signatures of the upper mantle: Model *vs* Observations. The blue and red symbols represent the putative primitive upper (PUM) and complementary Si-enriched lower mantles, respectively. Open squares and filled circles denote batch and fractional crystallization models, respectively. a) A cartoon illustrating how the compositions of the model upper (blue arrow) and lower (red arrow) mantle would evolve during crystallization of the CHUR magma ocean at 4.467 Ga. b) A cartoon illustrating how the $\square_{Hf}$ and $\square_{Nd}$ of putative upper mantle would fractionate (grey arrows) as it differentiates into a depleted upper mantle (DUM) and the crust. The grey symbols show the present day terrestrial Hf-Nd array (Vervoort et al., 2011, 1999). c) Model results. This model uses the decay constants of 1.867×10^{-11} yr^{-1} for ^{176}Lu (Söderlund et al., 2004), and 6.54×10^{-9} yr^{-1} ^{147}Sm (Kossert et al., 2009). The numbered blue and red symbols show respectively the compositions of the putative upper and lower mantles at different contents of Ca-perovskite (Ca-pv, numbers next to the symbols) in the modeled Si-enriched lower mantle. The grey symbols show the terrestrial Hf-Nd array. The red and blue crosses in the upper right corner show maximum uncertainties induced by the different values of ^{176}Lu decay constant and the timing of the mantle differentiation, respectively. The lack of overlap between the modeled PUM reservoirs complementary to a putative Si-enriched lower mantle and the terrestrial array argues against the presence of a Si-enriched lower mantle in the present Earth.

coefficients may change with pressure and temperature. In such a case, *D* values may well increase with increasing pressure because of a positive Clapeyron-slope of fusion in silicates (Liebske et al., 2005). This would tend to increase the fractionation effects of the ε_{Hf}-ε_{Nd} signatures (Fig. 5c), making the difference between modeled ε_{Hf}-ε_{Nd} signatures and the terrestrial Hf-Nd array larger.

The timing of differentiation of a global magma ocean and the uncertainty in the ^{176}Lu decay constant are also incapable of significantly affecting large fractionation effects predicted by our model of a Si-enriched lower mantle. The ε_{Hf} values are affected by the different plausible values of the ^{176}Lu decay constant (Bizzarro et al., 2003; Scherer et al., 2001) by about 1 ε unit at most. The explored difference in the onset of mantle differentiation by ± 100 Ma results in the maximum shift of the ε_{Hf}-ε_{Nd} values of ±2 ε units. None of these factors compensates for the lack of overlap between our model upper mantle ε_{Hf} and ε_{Nd} values and the terrestrial Hf-Nd array.

We note that the PUM ε_{Hf}-ε_{Nd} signatures resulting from the formation of a Si-enriched lower mantle (Fig. 5c) cannot be erased by subsequent upper mantle melting, as these ε_{Hf}-ε_{Nd} signatures are strongly controlled by minerals that are stable only under the lower mantle conditions. Therefore, the lack of overlap between our model and the terrestrial Hf-Nd array makes a Si-enriched lower mantle containing more than 93 wt% bridgmanite at present day unlikely. In contrast, an early decoupling of Hf-Nd signatures (Hoffmann et al., 2011; Puchtel et al., 2013) suggests that chemical layering was present early on, although often inferred to occur at depths well into the lower mantle. Even if there was once chemical stratification involving a composition change at the 660km discontinuity, the upper and lower mantles have been subsequently disturbed and remixed rather than

preserved perhaps during rigorous convection predicted by models of magma ocean evolution (Tonks and Melosh, 1993).

4. Conclusions

The shear-wave velocity model of the lower mantle matches the pyrolitic composition to within 1% when the contribution of Ca-perovskite and relatively high K_D values characteristic of Al-bearing systems are taken into account.

The evaluation of experimental data on Fe-Mg partitioning between bridgmanite and ferropericlase in Al-bearing systems shows that K_D depends upon the Al content, the bulk Fe# of the system, and temperature. Dependence of K_D on pressure up to 109 GPa is not significant. K_D is also unlikely to be substantially (>0.10) affected by the spin transition of Fe in ferropericlase. For the bulk silicate Earth composition combined with lower mantle temperature conditions, K_D values likely exceed 0.65 throughout the whole lower mantle, approaching ~1.05 near the 660km discontinuity.

Our modeling of the crystallization of a magma ocean with a Si-enriched lower mantle yields ε_{Hf} and ε_{Nd} signatures that do not overlap with the present day terrestrial array, implying that if such a Si-enriched lower mantle has ever formed, it was not preserved throughout Earth's history. It may be concluded that the lower mantle is likely pyrolitic, and that the mantle as a whole need not be chemically stratified.

References

Agee, C., Walker, D., 1988. Mass balance and phase density constraints on early differentiation of chondritic mantle. Earth Planet. Sci. Lett. 90, 144–156.

Albarede, F., Blichert-Toft, J., Vervoort, J., Gleason, J., Rosing, M., 2000. Hf-Nd isotope evidence for a transient dynamic regime in the early terrestrial mantle. Nature 404, 488–490.

Allegre, C.J., Poirier, J., Humler, E., Hofmann, A.W., 1995. The chemical composition of the Earth. Earth Planet. Sci. Lett. 134, 515–526.

Auzende, A.-L., Badro, J., Ryerson, F.J., Weber, P.K., Fallon, S.J., Addad, A., Siebert, J., Fiquet, G., 2008. Element partitioning between magnesium silicate perovskite and ferropericlase: New insights into bulk lower-mantle geochemistry. Earth Planet. Sci. Lett. 269, 164–174. doi:10.1016/j.epsl.2008.02.001

Badro, J., 2014. Spin Transitions in Mantle Minerals. Annu. Rev. Earth Planet. Sci. 42, 231–248. doi:10.1146/annurev-earth-042711-105304

Birch, F., 1952. Elasticity and consitution of the Earth's interior. J. Geophys. Res. 57, 227–286.

Bizzarro, M., Baker, J.A., Haack, H., Ulfbeck, D., Rosing, M., 2003. Early history of Earth's crust-mantle system inferred from hafnium isotopes in chondrites. Nature 421, 931–3. doi:10.1038/nature01421

Blichert-Toft, J., Albarede, F., 1997. The Lu-Hf isotope geochemistry of chondrites and the evolution of the mantle-crust system. Earth Planet. Sci. Lett. 148, 243–258.

Boyet, M., Carlson, R., 2006. A new geochemical model for the Earth's mantle inferred from 146Sm–142Nd systematics. Earth Planet. Sci. Lett. 250, 254–268. doi:10.1016/j.epsl.2006.07.046

Boyet, M., Carlson, R.W., 2005. Nd-142 evidence for early (> 4.53 Ga) global differentiation of the silicate Earth. Science (80-.). 309, 576–581. doi:10.1126/science.1113634

Brown, J.M., Shankland, T.J., 1981. Thermodynamic parameters in the Earth as determined from seismic profiles. Geophys. J. R. astr. Soc. 66, 579–596.

Caro, G., Bourdon, B., Wood, B.J., Corgne, A., 2005. Trace-element fractionation in Hadean mantle generated by melt segregation from a magma ocean. Nature 436, 246–249. doi:10.1038/nature03827

Chantel, J., Frost, D.J., McCammon, C.A., Jing, Z., Wang, Y., 2012. Acoustic velocities of pure and iron-bearing magnesium silicate perovskite measured to 25 GPa and 1200 K. Geophys. Res. Lett. 39, L19307. doi:10.1029/2012GL053075

Dziewonski, A., Anderson, D.L., 1981. Preliminary reference Earth model. Phys. Earth Planet. Inter. 25, 297–356.

Elkins-Tanton, L.T., 2012. Magma oceans in the inner solar system. Annu. Rev. Earth Planet. Sci. 40, 113–139. doi:10.1146/annurev-earth-042711-105503

Elkins-Tanton, L.T., Parmentier, E.M., Hess, P.C., 2003. Magma ocean fractional crystallization and cumulate overturn in terrestrial planets: Implications for Mars. Meteorit. Planet. Sci. 38, 1753–1771. doi:10.1111/j.1945-5100.2003.tb00013.x

Frost, D.J., Langenhorst, F., 2002. The effect of Al_2O_3 on Fe-Mg partitioning between magnesiowustite and magnesium silicate perovskite. Earth Planet. Sci. Lett. 199, 227–241.

Georg, R.B., Halliday, A.N., Schauble, E.A., Reynolds, B.C., 2007. Silicon in the Earth's core. Nature 447, 1102–1106. doi:10.1038/nature05927

Green, D.H., Hibberson, W.O., Jaques, A.L., 1979. Petrogenesis of mid-ocean ridge basalts, in: McElhinny, M.W. (Ed.), The Earth: Its Origin, Structure and Evolution. Academic Press, London, pp. 265–299.

Hill, R., 1952. The elastic behaviour of a crystalline aggregate. Proc. Phys. Soc. 65, 349–354.

Hirose, K., 2002. Phase transitions in pyrolitic mantle around 670-km depth: Implications for upwelling of plumes from the lower mantle. J. Geophys. Res. 107, 2078–2088.

Hoffmann, J.E., Münker, C., Polat, A., Rosing, M.T., Schulz, T., 2011. The origin of decoupled Hf–Nd isotope compositions in Eoarchean rocks from southern West Greenland. Geochim. Cosmochim. Acta 75, 6610–6628. doi:10.1016/j.gca.2011.08.018

Huang, S., Jacobsen, S.B., Mukhopadhyay, S., 2013. ^{147}Sm-^{143}Nd systematics of Earth are inconsistent with a superchondritic Sm/Nd ratio. Proc. Natl. Acad. Sci. U. S. A. 110, 4929–34. doi:10.1073/pnas.1222252110

Irifune, T., 1994. Absence of an aluminous phase in the upper part of the Earth's lower mantle. Nature 370, 131–133.

Irifune, T., Shinmei, T., Mccammon, C.A., Miyajima, N., Rubie, D.C., Frost, D.J., 2010. Iron partitioning and density changes of pyrolite in Earth's lower mantle. Science 1, 193–195.

Ito, E., Takahashi, E., 1989. Postspinel transformations in the system Mg_2SiO_4-Fe_2SiO_4 and some geophysical implications. J. Geophys. Res. 94, 10,637–10,646.

Jackson, J.M., 2004. Sound velocities and elasticity of aluminous $MgSiO_3$ perovskite: Implications for aluminum heterogeneity in Earth's lower mantle. Geophys. Res. Lett. 31, L10614. doi:10.1029/2004GL019918

Jacobsen, S.B., 2005. The Hf-W isotopic system and the origin of the Earth and Moon. Annu. Rev. Earth Planet. Sci. 33, 531–570. doi:10.1146/annurev.earth.33.092203.122614

Jacobsen, S.D., Reichmann, H., Spetzler, H.A., Mackwell, S.J., Smyth, J.R., Angel, R.J., Mccammon, C.A., 2002. Structure and elasticity of single-crystal (Mg,Fe)O and a new method of generating shear waves for gigahertz ultrasonic interferometry. J. Geophys. Res. 107, 2037–2050.

Jagoutz, E., Palme, H., Baddenhausen, H., Blum, K., Cendales, M., Spettel, B., Lorenz, V., Wanke, H., 1979. The abundances of major, minor, and trace elements in the Earth's mantle as derived from primitive ultramafic nodules. LPSC X, 610–612.

Javoy, M., Kaminski, E., Guyot, F., Andrault, D., Sanloup, C., Moreira, M., Labrosse, S., Jambon, A., Agrinier, P., Davaille, A., Jaupart, C., 2010. The chemical composition of the Earth: Enstatite chondrite models. Earth Planet. Sci. Lett. 293, 259–268. doi:10.1016/j.epsl.2010.02.033

Karki, B.B., Crain, J., 1998. First principles determination of elastic properties of $CaSiO_3$ perovskite at lower mantle pressures. Geophys. Res. Lett. 25, 2741–2744.

Kato, T., Ringwood, A.E., Irifune, T., 1988. Experimental determination of element partitioning between silicate perovskites, garnets and liquids: constraints on early differentiation of the mantle. Earth Planet. Sci. Lett. 89, 123–145.

Kobayashi, Y., Kondo, T., Ohtani, E., Hirao, N., Miyajima, N., Yagi, T., Nagase, T., Kikegawa, T., 2005. Fe-Mg partitioning between (Mg, Fe)SiO_3 post-perovskite, perovskite, and magnesiowüstite in the Earth's lower mantle. Geophys. Res. Lett. 32. doi:10.1029/2005GL023257

Kossert, K., Jörg, G., Nähle, O., v. Gostomski, C.L., 2009. High-precision measurement of the half-life of 147Sm. Appl. Radiat. Isot. 67, 1702–1706.

Lee, K.K.M., O'Neill, B., Panero, W.R., Shim, S.-H., Benedetti, L.R., Jeanloz, R., 2004. Equations of state of the high-pressure phases of a natural peridotite and implications for the Earth's lower mantle. Earth Planet. Sci. Lett. 223, 381–393. doi:10.1016/j.epsl.2004.04.033

Liebske, C., Corgne, A., Frost, D.J., Rubie, D.C., Wood, B.J., 2005. Compositional effects on element partitioning between Mg-silicate perovskite and silicate melts. Contrib. to Mineral. Petrol. 149, 113–128. doi:10.1007/s00410-004-0641-8

Mao, H., Shen, G., Hemley, R., 1997. Multivariable dependence of Fe-Mg partitioning in the lower mantle. Science 278, 2098–2100.

Matas, J., Bass, J., Ricard, Y., Mattern, E., Bukowinski, M.S.T., 2007. On the bulk composition of the lower mantle: predictions and limitations from generalized inversion of radial seismic profiles. Geophys. J. Int. 170, 764–780.

McCammon, C.A., Lauterbach, S., Seifert, F., Langenhorst, F., van Aken, P.A., 2004. Iron oxidation state in lower mantle mineral assemblages. Earth Planet. Sci. Lett. 222, 435–449. doi:10.1016/j.epsl.2004.03.018

McDonough, W., Sun, S. -s., 1995. The composition of the Earth. Chem. Geol. 120, 223–253. doi:10.1016/0009-2541(94)00140-4

Murakami, M., 2005. Post-perovskite phase transition and mineral chemistry in the pyrolitic lowermost mantle. Geophys. Res. Lett. 32, L03304. doi:10.1029/2004GL021956

Murakami, M., Ohishi, Y., Hirao, N., Hirose, K., 2012. A perovskitic lower mantle inferred from high-pressure, high-temperature sound velocity data. Nature 485, 90–4. doi:10.1038/nature11004

Nakajima, Y., Frost, D.J., Rubie, D.C., 2012. Ferrous iron partitioning between magnesium silicate perovskite and ferropericlase and the composition of perovskite in the Earth's lower mantle. J. Geophys. Res. 117, B08201. doi:10.1029/2012JB009151

Nishiyama, N., Yagi, T., 2003. Phase relation and mineral chemistry in pyrolite to 2200°C under the lower mantle pressures and implications for dynamics of mantle plumes. J. Geophys. Res. 108, 2255. doi:10.1029/2002JB002216

Puchtel, I.S., Blichert-Toft, J., Touboul, M., Walker, R.J., Byerly, G.R., Nisbet, E.G., Anhaeusser, C.R., 2013. Insights into early Earth from Barberton komatiites: Evidence from lithophile isotope and trace element systematics. Geochim. Cosmochim. Acta 108, 63–90. doi:10.1016/j.gca.2013.01.016

Ringwood, A.E., 1962. A model for the upper mantle. J. Geophys. Res. 67, 857–867.

Ritsema, J., Deuss, a., Van Heijst, H.J., Woodhouse, J.H., 2011. S40RTS: A degree-40 shear-velocity model for the mantle from new Rayleigh wave dispersion, teleseismic traveltime and normal-mode splitting function measurements. Geophys. J. Int. 184, 1223–1236. doi:10.1111/j.1365-246X.2010.04884.x

Sakai, T., Ohtani, E., Terasaki, H., Sawada, N., Kobayashi, Y., Miyahara, M., Nishijima, M., Hirao, N., Ohishi, Y., Kikegawa, T., 2009. Fe-Mg partitioning between perovskite and ferropericlase in the lower mantle. Am. Mineral. 94, 921–925. doi:10.2138/am.2009.3123

Scherer, E., Munker, C., Mezger, K., 2001. Calibration of the lutetium-hafnium clock. Science 293, 683–7. doi:10.1126/science.1061372

Sinmyo, R., Hirose, K., 2013. Iron partitioning in pyrolitic lower mantle. Phys. Chem. Miner. 40, 107–113. doi:10.1007/s00269-012-0551-7

Söderlund, U., Patchett, P.J., Vervoort, J.D., Isachsen, C.E., 2004. The ^{176}Lu decay constant determined by Lu–Hf and U–Pb isotope systematics of Precambrian mafic intrusions. Earth Planet. Sci. Lett. 219, 311–324. doi:10.1016/S0012-821X(04)00012-3

Stixrude, L., Hemley, R.J., Fei, Y., Mao, H.K., 1992. Thermoelasticity of silicate perovskite and magnesiowüstite and stratification of the Earth's mantle. Science 257, 1099–1101.

Stixrude, L., Lithgow-Bertelloni, C., 2005. Thermodynamics of mantle minerals - I. Physical properties. Geophys. J. Int. 162, 610–632. doi:10.1111/j.1365-246X.2005.02642.x

Taylor, S.R., McLennan, S.M., 1985. The Continental Crust: its Composition and Evolution, in: Hallan, A. (Ed.), The Continental Crust: Its Composition and Evolution. Blackwell Publishing Ltd, Oxford, pp. 256–276.

Tonks, W.B., Melosh, H.J., 1993. Magma ocean formation due to giant impacts. J. Geophys. Res. 98, 5319–5333.

Van der Hilst, R.D., Widyantoro, S., Engdahl, E.R., 1997. Evidence for deep mantle circulation from global tomography. Nature 386, 578–584.

Vervoort, J.D., Patchett, P.J., Blichert-Toft, J., Albarede, F., 1999. Relationships between Lu–Hf and Sm–Nd isotopic systems in the global sedimentary system. Earth Planet. Sci. Lett. 168, 79–99.

Vervoort, J.D., Plank, T., Prytulak, J., 2011. The Hf–Nd isotopic composition of marine sediments. Geochim. Cosmochim. Acta 75, 5903–5926. doi:10.1016/j.gca.2011.07.046

Walter, M.J., Nakamura, E., Trønnes, R.G., Frost, D.J., 2004. Experimental constraints on crystallization differentiation in a deep magma ocean. Geochim. Cosmochim. Acta 68, 4267–4284. doi:10.1016/j.gca.2004.03.014

Williamson, E.D., Adams, L.H., 1923. Density of the Earth. J. Washingt. Acad. Sci. 13, 413–414.

Wood, B.J., 2000. Phase transformations and partitioning relations in peridotite under lower mantle conditions. Earth Planet. Sci. Lett. 174, 341–354.

Wood, B.J., Rubie, D.C., 1996. The effect of alumina on phase transformations at the 660-kilometer discontinuity from Fe-Mg partitioning experiments. Science (80-.). 273, 1522–1524.

Yu, G., Jacobsen, S.B., 2011. Fast accretion of the Earth with a late Moon-forming giant impact. Proc. Natl. Acad. Sci. U. S. A. 108. doi:10.1073/pnas.1108544108/-/DCSupplemental.www.pnas.org/cgi/doi/10.1073/pnas.1108544108

Zhang, Z., Stixrude, L., Brodholt, J., 2013. Elastic properties of $MgSiO_3$-perovskite under lower mantle conditions and the composition of the deep Earth. Earth Planet. Sci. Lett. 379, 1–12. doi:10.1016/j.epsl.2013.07.034

CHAPTER 3

$^{142}Nd/^{144}Nd$ variations support a Hadean origin of plate tectonics as well as limited preservation of Hadean heterogeneity in the modern mantle

This chapter has been submitted to *Nature Communications* close to its present form. Stein B. Jacobsen was a primary collaborator.

Abstract

Early silicate differentiation events for the terrestrial planets can be traced with the short-lived ^{146}Sm-^{142}Nd system (~100 Myr half-life) by measuring $^{142}Nd/^{144}Nd$. Variations in $^{142}Nd/^{144}Nd$ are also an excellent tracer of the rate of mantle mixing (Jacobsen and Harper, 1996; Jacobsen and Yu, 2015) and thus a potential tracer of plate tectonics through time. Evidence for early silicate differentiation in the Hadean (4.6 to 4.0 Ga) have been provided by $^{142}Nd/^{144}Nd$ measurements of rocks that show both higher and lower values than the present day mantle, demonstrating major silicate Earth differentiation within the first 100 million years of the solar system (Caro et al., 2006; Harper and Jacobsen, 1992). Low $^{142}Nd/^{144}Nd$ provides evidence for the preservation of an early enriched Hadean reservoir (Rizo et al., 2012). In contrast to these $^{142}Nd/^{144}Nd$ variations in early Archean rocks, such $^{142}Nd/^{144}Nd$ variations have not been resolved in rocks younger than 2.7 Ga (Jackson and Carlson, 2012). We have obtained an external 2σ uncertainty better than 1.6 ppm for $^{142}Nd/^{144}Nd$ measurements to constrain level of homogeneity/heterogeneity in the mantle for the last 2 Ga (compared to 5-6 ppm uncertainties in earlier measurements–Boyet and Carlson, 2005; Jackson and Carlson, 2012). We report that most modern day MORB and OIB samples as well as continental crustal rocks going back to 2 Ga are within 1.6 ppm of

the average Earth $^{142}Nd/^{144}Nd$-value. We use a mantle mixing model to show that this is consistent with a mantle stirring time of about 500 Myr since the early Hadean and therefore the Earth's thermal and chemical evolution has been largely regulated by plate tectonics for most of its history. Some young rocks have $^{142}Nd/^{144}Nd$ signatures marginally resolved (~3 ppm), suggesting that the entire mantle is not equally well homogenized and that some silicate mantle signatures from an early differentiated mantle (>4.1 Ga ago) are preserved in the modern mantle.

High-precision measurements of the now extinct ^{146}Sm-^{142}Nd system is an excellent tool for tracing early silicate differentiation processes that occurred within the first 300–500 Ma of solar system history and subsequent mixing through convective processes (Boyet and Carlson, 2005; Burkhardt et al., 2016; Caro et al., 2006; Debaille et al., 2013; Huang et al., 2013). Samarium and Nd are concentrated to different degrees in the melt with respect to the solid during partial melting or fractional crystallization and produce variations in Sm/Nd ratios. Only very early (less than 500 Ma after Earth formation) formed Sm/Nd fractionated reservoirs develop $^{142}Nd/^{144}Nd$ variations while Sm/Nd fractionation throughout Earth history is recorded by the long-lived ^{147}Sm-^{143}Nd system as $^{143}Nd/^{144}Nd$ variations. Variations in $^{142}Nd/^{144}Nd$ are now usually reported as $\mu^{142}Nd = [(^{142}Nd/^{144}Nd_{sample}/^{142}Nd/^{144}Nd_{standard})–1] \times 1{,}000{,}000$, units of "parts per million (ppm)", with respect to the modern terrestrial values as a reference point (Caro et al., 2006; Harper and Jacobsen, 1992; Jackson and Carlson, 2012). The first evidence for early silicate differentiation in the Hadean is evident in 3.8 Ga Greenland Isua supracrustal rocks as

positive μ^{142}Nd-values (>0), preserving a record of the early depleted (high Sm/Nd ratio) mantle (Caro et al., 2006; Harper and Jacobsen, 1992). A complementary, enriched (low Sm/Nd) Hadean mantle reservoir, with negative μ^{142}Nd values is the source of the 3.4 Ga old mafic Greenland Ameralik dikes (Rizo et al., 2012) as well as the mantle source of 3.8 Ga old rocks on the North-east side of the Hudson Bay (O'Neil et al., 2008). The presence of such variations of μ^{142}Nd in rocks formed well after the extinction of ^{146}Sm is a measure of the process of mantle mixing. Subsequent mixing of mantle reservoirs can only result in smaller μ^{142}Nd variations as a function of time, reflecting the extent of mixing, which act as a tracer for geodynamic mixing of enriched and depleted reservoirs (Jacobsen and Harper, 1996). Measurements of μ^{142}Nd by Thermal Ionization Mass Spectrometry (Boyet and Carlson, 2006a; Jackson and Carlson, 2012) of roughly present day rocks, including mantle peridotites, MORBs, OIBs, kimberlites, and continental flood basalts, have not revealed clearly resolved variations at the external reproducibility level of 5–6 ppm (2σ) except for some recent indications from Reunion and Samoa (Horan et al., 2018; Peters et al., 2018) at slightly improved precision. Thus, for the modern mantle, the well-established μ^{142}Nd variations in the oldest Archean rocks have largely been erased. We report new higher-precision ^{142}Nd/^{144}Nd measurements spanning from the present day to 2 Ga ago to further investigate this issue and to assess the extent of mantle mixing, providing a perspective from Nd isotopes to infer whether plate tectonics may have been present since the early Hadean, or whether the changes in the extent of μ^{142}Nd heterogeneity reflect major changes in such processes for the early versus the later Earth (Debaille et al., 2013).

We report ultra-high precision ^{142}Nd/^{144}Nd measurements of terrestrial samples constraining the extent of mantle ^{142}Nd/^{144}Nd heterogeneity through the past 2 Ga. The

μ^{142}Nd values of terrestrial samples are plotted in **Figure 1** relative to the JNdi standard which is assumed to be representative of average mantle. The ^{142}Nd/^{144}Nd measurements (**Appendix II Table 1**) were determined with an external 2σ reproducibility of ~±1.6 ppm. Measurements were performed with our Phoenix Isotopx Thermal Ionization Mass Spectrometer, using a dynamic measurement procedure to cancel out differences in detector efficiencies. Measurements of the long-lived ^{147}Sm-^{143}Nd system are also reported (**Appendix II Table 2**) to use the ε^{143}Nd value (= [(^{143}Nd/^{144}Nd$_{sample}$ / ^{143}Nd/^{144}Nd$_{CHUR}$)–1] x 10,000) to determine whether the mantle source of the samples had long-term enrichment (ε^{143}Nd < 0) or depletion (ε^{143}Nd > 0) of a light-rare earth enriched component (typical for melts). MORB samples include HIMU, enriched mantle 1 (EM1) and the depleted MORB mantle (DMM) whose ε^{143}Nd values are > 10, with the exception of an EM1 MORB with a low ε^{143}Nd-value of +0.8. A depleted N-MORB, is barely resolved to be 3 ppm lower (2σ = 1.2) in μ^{142}Nd than the **JNdi** standard, determined at a long-term reproducibility of better than 1.6 ppm. In contrast, all our other modern MORB and OIB measurements agree to within ±1.6 ppm of the JNdi standard. This includes a highly depleted MORB sample from the Gakkel ridge free of hot spot influence; an EM1 MORB, and Iceland and Hawaii samples. The enriched ^{142}Nd/^{144}Nd signature (μ^{142}Nd <0) in a depleted MORB sample indicates the decoupling of the long-lived ^{147}Sm-^{143}Nd and short-lived ^{146}Sm-^{142}Nd systems, reflecting the complex history of the mantle where an initially enriched mantle reservoir is recycled to later become depleted by melt extraction.

A number of continental crustal samples were selected to cover the age range from 300 Ma to 2 Ga; they are all from the Baltic Shield area and range in compositions from gabbroic to granitic. They are representative of the established ^{143}Nd/^{144}Nd evolution of the

source of the Baltic Shield through this time period and also similar to the global evolution (Andersen and Sundvoll, 1995). They all have μ^{142}Nd-values within ±1.6 ppm (2σ) of the JNdi standard (**Figure 1**). We conclude from our new data that generally the mantle has had a μ^{142}Nd-value within ±1.6 ppm for the past 2 Ga, while some slightly larger heterogeneities may exist. The $^{142}Nd/^{144}Nd$ uniformity for the past 2 Ga is in strong contrast to pre-2.5 Ga data where $^{142}Nd/^{144}Nd$ variations are the rule rather than the exception. This is shown in **Figure 2** where the μ^{142}Nd data (green squares) reported here for samples in the age range 0 to 2 Ga are compared to published μ^{142}Nd data for Archean rocks of 2.7 to 4.0 Ga age (blue circles). It is well accepted that the Earth's thermal and chemical evolution has been largely regulated by plate tectonics for the past 2 Ga, but it is debated for earlier times. The preservation of significant $^{142}Nd/^{144}Nd$ heterogeneities in the mantle until 2.7 Ga ago has been used to argue that throughout the Hadean and Archean, Earth was characterized by a stagnant-lid regime, possibly with sporadic and short subduction episodes (Debaille et al., 2013). Such a stagnant lid regime would seem to be inconsistent with geological evidence that Phanerozoic-like plate tectonics were operating already ~3.8 billion years ago (Furnes et al., 2007).

Plate tectonics is today the surface manifestation of mantle convection and mixing, but is not the only possible mode of plate-mantle interaction which translate to different mantle mixing rates (Debaille et al., 2013) at earlier times (Crowley and O'Connell, 2012). The $^{142}Nd/^{144}Nd$ record can be used with a statistical, stochastic model (Jacobsen and Yu, 2015) modified from (Kellogg et al., 2007) to infer the rate of mantle mixing and therefore used to infer the surface tectonic style (Debaille et al., 2013). The model assumes upper and lower mantle reservoirs that are initially uniform in isotopic composition, formed essentially at the

origin of a fully grown Earth. The upper and lower mantle volumes are set up to represent the early (Hadean) enriched (EEM), and early depleted mantle reservoirs (EDM), respectively, most likely formed as the result of magma ocean differentiation. The model assumes mixing of the whole mantle, with a stirring rate τ, resulting in stretching and thinning of layers with an initial heterogeneity length scales of $l_{0\text{-}upper}$ and $l_{0\text{-}lower}$. The short-length scales of the mantle reservoirs are stretched and thinned such that it decays exponentially as a function of time t, $l_t = l_0 e^{-t/\tau}$, due to toroidal motion. A sampling box simulating a melting column is placed randomly in the mixture of stretched reservoirs. As the relative sizes of the reservoirs are initially much larger than the length scale of sampling, sampled isotopic signatures demonstrate a bimodal distribution of heterogeneities in the first few hundred million years of this model, as shown in **Figure 2**. We assume that the μ^{142}Nd of EEM would be –20 and μ^{142}Nd of EDM would be +20 after the decay of ^{146}Sm, if there were no mixing of the two mantles. The complete set of parameters used are given in the **Methods** section. The model results are shown in **Figures 2 and 3** as purple crosses as a function of time for a uniform mantle stirring rate (τ) of 500 Myr. At early times, prior to 4 Ga, the model shows that one will expect to see the full range of μ^{142}Nd for a mixing rate that is similar to that of the modern plate tectonic cycle. This justifies our choice of initial μ^{142}Nd-values for the Hadean mantle reservoirs. Large variations are present through most of the Archean (±20 ppm), up to the Late Archean at 2.7 Ga, where the combination of Theo's flow and Hudson Bay reveals a combined variation of up to 23 ppm (Debaille et al., 2013; O'Neil and Carlson, 2017), which when compared to our new data document a rapid changeover between this time and 2 Ga. For a convectively stirred mantle with a 500 Myr stirring rate, there is such a rapid changeover from an Archean μ^{142}Nd heterogeneous mantle

to a μ^{142}Nd homogenous post-Archean mantle (**Figure 2**). The broad ranges of μ^{142}Nd values are observed to converge into a limited distribution of values at around 2 Ga, predicting a relatively quick change from a wide range of μ^{142}Nd values (40 ppm maximum range at 3 Ga) into a much smaller range of ±1.8 ppm (2σ) at 2.17 Ga. In this model, this results when the layers in the mantle, carrying the Hadean ^{142}Nd/^{144}Nd signatures, are sufficiently thin that sampling of the mantle by basalt melt extraction always gives the average value. Once the average ^{142}Nd/^{144}Nd of a sampling box is no longer distinguishable from one another after repeat sampling procedures on the scale of the sampling box (melting column), the terrestrial mantle can be deduced to be homogeneous on the length scale of melting (**Methods Figure S3c**).

Ultra-high precision measurements of Phanerozoic and Proterozoic samples are compared with model results in **Figure 3**. Most samples that are measured in this study are shown to cluster around μ^{142}Nd = 0 and these results support using JNdi as representative of μ^{142}Nd in the average modern mantle. While the Proterozoic μ^{142}Nd data all are within ±1.6 ppm, most of the data plot above the average modern mantle while one 1.08 Ga sample plots significantly below these values. This may suggest that 1.08 Ga old sample records a mantle that is different from the main trend of the samples. These small μ^{142}Nd variations are contrary to predictons from the model and may, if correct, suggest that some domains of the modern mantle are not as well mixed as the dominant part of the mantle producing magmas.

Histograms of μ^{142}Nd-values for rocks whose ages are about 3.8 and 2.7 Ga are shown in **Figure 4** (panels **a** and **c**). They are compared with synthetic histograms (panels **b** and **d** of **Figure 4**) predicted from the model with a mantle stirring rate of 500 Myr and are results

from the same calculation shown in **Figure 2**. The data from the 3.7–3.9 Ga time window show a bimodal distribution. The model results in panel **b** exhibit a bi-modal distribution. The difference reflects the assumption of initial μ^{142}Nd values of –20 and +20 of upper and lower mantles. To get a better match one could invoke a slightly faster stirring rate (<500 Myr) in the Hadean or two initially heterogeneous reservoirs. The data in panel **c** and the model results in **d** for 2.7 Ga gives a much better match showing that a stirring rate of about 500 Myr is needed to explain the overall pattern of ^{142}Nd/^{144}Nd through Earth history. The difference between the 3.8 Ga data and model will not alter this conclusion. As the early enriched and early depleted reservoirs are gradually stretched and thinned due to convection, the mantle is gradually homogenized, and the μ^{142}Nd changeover from an early heterogenous distribution to a late (after 2.7 Ga and is essential gone by 2 Ga – see **Figures 2** and **3**) homogenization of μ^{142}Nd happens rapidly. The sensitivity of the isotopic pattern to the mantle stirring rate is shown in the lower panel of **Figure 2**. A mantle mixing time of about 500 Myr since the early Hadean is thus broadly consistent with the pattern of μ^{142}Nd in rocks through time. This value is typical for modern plate tectonics (Kellogg et al., 2007); therefore μ^{142}Nd data are consistent with the Earth's thermal and chemical evolution being continually regulated, through a mechanism such as plate tectonics for most of Earth's history. The combination of a wide range of μ^{142}Nd variations prior to about 2.7 Ga as well as their duration throughout the Archean require one or more massive initial differentiation events, through an event such as the formation of an early magma ocean. Subsequent to that early massive differentiation, our model demonstrates that there is no need for the currently proposed stagnant lid (Debaille et al., 2013) or sluggish tectonics (Caro et al., 2017) to explain the ^{142}Nd/^{144}Nd record in rocks through time. The ^{142}Nd/^{144}Nd evidence consistent

with plate tectonics and geology evidence (Furnes et al., 2007) back to 3.8 Ga, and requires the mixing process to start shortly after the initial magma ocean differentiation event that resulted in the ^{142}Nd heterogeneities in the early mantle. The general lack of μ^{142}Nd variations in young rocks suggests that the early magma ocean structure has been thoroughly mixed between the upper and lower mantles.

References

Andersen, T., Sundvoll, B., 1995. Neodymium isotope systematics of the mantle beneath the Baltic shield: Evidence for depleted mantle evolution since the Archean. Lithos 35, 235–243.

Bennett, V.C., Brandon, A.D., Nutman, A.P., 2007. Coupled ^{142}Nd-^{143}Nd Isotopic Evidence for Hadean Mantle Dynamics. Science (80-.). 318, 1907–1910. https://doi.org/10.1126/science.1145928

Boyet, M., Carlson, R., 2006a. A new geochemical model for the Earth's mantle inferred from ^{146}Sm–^{142}Nd systematics. Earth Planet. Sci. Lett. 250, 254–268. https://doi.org/10.1016/j.epsl.2006.07.046

Boyet, M., Carlson, R., 2006b. A new geochemical model for the Earth's mantle inferred from ^{146}Sm–^{142}Nd systematics. Earth Planet. Sci. Lett. 250, 254–268. https://doi.org/10.1016/j.epsl.2006.07.046

Boyet, M., Carlson, R.W., 2005. ^{142}Nd Evidence for Early (4.53 Ga) Global Differentiation of the Silicate Earth. Science (80-.). 309, 576–581. https://doi.org/10.1126/science.1113634

Burkhardt, C., Borg, L.E., Brennecka, G. a., Shollenberger, Q.R., Dauphas, N., Kleine, T., 2016. A nucleosynthetic origin for the Earth's anomalous ^{142}Nd composition. Nature 537, 394–398. https://doi.org/10.1038/nature18956

Caro, G., Bourdon, B., Birck, J.-L., Moorbath, S., 2006. High-precision ^{142}Nd/^{144}Nd measurements in terrestrial rocks: Constraints on the early differentiation of the Earth's mantle. Geochim. Cosmochim. Acta 70, 164–191. https://doi.org/10.1016/j.gca.2005.08.015

Caro, G., Morino, P., Mojzsis, S.J., Cates, N.L., Bleeker, W., 2017. Sluggish Hadean geodynamics: Evidence from coupled ^{146,147}Sm-^{142,143}Nd systematics in Eoarchean supracrustal rocks of the Inukjuak domain (Quebec). Earth Planet. Sci. Lett. 457, 23–

37. https://doi.org/10.1016/j.epsl.2016.09.051

Crowley, J.W., O'Connell, R.J., 2012. An analytic model of convection in a system with layered viscosity and plates. Geophys. J. Int. 188, 61–78. https://doi.org/10.1111/j.1365-246X.2011.05254.x

Debaille, V., O'Neill, C., Brandon, A.D., Haenecour, P., Yin, Q.Z., Mattielli, N., Treiman, A.H., 2013. Stagnant-lid tectonics in early Earth revealed by ^{142}Nd variations in late Archean rocks. Earth Planet. Sci. Lett. 373, 83–92. https://doi.org/10.1016/j.epsl.2013.04.016

Furnes, H., Wit, M. De, Staudigel, H., Rosing, M.T., Muehlenbachs, K., 2007. A vestige of Earth's oldest ophiolite. Science (80-.). 315, 2001–2004. https://doi.org/10.1126/science.1139170

Harper, C.L.J., Jacobsen, S.B., 1992. Evidence from coupled ^{147}Sm-^{143}Nd and ^{146}Sm-^{142}Nd systematics for very early (4.5-Gyr) differentiation of the Earth's mantle. Nature 360, 726–732.

Horan, M.F., Carlson, R.W., Walker, R.J., Jackson, M., Garçon, M., Norman, M., 2018. Tracking Hadean processes in modern basalts with 142-Neodymium. Earth Planet. Sci. Lett. 484, 184–191. https://doi.org/10.1016/j.epsl.2017.12.017

Huang, S., Jacobsen, S.B., Mukhopadhyay, S., 2013. ^{147}Sm-^{143}Nd systematics of Earth are inconsistent with a superchondritic Sm/Nd ratio. Proc. Natl. Acad. Sci. U. S. A. 110, 4929–34. https://doi.org/10.1073/pnas.1222252110

Jackson, M.G., Carlson, R.W., 2012. Homogeneous superchondritic ^{142}Nd/^{144}Nd in the mid-ocean ridge basalt and ocean island basalt mantle. Geochemistry, Geophys. Geosystems 13, 1–10.

Jacobsen, S.B., Harper, C.L., 1996. Earth Processes: Reading the Isotopic Code, in: Basu, A., Hart, S. (Eds.), . Geophysical Mongraph 95.

Jacobsen, S.B., Yu, G., 2015. Extinct isotope heterogeneities in the mantles of Earth and Mars: implications for mantle stirring rates. Meteorit. Planet. Sci. 50, 555–567.

Kellogg, J.B., Jacobsen, S.B., O'Connell, R.J., 2007. Modeling lead isotopic heterogeneity in mid-ocean ridge basalts. Earth Planet. Sci. Lett. 262, 328–342. https://doi.org/10.1016/j.epsl.2007.06.018

Maya, J.M., Bhutani, R., Balakrishnana, S., Rajee Sandhya, S., 2017. Petrogenesis of 3.15 Ga old Banasandra komatiites from the Dharwar craton, India: Implications for early mantle heterogeneity. Geosci. Front. 8, 467–481.

O'Neil, J., Carlson, R.W., 2017. Building Archean cratons from Hadean mafic crust. Science (80-.). 355, 1199–1202.

O'Neil, J., Carlson, R.W., Francis, D., Stevenson, R.K., 2008. Neodymium-142 Evidence for Hadean Mafic Crust. Science (80-.). 321, 1828–1832. https://doi.org/10.1126/science.1161925

O'Neil, J., Rizo, H., Boyet, M., Carlson, R.W., Rosing, M.T., 2016. Geochemistry and Nd isotopic characteristics of Earth's Hadean mantle and primitive crust. Earth Planet. Sci. Lett. 442, 194–205. https://doi.org/10.1016/j.epsl.2016.02.055

Peters, B.J., Carlson, R.W., Day, J.M.D., Horan, M.F., 2018. Hadean silicate differentiation preserved by anomalous142Nd/144Nd ratios in the Réunion hotspot source. Nature 555, 89–93. https://doi.org/10.1038/nature25754

Rizo, H., Boyet, M., Blichert-Toft, J., O'Neil, J., Rosing, M.T., Paquette, J.-L., 2012. The elusive Hadean enriched reservoir revealed by ^{142}Nd deficits in Isua Archaean rocks. Nature 491, 96–100. https://doi.org/10.1038/nature11565

Rizo, H., Boyet, M., Blichert-Toft, J., Rosing, M., 2011. Combined Nd and Hf isotope evidence for deep-seated source of Isua lavas. Earth Planet. Sci. Lett. 312, 267–279.

Rizo, H., Boyet, M., Blichert-Toft, J., Rosing, M.T., 2013. Early mantle dynamics inferred from ^{142}Nd variations in Archean rocks from southwest Greenland. Earth Planet. Sci. Lett. 377–378, 324–335. https://doi.org/10.1016/j.epsl.2013.07.012

Rizo, H., Walker, R.J., Carlson, R.W., Touboul, M., Horan, M.F., Puchtel, I.S., Boyet, M., Rosing, M.T., 2016. Early Earth differentiation investigated through ^{142}Nd, ^{182}W, and highly siderophile element abundances in samples from Isua, Greenland. Geochim. Cosmochim. Acta 175, 319–336. https://doi.org/10.1016/j.gca.2015.12.007

Roth, A.S.G., 2014. Combined ^{147,146}Sm-^{143,142}Nd constraints on the longevity and residence time of early crust. Geochemistry, Geophys. Geosystems 15, 2329–2345. https://doi.org/10.1002/2014GC005313.Received

Roth, A.S.G., Bourdon, B., Mojzsis, S.J., Touboul, M., Sprung, M., Guitreau, P., Blichert-Toft, J., 2013. Inherited ^{142}Nd anomalies in Eoarchean protoliths. Earth Planet. Sci. Lett. 361, 50–57.

Schneider, K.P., Hoffmann, J.E., Boyet, M., Munker, C., 2018. Coexistence of enriched and modern-like ^{142}Nd signatures in Archean igneous rocks of the eastern Kaapvaal Craton, southern Africa. Earth Planet. Sci. Lett. 487, 54–66.

FIGURES

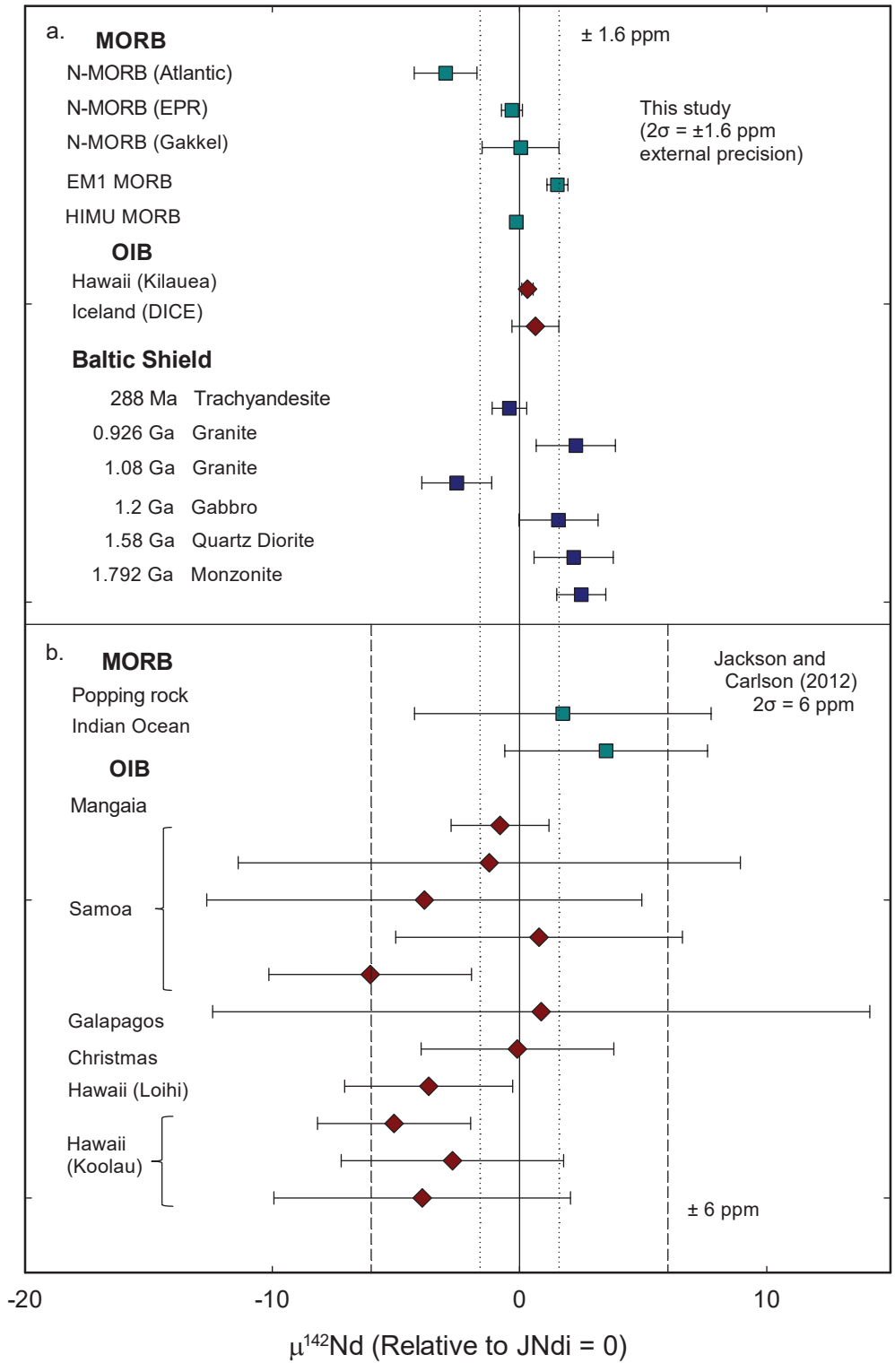
a.
MORB
N-MORB (Atlantic)
N-MORB (EPR)
N-MORB (Gakkel)
EM1 MORB
HIMU MORB
OIB
Hawaii (Kilauea)
Iceland (DICE)
Baltic Shield
288 Ma Trachyandesite
0.926 Ga Granite
1.08 Ga Granite
1.2 Ga Gabbro
1.58 Ga Quartz Diorite
1.792 Ga Monzonite
± 1.6 ppm
This study
(2σ = ±1.6 ppm
external precision)
b.
MORB
Popping rock
Indian Ocean
OIB
Mangaia
Samoa
Galapagos
Christmas
Hawaii (Loihi)
Hawaii
(Koolau)
Jackson and
Carlson (2012)
2σ = 6 ppm
± 6 ppm
-20
-10
0
10
μ142Nd (Relative to JNdi = 0)

Figure 1. μ^{142}Nd values of terrestrial samples plotted relative to the JNdi standard which is assumed to be representative of the average mantle. Dotted lines indicate our measured 2σ uncertainty of ±1.6 ppm for this standard. a. New measurements from this study: Modern day MORBs are shown in green squares, OIBs in red diamonds, continental crustal samples whose ages range from 288 Ma to 1.792 Ga are shown in blue squares. All of these samples are within the ±1.6 ppm 2σ error of the JNdi standard, except for one Atlantic N-MORB sample which is slightly lower and outside the 2σ uncertainty of JNdi. b. Plotted for comparison are the data of an earlier study reporting μ^{142}Nd measurements for a variety of modern day MORBs and OIBs, at 2σ = ±6 ppm external precision (Jackson and Carlson, 2012). We conclude from our new data that the mantle has had a μ^{142}Nd-value within ±1.6 ppm for the past 2 Ga, while some slightly larger heterogeneities may exist. Recent studies of Reunion and Samoa (Horan et al., 2018; Peters et al., 2018) support this conclusion.

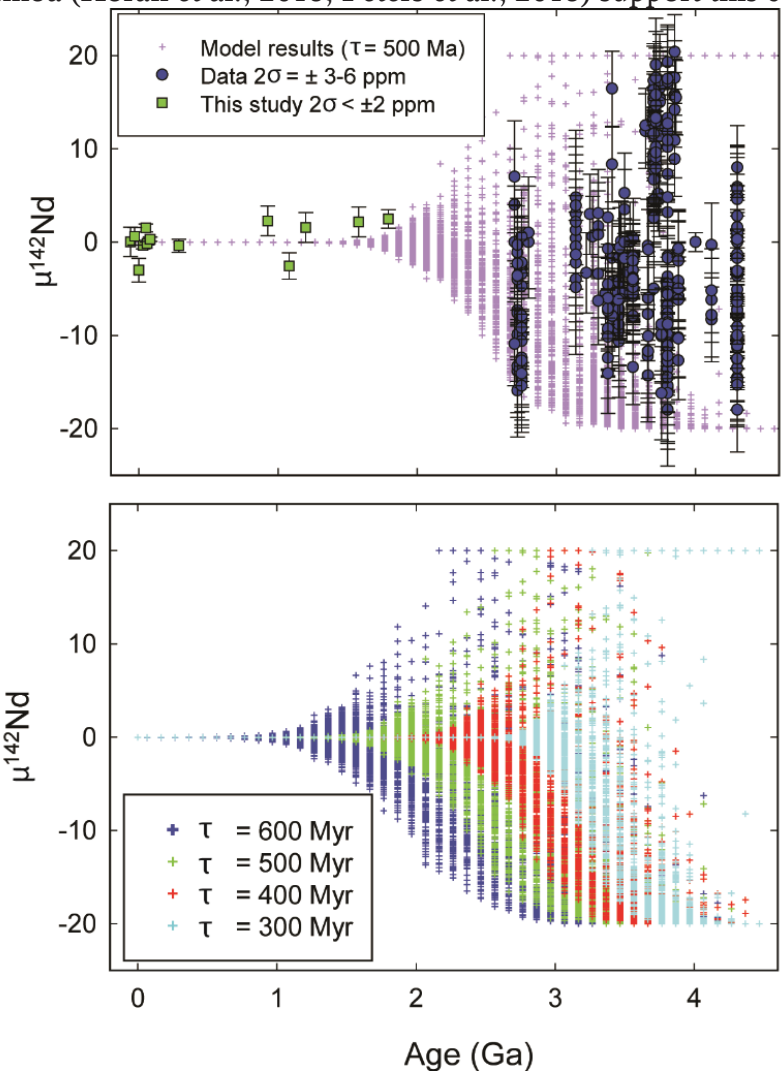

Figure 2. In the upper panel, the μ^{142}Nd data (green squares) reported here for sample on the age range 0 to 2 Ga are compared to published μ^{142}Nd data for Archean rocks of 2.7 to 4.0 Ga age (blue circles – Bennett et al., 2007; Boyet and Carlson, 2006b; Caro et al., 2017, 2006; Debaille et al., 2013; Maya et al., 2017; O'Neil et al., 2016, 2008; O'Neil and Carlson, 2017;

Rizo et al., 2013, 2012, 2011, 2016; Roth, 2014; Roth et al., 2013; Schneider et al., 2018). Modern day measured samples of this study (green squares), which are clustered around $T = 0$, are slightly offset from 0 to better exhibit the distribution of the data in comparison to model results. The data are compared to a results from a model for mantle mixing (Jacobsen and Yu, 2015). The rapid changeover happens when the layers in the convectively stirred mantle are sufficiently thin that sampling of the mantle by basalt melt extraction will always only give the average value. At early times one will expect to see the full range of μ^{142}Nd for a mixing rate that is similar to that of the modern plate tectonic cycle. The lower panel shows the sensitivity of the time of change-over to a uniform μ^{142}Nd-value to the stirring rate.

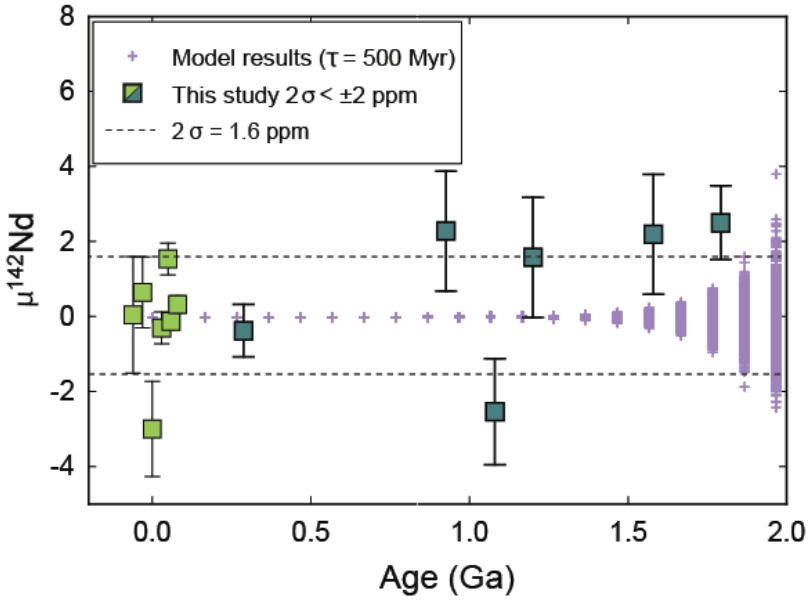

Figure 3. μ^{142}Nd modern MORB and OIB sample measurements of this study (green squares), compared to the last 2 Ga of the evolution diagram in **Figure 2**. The modern day data ($T = 0$) are offset from zero for clarity. Samples whose ages are older than 288 Ma are shown in blue squares. The $2\sigma = \pm 1.6$ ppm error band around 0 is indicated with broken lines. The model results from **Figure 2** are plotted in purple for comparison. A 500 Ma stirring rate is consistent with the constraint of the mantle μ^{142}Nd-value being with ±1.6 ppm of the JNdi standard for the past 2.0 Ga.

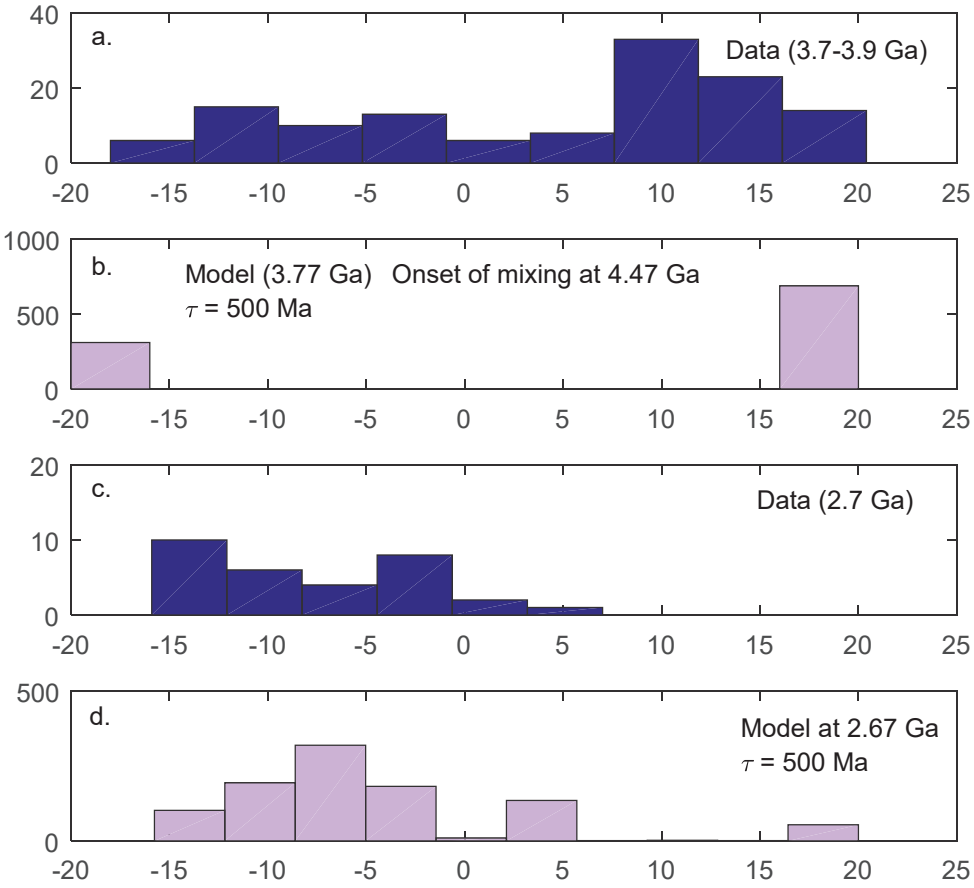

Figure 4. Comparison of μ^{142}Nd histograms for two times (panels **a** and **c**) with μ^{142}Nd histogrames predicted from the model with a mantle stirring rate of 500 Myr (panels **b** and **d**). A mantle mixing time of about 500 Myr since the early Hadean is broadly consistent with the pattern of μ^{142}Nd in rocks through time. This value is typical for modern plate tectonics (Kellogg et al., 2007); therefore μ^{142}Nd data are consistent with the Earth's thermal and chemical evolution being largely regulated by plate tectonics for most of Earth's history.

Methods

Sample digestion and chemical separation of Nd and Sm

Samples (~100 mg) were dissolved in a mixture of concentrated HF and HNO_3 (1:4 ratio) using a CEM microwave system. The temperature is ramped to 180 ºC in a span of 20 mins, and held at 1 hr, then ramped down to room temperature. The solution was dried down on hot plates slowly at low temperature (~80 ºC) and then redissolved in a mixture of concentrated HCl, HNO_3, and MilliQ water (1:4:1) mixture using the microwave setup. Samples that formed precipitates were repeatedly dissolved using the second step in different ratios of HCl to HNO_3 to ensure complete dissolution.

The dissolved samples were processed through ion exchange chemistry using BioRad AG50WX8 Resin (100-200 mesh). The Teflon/Quartz ion exchange columns have a 1 cm internal diameter 30 cm in length. The separated collection of rare earth elements (REE) were then treated with 30% H_2O_2 and further dried down and passed through 30 cm long REE columns with BioRad AG50WX8 Resin (200-400 mesh) whose internal diameters were 2 mm, to separate Nd from other REEs with 2-methylactic acid (0.2 M) calibrated at a pH of 4.62, air pressurized to have a ~1 drop/min drop rate (~43.1 µL/drop). Samples were passed twice through the columns. Nd concentrations of pre-cuts, post-cuts, and a small fraction of the collected aliquot were measured with a Thermo iCAP-Q quadrupole ICP-MS, to be compared to a fraction of the Nd cut to ensure that the collected aliquot contained 98% of the Nd from the sample.

Mass spectrometry

$^{147}Sm/^{144}Nd$ ratios were determined from concentration measurements of small dissolved aliquots of whole rock samples measured for major and trace elements using a Thermo iCAP-Q quadrupole ICP-MS. Standards, blanks, and standards were doped with 10 ppb In for drift corrections.

In order to make $^{142}Nd/^{144}Nd$ measurements, the Nd aliquots that were purified through column chromatography (~1000-1500 ng) were loaded on a single 99.999% Re filament zone refined filament (H Cross, USA) at ~1.0 A, with a 2:1 ratio mixture of sample solution to 0.1 N H_3PO_4 acid. The sample was heated at 1.3 A for 2 ½ to 3 minutes, after which it was flashed at a dull red (~2 A) for 3 seconds to burn off organics and evaporate phosphoric acid. The loading technique was important in consistency of runs and preventing reverse fractionation. Samples were loaded in six increments for every 1 μL of solution with a consistent evaporation time of 45 secs in between loads. Sample loading was focused on the middle of the filament, where loads overlapped on top of one another.

The Nd isotope measurements were carried with our Isotopx Phoenix TIMS (thermal ionization mass spectrometer) in two-step multi-dynamic mode with 10^{11} Ω resistors. A Gains calibration was carried out prior to each measurement. The filaments were configured in a triple filament arrangement, with two side posts and one center post. The side filaments were ramped to an average of 2.3A and the center up to 4.5A. High ion beam signals (>1 V) at low side-filament intensity (1.8 A), indicating early burn-off from a small reservoir, was treated by preheating the sample from 5 to 8 hours at 5 to 20 mV. Then isotope data were collected at 5 (n=3), 6 (n=2) or 7 V (n=55) for with an integration time of 10 secs per cycle. Prior to each block consisting of 10 cycles for each sequence, half-mass baseline

measurements were carried out for 10 secs with an automatic peak centering routine. The number of cycles for each sample ranged from 150 to 2000 cycles, with an average of 500.

Typical ^{142}Ce interferences for ^{142}Nd were less than 1 ppm, as with ^{144}Sm interferences for ^{144}Nd. The ion exchange column cut was selected to be wide rather than narrow in order to avoid potential fractionation effects due to incomplete collections. Thus ^{144}Sm interferences for the measurements of CH59-2 and one measurement of HLY102-096 and K1714 each were detected to range from 100-400 ppm even after two passes. The high interference measurements of HLY102-096, as well as of K1714, were observed to agree within 1.6 ppm of other low interference (<1 ppm) measurements of the same samples.

We describe two procedures for data reduction by measurement of ^{142}Nd/^{144}Nd involving two data collections sequences (labeled S1 and S2). We used two multi-dynamic data reduction methods here called "Reduction 1: RED1" and "Reduction 2: RED2" for purposes of distinction. Two reduction methods can be derived from the same set-up. The sequence steps are off-set by two mass units as noted in the table below.

	L2	Ax	H1	H2	H3	H4	H5	H6
Sequence 1	^{140}Ce	^{142}Nd	^{143}Nd	^{144}Nd	^{145}Nd	^{146}Nd	^{147}Sm	^{148}Nd
Sequence 2	^{142}Nd	^{144}Nd	^{145}Nd	^{146}Nd	^{147}Sm	^{148}Nd		^{150}Nd

Multidynamic reduction RED1: The data collection sequence (S1) is the measurement of ^{142}Nd and ^{144}Nd in the Ax and H2 cups. The isotopic ratio is calculated from the ion beam intensities (*I*) and the cup efficiency factors (*f*). The second data collection sequence (S2) is the measurement of ^{144}Nd and ^{146}Nd in the Ax and H2 cups. The cup factors can be directly cancelled out:

$$\left(\frac{^{142}Nd^{(S1)}(t_1)}{^{144}Nd^{(S2)}(t_1)}\right)_M = \frac{I_{142}^{(S1)}(t_1)}{I_{144}^{(S2)}(t_1)} \times \frac{f_{Ax}}{f_{Ax}} = \frac{I_{142}^{(S1)}(t_1)}{I_{144}^{(S2)}(t_1)}$$

$$\left(\frac{^{146}Nd^{(S2)}(t_1)}{^{144}Nd^{(S1)}(t_1)}\right)_M = \frac{I_{146}^{(S2)}(t_1)}{I_{144}^{(S1)}(t_1)} \times \frac{f_{H2}}{f_{H2}} = \frac{I_{146}^{(S2)}(t_1)}{I_{144}^{(S1)}(t_1)}$$

The standard way is to use a time interpolation method based on repeated measurement of a reference peak. Assuming that the data follow the exponential law, the RED1 method gives:

$$\left(\frac{^{142}Nd}{^{144}Nd}\right)_M^{\exp(RED1)} = \frac{I_{142}^{(S1)}(t_1)}{I_{144}^{(S2)}(t_1)}\left[\frac{\frac{I_{146}^{(S2)}(t_1)}{I_{144}^{(S1)}(t_1)}}{0.7219}\right]^{-p}$$

the exponent, p is given by:

$$p = \frac{\ln(m_{142Nd}/m_{144Nd})}{\ln(m_{146Nd}/m_{144Nd})} = \frac{\ln(141.907729/143.910093)}{\ln(145.913123/143.910093)} = -1.0137$$

where the m's represent the masses of the individual isotopes.

Multidynamic reduction RED2: In this method, the ratio obtained from the first sequence (S1) is by measurement of ^{142}Nd and ^{144}Nd in the Ax and H2 cups. The second scan is the measurement of ^{144}Nd and ^{146}Nd in the Ax and H2 cups. Thus:

$$\left(\frac{^{142}Nd}{^{144}Nd}\right)_M^{(S1)} = \frac{I_{142}^{(S1)}(t_1)}{I_{144}^{(S1)}(t_1)} \times \frac{f_{Ax}}{f_{H2}}$$

$$\left(\frac{^{146}Nd}{^{144}Nd}\right)_M^{(S2)} = \frac{I_{146}^{(S2)}(t_2)}{I_{144}^{(S2)}(t_2)} \times \frac{f_{H2}}{f_{Ax}}$$

If we assume that the data follow the exponential law, then there is not complete cancellation of cup factors:

$$\left(\frac{^{142}Nd}{^{144}Nd}\right)_M^{\exp(RED2)} = \frac{I_{142}^{(S1)}(t_1)}{I_{144}^{(S1)}(t_1)} \times \frac{f_{Ax}}{f_{H2}}\left[\frac{\frac{I_{146}^{(S2)}(t_2)}{I_{144}^{(S1)}(t_2)} \times \frac{f_{H2}}{f_{Ax}}}{0.7219}\right]^{-p}$$

The cup factors can be factored out separately:

$$\left(\frac{^{142}Nd}{^{144}Nd}\right)_M^{\exp(RED2)} = \frac{I_{142}^{(S1)}(t_1)}{I_{144}^{(S1)}(t_1)}\left[\frac{\frac{I_{146}^{(S2)}(t_2)}{I_{144}^{(S1)}(t_2)}}{0.7219}\right]^{-p}\left(\frac{f_{H2}}{f_{Ax}}\right)^{-1-p}$$

where

$$\left(\frac{f_{H2}}{f_{Ax}}\right)^{-1-p}$$

is the unknown cup factor ratio.

The two drift correction methods are distinguished by the unknown cup factor ratio, which can be calibrated by comparing the ratios of the intensities of ^{144}Nd(S1) versus ^{144}Nd(S2).

"Drift corrections": For both methods, the data are corrected for drift correction by using time interpolation to correct for either intensity changes or ratio changes. Drift corrections are necessary for each of the two different reduction methods. As the ^{144}Nd signals for Sequence 1 and Sequence 2 in the RED1 method are different due to the change of signal intensity with time, the results are corrected to accommodate the change in the intensity of the signal as a function of time. On the other hand, the drift for the RED2 is corrected with respect to the time dependence of ratios, as the ^{142}Nd/^{144}Nd and ^{146}Nd/^{144}Nd ratios are being measured at different times. Drift corrections for the change of intensity are made based on ^{146}Nd, which has no mass interferences. Intensities from Sequence 1 and Sequence 2 throughout one block measurement (Sequence 1 and Sequence 2 signals alternating in 20 cycles) are interpolated with a least-squares fitting with a fourth order polynomial. Using this fitting, the intensity of the ^{142}Nd, ^{144}Nd, and ^{146}Nd beams are normalized to the first intensity from the block. For blocks of each run, each polynomial is

manually checked through plots to ensure the polynomial function is capable of reasonably accommodating the intensity drift. Poorly fitted points or blocks are eliminated from data reduction. Interference corrections are applied after drift corrections.

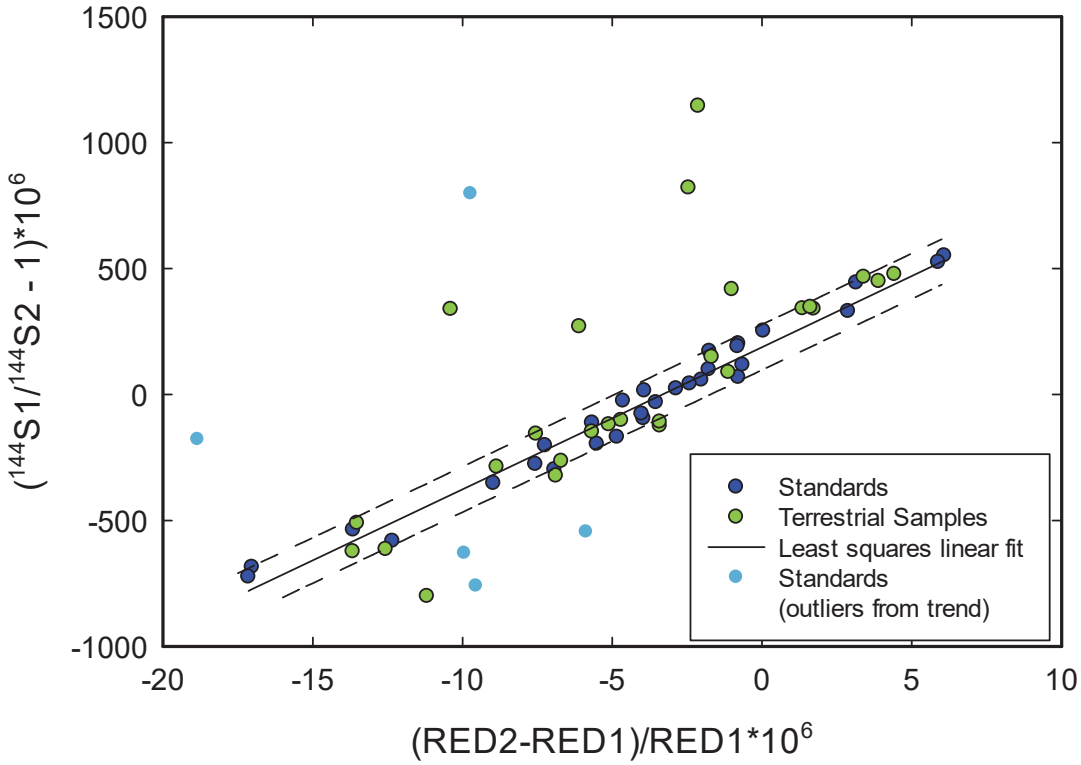

Fig. S1. This plot demonstrates the relationship between RED1 and RED2 as predicted through the derived reduction methods. The discrepancy in $^{142}Nd/^{144}Nd$ values from the different reduction methods (labeled as "RED1" or "RED2" in plot; *x*-axis) demonstrate a correlation with the cup factors (*y*-axis; here "$^{144}S_n$" signifies the ^{144}Nd intensity of Sequence "*n*," where *n* is 1 or 2) shown here in this figure. We find that RED2 produces more dispersion in $^{142}Nd/^{144}Nd$ values in comparison to RED1 (demonstrating a $2\sigma \leq \pm 1.6$ reproducibility), whose cup factors cancel out. Regardless of the whether the data fall on the trend, all standards here demonstrate $2\sigma \leq \pm 1.6$ external reproducibility with RED1. The least-squares fit to the standards that fit the trend as indicated in dark blue reveal an equation of $y = 56.42x + 187.2$. The internal 1σ standard errors for the *y*-axis vary between ~10 and 100. The regression line is bracketed by ±1.6 ppm in the *x*-axis direction. Terrestrial sample measurements that are offset from the trend include one measurement of the following samples: DICE, HLY102-096, RAM-3, and E-58, and two GN-12-03 measurements.

Model parameters and calculations

Model set-up

We use the short-lived ^{146}Sm-^{142}Nd system as an isotope tracer for assessing the extent of mixing(Kellogg et al., 2007, 2002) in the mantle using a simplified set-up(Jacobsen and Yu, 2015) summarized as follows. The terrestrial mantle is assumed to differentiate into two homogeneous layers 100 Ma after solar system history, corresponding roughly to the mass of the upper and lower mantles to represent the early enriched mantle (EEM) and early depleted mantle (EDM) reservoirs, respectively. Here the length scale of heterogeneity is determined by the short-length of the reservoir, corresponding to the thickness of the layer, which decreases exponentially as a function of time.

Fig. S2.

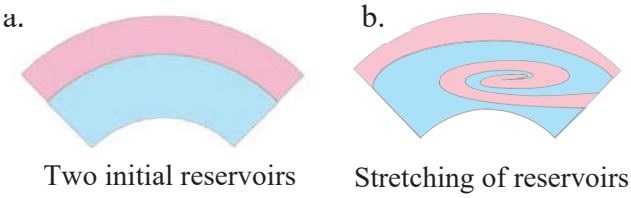

A melting event is represented by a sampling box that is 100 km in each dimension, which is placed in a mixture of cubes of reservoirs Figure S3(a). This process is repeated 1000 times for each time step for every 100 Myr from the timing of differentiation ($T_{4.47Ga}$) to present day (T_0). The resulting isotopic composition from the sampling box is calculated from the averaged isotopic compositions of the EEM and EDM and their corresponding volumetric proportions present in the box.

Fig. S3.

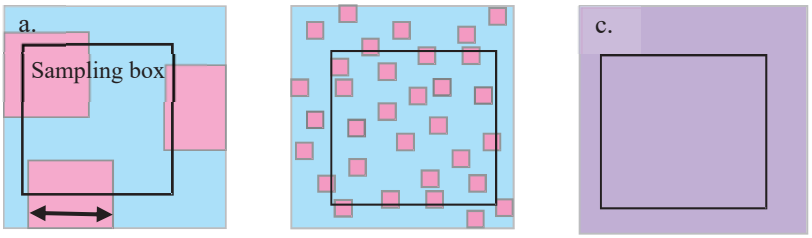

Length scale of heterogeneity

a. at $T_{a\ Ga}$

b. at $T_{b\ Ga}$

c. Isotopic composition of one sampling box is not discernable from another here. Heterogeneity is considered to be no longer detectable at this scale; considered "homogenous" at $T_{c\ Ga}$ where c < b < a

Determination of starting parameters

The upper limit of the $^{143}Nd/^{144}Nd$ value of the early depleted reservoir can be constrained to a first degree based on observations of $^{143}Nd/^{144}Nd$ values of early terrestrial reservoirs. The $^{143}Nd/^{144}Nd$ value in turn is linked with the $^{147}Sm/^{144}Nd$ values of the early depleted reservoir by the relationship (Jacobsen and Wasserburg, 1980a):

$$\frac{\varepsilon_{EDR}}{\varepsilon_{EER}} = \frac{f_{EDR}}{f_{EER}} = 1 - \frac{N_{BSE}(0)}{N_{EDR}(\tau)} = a$$

where

$$\varepsilon_i = \left[\frac{\left(^{143}Nd / {}^{144}Nd\right)_i}{\left(^{143}Nd / {}^{144}Nd\right)_{CHUR}} - 1 \right] \times 10{,}000$$

$$f_i = \left[\frac{\left(^{147}Sm / {}^{144}Nd\right)_i}{\left(^{147}Sm / {}^{144}Nd\right)_{CHUR}} - 1 \right]$$

where $^{147}Sm/^{144}Nd_{CHUR}$ is 0.1967(Jacobsen and Wasserburg, 1980b), N_{EDR} is the sum of a stable, nonradiogenic Nd species in the reservoir "EDR" at time τ, and a is a constant that determines the extent of depletion in the early depleted reservoir in relation to the Bulk Silicate Earth (BSE). N_{DM}/N_{BSE} for the modern day depleted mantle is typically is observed to be ~0.6.

The $\mu^{142}Nd$ value after the complete decay of ^{146}Sm ($\mu^{142}Nd$ is defined to be [($^{142}Nd/^{144}Nd - ^{142}Nd/^{144}Nd_{std}$)/$^{142}Nd/^{144}Nd_{std}$] x 1,000,000) is sensitive to the timing of differentiation and is dependent on the $^{147}Sm/^{144}Nd$ ratio of the early depleted reservoir through the relationship:

$$\left(\frac{^{142}Nd}{^{144}Nd}\right)_t^{EDM} = \left(\frac{^{142}Nd}{^{144}Nd}\right)_{t_p}^{BSE} + \frac{(^{146}Sm/^{144}Sm)_{t0}}{\left(^{147}Sm/^{144}Sm\right)_{t_p}}\left[\left(\frac{^{147}Sm}{^{144}Nd}\right)_{t_p}^{BSE} \times e^{-\lambda_{146}t_d} + \left(\frac{^{147}Sm}{^{144}Nd}\right)_{t_p}^{EDM} \times [e^{-\lambda_{146}t} - e^{-\lambda_{146}t_d}]\right]$$

Where t_p is the time at present, t_0 is the time at the beginning of solar system history, and t_d is time passed from the time of differentiation. $\lambda_{146} = 6.731^{-9}$ yr^{-1}. $^{146}Sm/^{144}Sm_{t0}$ is set to be 0.00828(Marks et al., 2014).

The extent to which the different layers are mixed are determined by the sizes of the reservoirs and their concentrations of Nd, and are constrained by relation (1). The relationship between the mass of a reservoir (M), the concentration of Nd (C) in a reservoir, and the abundance of Nd (N) in each of the reservoirs are

$$M_{EDR}C_{EDR} = N_{EDR},$$

Where the mass fraction of reservoir X_{EDR} is M_{EDR}/M_{BSE},

$$\text{and } X_{EDR} + X_{EER} = 1$$

Parameters that are capable of fitting extant $\mu^{142}Nd$ data were tested to be within a limited range. We use the following values organized in a table below:

N_{EDM}/N_{BSE}	ε_{EDM}	ε_{EEM}	f_{EDM}	f_{EEM}	$\mu^{142}Nd_{EDM}$	$\mu^{142}Nd_{EEM}$
50%	26.6	-26.6	0.1782	-0.1782	20	-20

Here the timing of differentiation is set to be 100 Ma after solar system formation. The relative sizes of the early depleted and enriched reservoirs are also linked to the concentration of Nd in the reservoirs, for which we consider:

l_{s3} (EDM)	l_{s2} (EEM)	M_{EDM}/M_{EEM}	C_{EDM}	C_{EEM}	Rate of mixing
2252	636	2.09	0.9232	1.935	500 Ma

where l_{s2} is the length scale of heterogeneity of reservoir "2," M_{EDM} is the mass of the early depleted mantle, and the average Nd concentration of the reservoirs are mass balanced so that the Bulk Silicate Earth concentration is 1.25 ppm(McDonough and Sun, 1995).

References

Jacobsen, S.B., Wasserburg, G.J., 1980a. A two-reservoir recycling model for mantle-crust evolution. Proc. Natl. Acad. Sci. 77, 6298–6302.

Jacobsen, S.B., Wasserburg, G.J., 1980b. Sm-Nd isotopic evolution of chondrites. Earth Planet. Sci. Lett. 50, 139–155. https://doi.org/10.1016/0012-821X(80)90125-9

Jacobsen, S.B., Yu, G., 2015. Extinct isotope heterogeneities in the mantles of Earth and Mars: implications for mantle stirring rates. Meteorit. Planet. Sci. 50, 555–567.

Kellogg, J.B., Jacobsen, S.B., O'Connell, R.J., 2007. Modeling lead isotopic heterogeneity in mid-ocean ridge basalts. Earth Planet. Sci. Lett. 262, 328–342. https://doi.org/10.1016/j.epsl.2007.06.018

Kellogg, J.B., Jacobsen, S.B., O'Connell, R.J., 2002. Modeling the distribution of isotopic ratios in geochemical reservoirs. Earth Planet. Sci. Lett. 204, 183–202.

Marks, N.E., Borg, L.E., Hutcheon, I.D., Jacobsen, B., Clayton, R.N., 2014. Samarium-neodymium chronology and rubidium-strontium systematics of an Allende calcium-aluminum-rich inclusion with implications for 146Sm half-life. Earth Planet. Sci. Lett. 405, 15–24. https://doi.org/10.1016/j.epsl.2014.08.017

McDonough, W., Sun, S. -s., 1995. The composition of the Earth. Chem. Geol. 120, 223–253. https://doi.org/10.1016/0009-2541(94)00140-4

CHAPTER 4

Mg isotopes of HIMU lavas from the Oslo Rift demonstrate formation from a normal peridotitic mantle source

This chapter has been submitted to *Proceedings of the National Academy of Sciences* close to its present form. The collaborators that were involved include (in the order of authorship) Fatemeh Sedaghatpour, Bjorn T. Larsen, Else-Ragnhild Neumann, and Stein B. Jacobsen.

Abstract

Alkalic to nepheline-normative basalts have highly fractionated trace element composition and the mantle source of many of these is the HIMU mantle. The origin of the HIMU source is subject to debate, but radiogenic isotopes have been used to favor recycled and dehydrated oceanic crust as the source. Experimental and element abundance constraints have been used to argue for a pyroxenite source, which could be formed from recycled oceanic crust, or from carbonated peridotite. Here we present Mg isotope measurements together with major and trace element analyses of highly fractionated, HIMU-like nepheline-normative melilitites from the Oslo Rift. We find that their Mg isotopic composition combined with their Gd/Yb ratio require a mantle source that is predominantly normal garnet peridotite. Lavas with HIMU signature can be derived from normal peridotite (without carbonate) sources as well as pyroxenite sources. The connection of HIMU compositions to a normal mantle peridotite source presents the first strong evidence against HIMU compositions as a tracer of recycled oceanic crust.

Mantle mixing through plate tectonics involves the recycling of oceanic crust that has been stretched and thinned throughout the mantle, and distributed below the lithosphere (Kellogg and Turcotte, 1990). Although the recycled oceanic crust is understood to contribute to the production of chemically heterogeneous mantle components, the process and extent of the contribution is not fully constrained. In addition, the subduction of oceanic crust is relevant to understanding the carbon cycle.

The formation of high time-integrated $^{238}U/^{204}Pb$ lavas (HIMU), has been thought to be a tracer for the residue of recycled oceanic crust after modification by arc volcanism (Zindler and Hart, 1986). Partial melting of altered oceanic crust has also been suggested to be one possible source for the production of nepheline-normative magmas (low SiO_2) and alkalic basalts (Kogiso et al., 2003), to account for their isotopic and major element compositions. Specifically, alkalic basalts, characterized by their high $Na_2O + K_2O$ contents in comparison to SiO_2, are observed in such settings but rare in terms of occurrence. Understanding the source and genesis of alkalic basalts is instrumental in elucidating the evolution of highly fractionated magmas such as nephelinites and carbonatites, and the mechanisms involved in the underlying mantle regarding their formation, as well as their role in rift formation and decompression melting. However, the petrogenesis of alkalic, SiO_2-undersaturated rocks, and in particular nepheline-normative basalts, is controversial and their source lithology is debated (Huang et al., 2015; Kogiso et al., 2003).

Alkalic compositions encompass basanites and nepheline-normative basalts, with melilitites being one extreme end-member in terms of SiO_2-undersaturation and occurrence (Barberi et al., 1982). Partial melting experiments have been used to argue that peridotites alone are insufficient in producing SiO_2-undersaturated alkalic lavas such as nephelinites,

melilitites, and kimberlitic compositions (Gerbode and Dasgupta, 2010; Kogiso et al., 2003). High CO_2 or carbonated peridotite have been shown to experimentally reproduce compositions similar to natural alkalic lavas (Dasgupta et al., 2007). Alternatively, pyroxenites and eclogites have been proposed to explain major element abundances of nepheline-normative magmas with HIMU signatures in ocean basalts (Hirschmann et al., 2003).

Magnesium (Mg) isotopes have been used to characterize the mantle source of basalts, as Mg is a major constituent of mantle minerals such as olivine, pyroxene, and garnet. Mg consists of three stable isotopes, ^{24}Mg, ^{25}Mg, and ^{26}Mg. The mass differences between the isotopes are significant enough to produce fractionation effects that are detectable at the ppm level. Significantly lower $\delta^{26}Mg$-values compared to the average peridotitic mantle (–0.25‰ ±0.07) (Teng et al., 2010, 2007) are attributed to carbonated lithologies in the mantle source. Carbonate minerals such as dolomite, calcite and aragonite exhibit negative $\delta^{26}Mg$-values, substantially lower than the peridotitic mantle ranging down to –5.57 (Teng, 2017). Low $\delta^{26}Mg$-values (down to –0.6) have been used to argue for source lithologies of alkalic rocks to be subducted oceanic slabs, carbonated eclogites, and also influences due to metasomatism by fluids in the mantle source (Dai et al., 2017).

The Skien area of the Oslo Rift has produced nepheline-normative lavas with unusual Nd, Sr and Pb isotopic compositions (Anthony et al., 1989; Corfu and Dahlgren, 2008; Jacobsen and Wasserburg, 1978) that correspond to HIMU signatures. Besides the isotopic composition, the Brunlanes melilitites have low SiO_2 content (35.5–40.0 %), moderate to high total alkalis of $Na_2O + K_2O$ (3.51–8.35%), low Al_2O_3 (7.6-10.9%), and high CaO (14.3–20.5%) content (**Appendix III Table S1**).

The Brunlanes samples (BR-01 to 05) collected and analyzed in this study cover 400 m of the 800 m stratigraphy (**Fig. 1**). Roughly 500 m of the upper stratigraphic column has been bracketed by samples that exhibit HIMU-like lead isotopic compositions (Corfu and Dahlgren, 2008). The δ^{26}Mg isotopic compositions of the Brunlanes samples on average are measured to be marginally lighter (average of –0.32‰; **Table 1**) than that of the average

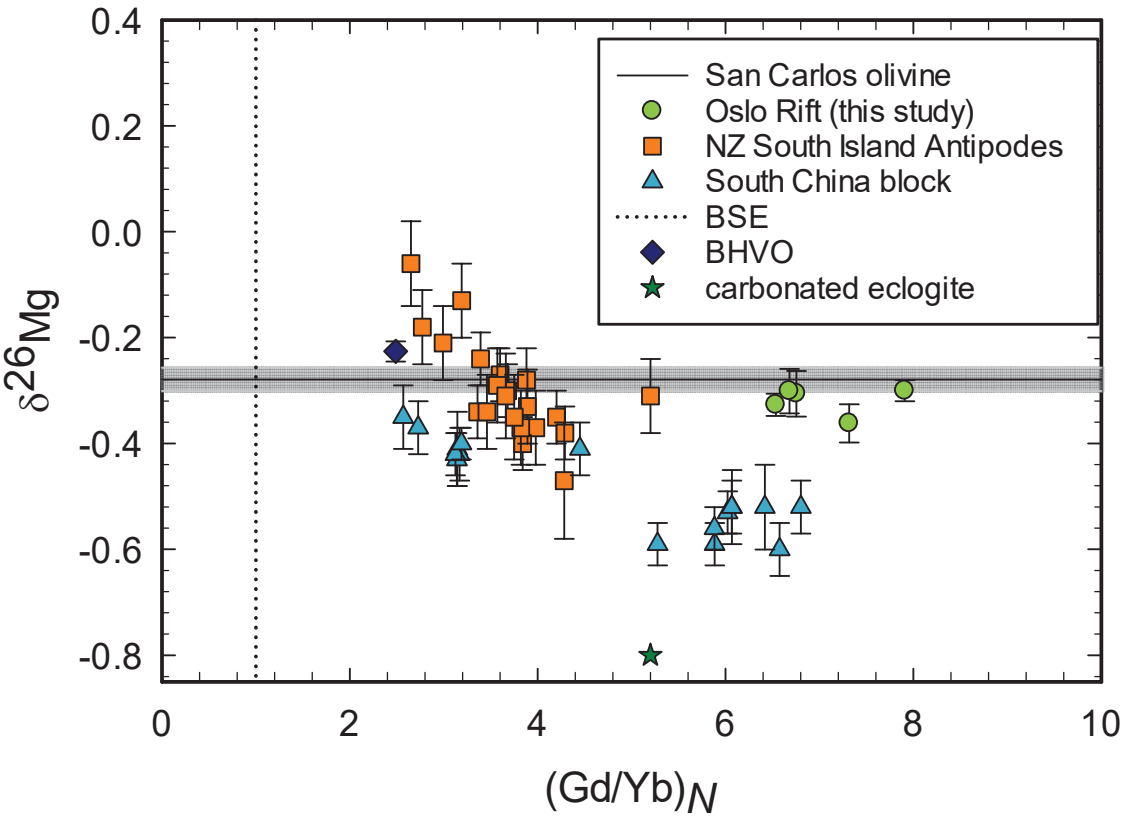

Fig. 1. Alkalic basalts from different regions plotted with respect to δ^{26}Mg vs Gd/Yb_N (bulk silicate Earth normalized ratios). The Brunlanes basalt melilitites from the Oslo Rift are indicated in green circles (this study), the alkalic New Zealand South Island Antipodes lavas are indicated in orange squares (Wang et al., 2016), and samples from the South China block are indicated in blue triangles (Huang et al., 2015). Errors bars are 2σ. BHVO (blue diamond), an ocean island basalt, is plotted (measurement from this study) for comparison with samples. Plotted to represent the average mantle δ^{26}Mg value of –0.25‰(Teng et al., 2010, 2007) is San Carlos Olivine (–0.28‰) from this study as well as the 2σ = ±0.023 error, indicated as a solid horizontal line and shading. The bulk silicate Earth Gd/Yb_N value (McDonough and Sun, 1995) is indicated as a dotted vertical line. The New Zealand South Island Antipodes intraplate alkalic samples exhibit a correlated trend between δ^{26}Mg and Gd/Yb_N, interpreted to be sourced from garnet and spinel peridotite lithologies and a carbonated eclogite source

(green star) that exhibits a high (>5) Gd/Yb_N and low $\delta^{26}Mg$ characteristic of carbonated lithologies (Wang et al., 2016). The alkalic rocks from the South China block have been interpreted to be affected by carbonatite metasomatism (Huang et al., 2015). The Brunlanes basalts from the Oslo Rift exhibit extremely high Gd/Yb_N ratios similar to kimberlites, with $\delta^{26}Mg$ values that are within the range of normal mantle peridotites, suggesting a garnet peridotite source that has undergone small degrees of partial melting.

peridotitic mantle. The small deviation of measured $\delta^{26}Mg$ signatures from the average peridotitic mantle in these Brunlanes samples are within the range of what is attributed to partial melting and magmatic differentiation (Teng et al., 2007). As Mg isotope fractionation from partial melting and fractional crystallization are minimal, signatures reflect source lithology, and the similarity in the $\delta^{26}Mg$ signatures of the samples to those of mantle peridotites strongly suggest that the samples are sourced from mantle peridotite. The high Gd/Yb_N ratios (6.5–7.3) and generally strong HREE depletion in these lavas can only be explained by residual garnet in the mantle source of these lavas (Wang et al., 2016). The Gd/Yb_N ratios among these melilitites are among the most extreme, similar in range to those found in Group I type, on-craton kimberlites (Becker and Le Roex, 2006), suggesting that the Brunlanes basalts were likely generated from very small degrees of partial melting, on the order of 1% (**Appendix III Fig. S3**). In addition to the Mg isotope signatures and strong REE fractionation patterns of the measured Brunlanes samples, the source lithology can be further assessed through factors such as FC3MS ($FeO/CaO - 3MgO/SiO_2$)(Yang and Zhou, 2013), and FeO/MnO ratios (Sobolev et al., 2005, 2007). Here, both the low FC3MS values (<0.65) and FeO/MnO ratios (<60), in addition to Mg isotope signatures, strongly suggest that the source is peridotitic rather than the type of pyroxenitic source inferred for some other HIMU basalts (**Fig. 3**). In contrast, a correlation between $\delta^{26}Mg$ isotopes and Gd/Yb_N ratios was reported for New Zealand HIMU lavas (Wang et al., 2016)

and is also apparent in HIMU basalts from the South China block (**Fig. 2**). These trends have been interpreted to reflect mixed sources of peridotite and carbonated eclogite for the New Zealand and South China localities. There is no evidence of such correlation in the Brunlanes samples; they are all consistent with a single homogenous garnet peridotite source.

HIMU-like intraplate lavas in New Zealand (Wang et al., 2016) are shown to be derived from recycled carbonated eclogites and spinel and garnet peridotites, implying a shallower source for

Table 1. Mg isotopic compositions of basaltic rocks and standards.

Sample	**Description**	**δ^{25}Mg**	**2σ**	**δ^{26}Mg**	**2σ**
BR-01	Nephelinite, Brunlanes	-0.188	0.018	-0.362	0.036
BR-02	Nephelinite, Brunlanes	-0.156	0.030	-0.306	0.043
BR-03	Nephelinite, Brunlanes	-0.152	0.016	-0.300	0.020
BR-04	Nephelinite, Brunlanes	-0.169	0.012	-0.327	0.021
BR-05	Nephelinite, Brunlanes	-0.143	0.017	-0.301	0.042
SC-Ol-H	San Carlos Olivine	-0.132	0.015	-0.279	0.022
	Bulk Silicate Earth (peridotite)	0.125	0.020	-0.250	0.040
	Average MORB and OIB	-0.125	0.030	-0.250	0.060
BHVO-2	Hawaiian basalt (USGS)	-0.120	0.007	-0.226	0.019
BCR-1	Columbia River basalt (USGS)	-0.104	0.019	-0.196	0.031

δ^{25}Mg-values are relative to the DSM3 standard. Errors are reported at the 95% level (2σ). SC-Ol-H is from a 50g powdered handpicked San Carlos olivines prepared at Harvard and distributed to other laboratories to rule out the effect of sample heterogeneity. Bulk Silicate Earth and average MORB and OIB(Teng, 2017; Teng et al., 2010). The δ^{25}Mg and δ^{26}Mg - values we obtained for the standards BHVO-2 and BCR-1 are the same as those summarized in other studies (Teng, 2017).

the basalts. Here the strong degrees of light δ^{26}Mg fractionation, and relatively high Gd/Yb_N ratios particularly eclogites. The suggested presence of a spinel peridotite source for the New Zealand alkalic rocks place partial melting at a shallower depth than those of the Brunlanes melilitites (Wang et al., 2016) (**Fig. 2**). Meanwhile, the garnet signature places the source of the Brunlanes melilitites in the garnet-stability field, at a depth of at least over 75 km, indicating a deep-seated source. In addition, thermobarometry (Lee et al., 2009) supports the notion of a deep-seated source for these melilitites at a derived depth of 120–140 km (**Appendix III**).

It has been argued that it is difficult to generate SiO_2-undersaturated basalts with the low Al_2O_3 (<10.9 wt%) and high CaO (14–20 wt %) compositions exhibited in theses samples from partial melting of dry peridotite alone (Hirschmann et al., 2003; Kogiso et al., 2003). Experiments have

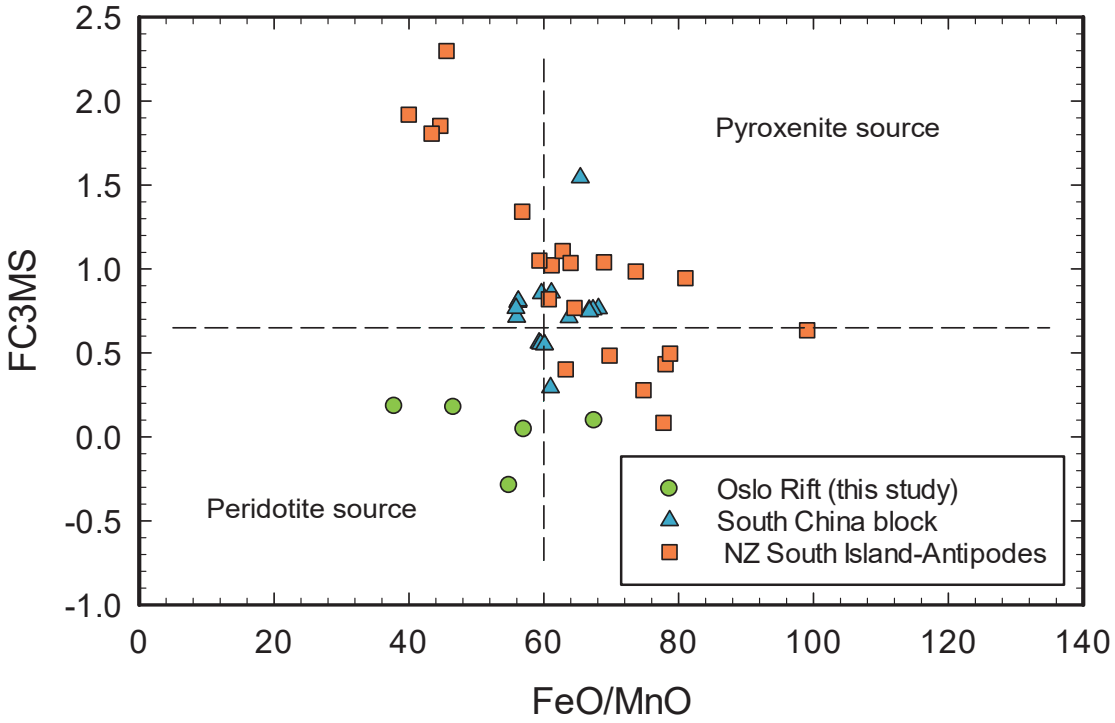

Fig. 2. FC3MS ($FeO/CaO - 3MgO/SiO_2$) and FeO/MnO values for the strongly SiO_2-undersaturated Brunlanes samples (green circles), compared to the alkalic but more weakly SiO_2-undersaturated South China block (blue triangles – Huang et al., 2015), and the New Zealand South Island Antipodes (orange squares(Wang et al., 2016)) for comparison. FC3MS < 0.65 and FeO/MnO < 60 have been taken to be indicative of a peridotite source lithology (3rd quadrant), while samples that plot in the 1st quadrant (FC3MS > 0.65 and FeO/MnO > 60) are thought to represent pyroxenite sources. The Brunlanes melilitites fall in the peridotite source field, supported by Mg isotope measurements. The samples from South China and New Zealand plot in the first quadrant, with some deviations, whose values reflect pyroxenite or mixed sources. Reported Fe_2O_3 values have been converted to FeO.

demonstrated that low degrees of partial melting of CO_2-enriched peridotites may generate melilitite compositions with CaO and Al_2O_3 abundances that are comparable with the samples analyzed in this study (Dasgupta et al., 2007). In contrast, the similar Mg isotope signatures of the Brunlanes samples to those of normal peridotitic mantle demonstrate the absence of recycled marine carbonate lithologies in their source. Although magmatic carbonatites could be another source of carbonate, $\delta^{26}Mg$ values of carbonatites have most often demonstrated extreme variability (–1.89 to –1.07‰ Song et al., 2016; 0.13 to 0.37‰ at Oldoinyo Lengai Li et al., 2016) unlike the peridotitic mantle, which is uniform with respect to $\delta^{26}Mg$.

Observations regarding mineral textures of calcite that indicate exsolution of CO_2 in nephelinitic lavas in the Oslo Rift (Anthony et al., 1989), support the likelihood of high CO_2 content in the erupted magmas. The lack of $\delta^{26}Mg$ variation and similarity to that of the normal peridotite mantle for the Brunlanes melilitites suggest that their source of CO_2 is from the ambient peridotite mantle rather than recycled carbonated lithologies or carbonatite metasomatism. The degree to which magmas can undergo enrichment in CO_2 from the peridotitic mantle through low degree of melting and fractionation, can be assessed through the C/Nb ratio of the bulk silicate Earth and the enrichment factor of Nb (172 to

465) in these samples, as CO_2 is as incompatible as Nb (Saal et al., 2002). An enrichment of 170 in C from a mantle background of 120 ppm (McDonough and Sun, 1995) suggests that the magmas could have 2 wt % C (corresponding to 16 wt % of $CaCO_3$). This indicates that melts that approach carbonatitic compositions, are capable of being produced from very small degrees of partial melting from the ambient mantle, and carbonate enrichment in a magma may happen during differentiation.

Oceanic crust that is recycled within the mantle is stretched and thinned due to mantle convection, ranging from kilometers to meters wide, down to a few centimeters (Kellogg and Turcotte, 1990). The dominant peridotite signature of these highly alkalic, Oslo Rift samples precludes pyroxenitic (recycled) components as the source of HIMU. One possible explanation for observing such a signature in peridotitic rocks is through mantle fertilization where subducted, noncarbonated oceanic crust or eclogites are well-mixed and homogenized into the peridotitic mantle (Yaxley and Green, 1998). Thus, the melilitites from the Oslo Rift suggest the presence of alternative internal processes in the mantle that are responsible for the production of HIMU signatures. In contrast to other studies of alkalic lavas (Dai et al., 2017; Wang et al., 2016; Yang and Zhou, 2013), the Mg isotopic measurements of the Brunlanes SiO_2-undersaturated alkalic magmas of the Oslo Rift establishes normal garnet peridotite as a source of alkalic magma genesis in this continental rift setting. In using Mg isotopes to understand the source lithologies and processes involved in the petrogenesis of mantle derived rocks, we conclude that there is not one singular source or method in generating alkalic magmas across the globe. Lavas with HIMU signature can be derived from normal peridotite (without carbonate) sources as well as pyroxenite sources. HIMU appears to be relatively common in the mantle, but the HIMU

end-member composition is relatively rare in volcanic rocks. The connection of HIMU compositions to a normal mantle peridotite source presents the first strong evidence against HIMU compositions as a tracer of recycled oceanic crust.

References

Anthony, E.Y., Segalstad, T. V, Neumann, E.-R., 1989. An unusual mantle source region for nephelinites from the Oslo Rift, Norway. Geochim. Cosmochim. Acta 53, 1067–1076.

Barberi, F., Satacroce, R., Varet, J., 1982. No Title, in: Continental and Oceanic Rifts. American Geophysical Union, pp. 223–258.

Becker, M., Le Roex, A.P., 2006. Geochemistry of South African on- and off-craton, group I and group II kimberlites: Petrogenesis and source region evolution. J. Petrol. 47, 673–703. https://doi.org/10.1093/petrology/egi089

Corfu, F., Dahlgren, S., 2008. Perovskite U-Pb ages and the Pb isotopic composition of alkaline volcanism initiating the Permo-Carboniferous Oslo Rift. Earth Planet. Sci. Lett. 265, 256–269. https://doi.org/10.1016/j.epsl.2007.10.019

Dai, L.-Q., Zhao, Z.-F., Zheng, Y.-F., An, Y.-J., Zheng, F., 2017. Geochemical Distinction between Carbonate and Silicate Metasomatism in Generating the Mantle Sources of Alkali Basalts. J. Petrol. 58, 863–884. https://doi.org/10.1093/petrology/egx038

Dasgupta, R., Hirschmann, M.M., Smith, N.D., 2007. Partial melting experiments of peridotite + CO_2 at 3 GPa and genesis of alkalic ocean island basalts. J. Petrol. 48, 2093–2124. https://doi.org/10.1093/petrology/egm053

Gerbode, C., Dasgupta, R., 2010. Carbonate-fluxed melting of MORB-like pyroxenite at 2·9 GPa and genesis of HIMU ocean Island basalts. J. Petrol. 51, 2067–2088. https://doi.org/10.1093/petrology/egq049

Hirschmann, M.M., Kogiso, T., Baker, M.B., Stolper, E.M., 2003. Alkalic magmas generated by partial melting of garnet pyroxenite. Geology 31, 481–484. https://doi.org/10.1130/0091-7613(2003)031<0481:AMGBPM>2.0.CO;2

Huang, J., Li, S.G., Xiao, Y., Ke, S., Li, W.Y., Tian, Y., 2015. Origin of low δ^{26}Mg Cenozoic basalts from South China Block and their geodynamic implications. Geochim. Cosmochim. Acta 164, 298–317. https://doi.org/10.1016/j.gca.2015.04.054

Jacobsen, S.B., Wasserburg, G.J., 1978. Nd and Sr isotopic study of the Permian Oslo Rift.

Open-File Rep. - U. S. Geol. Surv. Rep. 78-0701 194–196.

Kellogg, L.H., Turcotte, D.L., 1990. Mixing and the distribution of heterogeneities in a chaotically convecting mantle. J. Geophys. Res. 95, 421–432. https://doi.org/10.1029/JB095iB01p00421

Kogiso, T., Hirschmann, M.M., Frost, D.J., 2003. High-pressure partial melting of garnet pyroxenite: Possible mafic lithologies in the source of ocean island basalts. Earth Planet. Sci. Lett. 216, 603–617. https://doi.org/10.1016/S0012-821X(03)00538-7

Lee, C.T.A., Luffi, P., Plank, T., Dalton, H., Leeman, W.P., 2009. Constraints on the depths and temperatures of basaltic magma generation on Earth and other terrestrial planets using new thermobarometers for mafic magmas. Earth Planet. Sci. Lett. 279, 20–33. https://doi.org/10.1016/j.epsl.2008.12.020

Li, W.Y., Teng, F.Z., Halama, R., Keller, J., Klaudius, J., 2016. Magnesium isotope fractionation during carbonatite magmatism at Oldoinyo Lengai, Tanzania. Earth Planet. Sci. Lett. 444, 26–33. https://doi.org/10.1016/j.epsl.2016.03.034

McDonough, W., Sun, S. -s., 1995. The composition of the Earth. Chem. Geol. 120, 223–253. https://doi.org/10.1016/0009-2541(94)00140-4

Saal, A.E., Hauri, E.H., Langmuir, C.H., Perfit, M.R., 2002. Vapour undersaturation in primitive mid-ocean ridge basalt and the volatile content of the Earth's upper mantle. Nature 419, 451–455.

Sobolev, S., Hofmann, A.W., Nikogoslan, I.K., 2005. An olivine--free mantle source of Hawaiian sheild basalts. Nature 434, 590–597.

Sobolev, A. V, Hofmann, A.W., Kuzmin, D. V, Yaxley, G.M., Arndt, N.T., Chung, S.-L., Danyushevsky, L. V, Elliott, T., Frey, F.A., Garcia, M.O., Gurenko, A.A., Kamenetsky, V.S., Kerr, A.C., Krivolutskaya, N.A., Matvienkov, V. V, Nikogosian, I.K., Rocholl, A., 2007. The Amount of Recycled Crust in Sources of Mantle - Derived Melts. Science 316, 412–417. https://doi.org/10.1126/science.1138113

Song, W., Xu, C., Smith, M.P., Kynicky, J., Huang, K., Wei, C., Zhou, L., Shu, Q., 2016. Origin of unusual HREE-Mo-rich carbonatites in the Qinling orogen, China. Sci. Rep. 6, 1–10. https://doi.org/10.1038/srep37377

Teng, F.-Z., 2017. Magnesium Isotope Geochemistry. Rev. Mineral. Geochemistry 82, 219–287. https://doi.org/10.2138/rmg.2017.82.7

Teng, F.Z., Li, W.Y., Ke, S., Marty, B., Dauphas, N., Huang, S., Wu, F.Y., Pourmand, A., 2010. Magnesium isotopic composition of the Earth and chondrites. Geochim. Cosmochim. Acta 74, 4150–4166. https://doi.org/10.1016/j.gca.2010.04.019

Teng, F.Z., Wadhwa, M., Helz, R.T., 2007. Investigation of magnesium isotope fractionation during basalt differentiation: Implications for a chondritic composition of

the terrestrial mantle. Earth Planet. Sci. Lett. 261, 84–92. https://doi.org/10.1016/j.epsl.2007.06.004

Wang, S.J., Teng, F.Z., Scott, J.M., 2016. Tracing the origin of continental HIMU-like intraplate volcanism using magnesium isotope systematics. Geochim. Cosmochim. Acta 185, 78–87. https://doi.org/10.1016/j.gca.2016.10.009

Yang, Z.F., Zhou, J.H., 2013. Can we identify source lithology of basalt? Sci. Rep. 3, 1–7. https://doi.org/10.1038/srep01856

Yaxley, G.M., Green, D.H., 1998. Reactions between eclogite and peridotite: Mantle refertilisation by subduction of oceanic crust. Schweizerische Mineral. Und Petrogr. Mitteilungen 78, 243–255.

Zindler, A., Hart, S.R., 1986. Chemical Geodynamics. Annu. Rev. Earth Planet. Sci. 14, 493–571. https://doi.org/10.1146/annurev.earth.14.1.493

CHAPTER 5

Exploring models of early Earth differentiation and late veneer delivery and subsequent mantle mixing through $^{182}W/^{184}W$ isotopes

Abstract

The hypothesized late veneer (or "late accretion) is thought to have replenished the highly siderophile element (HSE) abundances of the terrestrial mantle post-core formation, while suggested to have been involved in the delivery of the volatiles of the Earth. As W is moderately siderophile, the delivery of the late veneer is also expected to have affected the W isotopic composition of the mantle. Using a stochastic mixing model, we explore the time scale at which the late veneer is homogenized into mantle, in the form of an undifferentiated thin layer resembling a CI chondrite composition. Assuming a mixing rate of 500 Myr as proposed by studies that employ similar mixing models, we find that the time scale to mix and lower the W isotope composition of the bulk mantle by the late veneer is up to ~2.5 Gyr. The W concentrations and W isotope compositions of the reservoirs have no effect on the time scale of homogenization. Thus a positive ($\varepsilon^{182}W > 0$) mantle W isotope signature due to mantle-core differentiation but prior to late veneer delivery, is expected to persist and be sampled well into the late Archean. An alternative scenario where the late veneer is initially mixed with only the solid upper mantle prior to whole mantle convection is explored. We find that due to the smaller size of the reservoir involved in mixing, the timescale at which the late veneer is homogenized into the upper mantle is shortened by 20% (0.5 Gyr). If the homogenization of the late veneer happened within the first 1 Ga of Earth's history, it must have occurred with a shorter mixing rate implying fast convection, within a smaller

mantle volume, or in the presence of a fast-convecting magma ocean. Understanding a full picture of the extent and time scale of mixing late veneer in the Earth's mantle requires resolution with $^{187}Os/^{188}Os$ isotopes.

Introduction

^{182}Hf decays to ^{182}W with a half-life of 8.9 million years. Owing to its short half-life and the lithophile(earth-loving)-siderophile (iron-loving) nature of the parent-daughter isotopes, the system is a tracer for early Earth differentiation processes. As the system is specifically applicable to metal-silicate differentiation effects, the system has been used as a tracer for the timing of core formation.

The notion of a late veneer (also referred to as "late accretion"), referring to accretionary material that is thought to have been added to the terrestrial mantle post-core formation, was introduced to accommodate the observation of elevated highly siderophile element (HSE) abundances in modern day terrestrial rocks. Late veneer (also referred to as "late accretion") indicates delivery of material to the Earth after the formation of the core. HSEs refer to elements such as Re, Os, Pt, Ir, Ru, and Pd. Owing to their strong affinity to metal, the bulk of the HSEs are expected to have largely been sequestered into the core during the differentiation of the metallic core and silicate mantle at core-mantle boundary conditions, leaving the mantle stripped of HSEs. It is commonly thought that the delivery of late veneer would have comprised 0.2–0.9% of the Earth's mass (Chou, 1978; Willbold et al., 2011), being well-mixed into the mantle.

The delivery of the late veneer would have not only affected HSE abundances, but moderately siderophile elements and their isotopic compositions of the mantle. Among

them, tungsten is of interest. Tungsten (W) isotope signatures of the ubiquitous mantle at modern-day have been observed to be offset compared to carbonaceous and ordinary chondrites by up to close to 2ε units (Kleine et al., 2002; Yin et al., 2002), where ε = ($^{182}W/^{184}W - {}^{182}W/^{184}W)/{}^{182}W/^{184}W$ x 10,000. Many portions of the W isotope composition of the Archean mantle is elevated by 0.15 ε units. As tungsten is a moderately siderophile element, the delivery of late veneer would have inevitably affected tungsten isotope signatures on top of HSEs, cumulatively lowering the $\varepsilon^{182}W$ isotope signatures of the mantle. However, the $\varepsilon^{182}W$ isotopic signature of the mantle in relation to the time scale of the homogenization of the late veneer is not well understood.

The short-lived ^{182}Hf-^{182}W isotope system is relevant to understanding the mixing of the late veneer. Another short-lived isotope system that is relevant to the time scale of mantle mixing, is the ^{146}Sm-^{142}Nd system, specifically considered a tracer for early silicate differentiation effects, owing to its lithophile nature and short half-life of 68 (Kinoshita et al., 2012) or 103 (Friedman A M, 1966) Myr. Anomalies in $^{142}Nd/^{144}Nd$ ratios ($\mu^{142}Nd \neq 0$) with respect to a terrestrial reference point (the modern-day mantle) reflect the presence of a differentiation event before the system was long-extinct, whose occurrence would have been within the first 500 Myr of solar system formation. Any anomalies detected after this time frame would be reflective of the extent of mixing of the silicate reservoirs. The ^{182}Hf-^{182}W and ^{146}Sm-^{142}Nd systems combined act as a tracer of mantle mixing.

The late veneer is not only thought to have been responsible for the HSE abundances of the mantle, but also involved in the delivery of volatiles such as water (Drake and Righter, 2002). Such a consideration is relevant to the study of the origins of life, as the delivery of volatiles pertain to the formation of the oceans and the evolution of the

Earth's atmosphere. Isotopic tracers have been instrumental in identifying different chondrites as candidate materials for the late veneer. In particular, carbonaceous chondrites, over comets, have been considered as the likely candidate material responsible for the delivery of water based on the similarity of their D/H ratios to the ocean. Among chondrites, CI chondrites are the most primitive and the most abundant in volatile content, being comprised of up to 10 wt% in water content.

Simple two-component diagrams have often been invoked to explore differentiation scenarios of the early Earth, and their subsequent homogenization throughout time. Considering CI chondrites as candidates for late veneer material, here we apply a simplified stochastic mixing model in order to understand the extent and timing through which a late veneer is well-mixed into the mantle. We aim to explore early Earth differentiation and accretionary scenarios with the aid of the rock record throughout time.

Methods

Observations from the Data

Based on the distribution of $\varepsilon^{182}W$ isotopes as a function of time, it may be possible to deduce a number of reservoirs sorted by the dominant $\varepsilon^{182}W$ signature based on the W isotope rock record. There is generally an elevated $\varepsilon^{182}W$ signature persisting throughout the Archean and post-Archean (**Fig. 7**), with a dominant distribution around 15 ppm (**Fig. 8**) (where ppm is units of "parts per million" and ppm= ε x 0.01). This elevation is in comparison to the modern-day, well-mixed mantle persisting throughout the Archean and post-Archean. There are reservoirs whose dominant $\varepsilon^{182}W$ signature clusters around 11 ppm (Liu et al., 2016); however, it may be questioned as to whether these clusters are

distinctly resolved from 15 ppm due to the typical resolution of the measurements ($2\sigma = \pm 0.04–0.06\varepsilon$). Schapenberg komatiites of 3.55 Ga age have demonstrated the presence of a reservoir with a negative $\varepsilon^{182}W$ anomaly, averaging at –0.08 (Puchtel et al., 2016). The dominant modern-day terrestrial mantle is considered to have an $\varepsilon^{182}W = 0$. $\varepsilon^{182}W$ isotopes demonstrate a distribution of data scattered in between up to 0.21 and -8, indicating a broader range of $\varepsilon^{182}W$ isotope signatures that is sampled throughout time. The data points closer to $\varepsilon^{182}W=0.21$ have large error bars.

The $\varepsilon^{182}W$ isotope signature of the modern day mantle is considered to fall on the terrestrial standard at $\varepsilon^{182}W = 0$ (Yin et al., 2002). However, the largest $\varepsilon^{182}W$ anomalies have been discovered among modern day samples, with flood basalts demonstrating an $\varepsilon^{182}W$ anomaly that is up to 0.50 units high, and ocean island basalts as low as -0.18 ppm. These reservoirs may be considered separate from the reservoirs inferred from distribution of $\varepsilon^{182}W$ isotopes scattered as a function of time as discussed above.

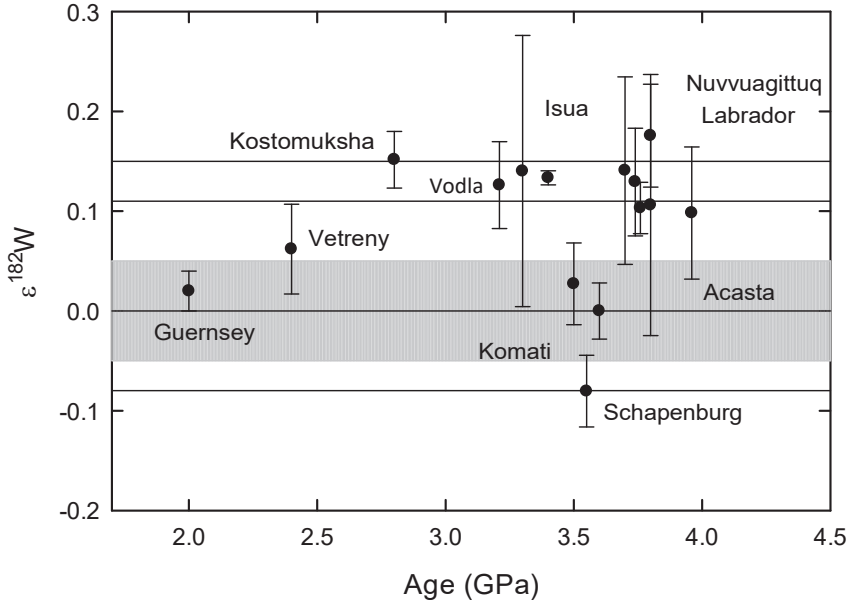

Fig. 1. Averages of different sample $\varepsilon^{182}W$ signatures per locale or age, plotted with respect to time. Data are from (Liu et al., 2016; Mundl et al., 2017; Rizo et al., 2016b, 2016a, Touboul et al., 2014, 2013, 2012, Willbold et al., 2015, 2011). An elevated $\varepsilon^{182}W$ signature of 0.15 is apparent throughout the early history of the Earth, which is no longer observed after 2.7 Ga. The data imply the presence of a reservoir at $\varepsilon^{182}W = 0.10$ in addition to one at 0.15. One reservoir is observed to have a negative $\varepsilon^{182}W$ anomaly of -0.08 (Puchtel et al., 2016). The 2σ external reproducibility error bars (±0.05) are shaded around $\varepsilon^{182}W = 0$. For reference, horizontal lines are plotted to represent $\varepsilon^{182}W$ isotope values at 0.15, 0.11, 0 and -0.08.

Model Set-Up

It has been proposed that the chondritic late veneer $\varepsilon^{182}W$ composition corresponding to 0.5% of the bulk silicate Earth is capable of bringing down the bulk mantle $\varepsilon^{182}W$ value by 0.15 (Morgan et al., 2001; Willbold et al., 2011). Most of the $\varepsilon^{182}W$ isotopic composition of the early rock record is demonstrated to be around 0.15 (**Fig. 1**). As the bulk $\varepsilon^{182}W$ value of the terrestrial mantle after core formation is not known, as a starting point, we set the terrestrial mantle that has largely differentiated into a reservoir with an elevated $\varepsilon^{182}W$ signature of 0.15 ppm, and a W concentration of around 13±10 ppb (Arevalo and McDonough, 2008).

The late veneer is initially assumed to take up a top layer corresponding to a depth of 12.5 km of the terrestrial mantle, composed of a uniform composition corresponding to the $\varepsilon^{182}W$ isotopic composition and W concentrations undifferentiated CI chondrites. A layer of such a depth would correlate to 0.7% of the volume of the silicate Earth, which is within the range of late veneer mass estimates (0.2 to 0.9%). The delivery of late veneer through large planetesimals is another alternative scenario that is capable of embedding these bodies deeply into the silicate mantle upon impact, inducing faster homogenization of the mantle. However, the size and masses of the bodies, as well as the energy these from early heat sources such as radioactive elements would likely have caused these bodies to differentiate into a silicate mantle and core. These scenarios have

been explored in related studies (Marchi et al., 2018). In such a scenario, exploration of the composition of late veneer as undifferentiated CI chondrites is not possible.

CI chondrites are primitive meteorites that are the most enriched in volatiles among the different classes of chondrites (which include ordinary and enstatite chondrites). The D/H ratio of the oceans are measured to be most similar to those of carbonaceous chondrites rather than of comets. Thus, we employ CI chondrites as the most likely candidate material to constitute the late veneer.

Based on the data, we test the following scenarios

(A) The late veneer is set to mix into the whole mantle 2890 km in depth. The uppermost layer of the mantle is set to be the late veneer, which is comprised of a chondritic $\varepsilon^{182}W$ value of –1.9 (Yin et al., 2002), and a W concentration ranging from 90–117 ppb (Jochum, 1996; Kleine et al., 2004). The W concentration of Orgueil (CI chondrite) is measured to be 90.3 ppb in one study (Jochum, 1996), while in another (Kleine et al., 2004), the measurements range from 109.2 to 116.8 ppb. We apply a stirring rate of 500 Myr, derived from similar whole mantle mixing models (Kellogg et al., 2007, 2002) to explore the duration at which the late veneer can be well-mixed into the whole mantle.

(B) We explore a scenario in which the late veneer may initially mix with a fraction of the mantle (e.g., the upper mantle only, a depth of 660 km). Such a scenario may be applicable in a partial magma ocean scenario, where the late veneer is efficiently mixed into the mantle in an environment that is convecting relatively rapidly, and where the lower mantle is subsequently mixed with the upper mantle that has solidified. We test a scenario in which the late veneer is assumed to mix

into a volume that corresponds to a solid upper mantle. A whole magma ocean scenario, which would be in contact with the core, may effectively deliver the late veneer into the core. Thus in considering the extent of mixing of the late veneer in the silicate mantle, it is useful to assume a barrier between the liquid magma ocean mantle and the core. The resulting upper mantle $\varepsilon^{182}W$ value after complete homogenization with the late veneer results in an initial overall negative $\varepsilon^{182}W$ composition, whose mass balance constraints are calculated such that the involvement of the lower mantle with the upper mantle volume will subsequently produce a W isotopic composition of $\varepsilon^{182}W = 0$. The W concentrations and $\varepsilon^{182}W$ isotopic composition of the late veneer is as scenario (A).

The model assumes that all domains of the reservoirs involved are equally mixed and randomly sampled. Recent studies of W (Mundl et al., 2017; Rizo et al., 2016b) and Nd (Hyung and Jacobsen, *under review*.; Horan et al., 2018; Peters et al., 2018) isotope anomalies have shown that there are portions of the mantle preserving extreme isotope effects, implying that this is not entirely the case. However, the bulk of the sampled modern day mantle, which is homogeneous in $^{142}Nd/^{144}Nd$ isotopes to within 5-6 ppm precision, may still be considered a reflection of the extent to which the majority of the mantle is well-mixed.

Mantle Stirring Function

The mantle is set to consist of two reservoirs corresponding to two layers, which are gradually homogenized and mixed as a function of time. Here in this scenario, the upper reservoir is set to pertain to the thickness of the late veneer layer, while the length scale

of the lower reservoir pertains to the depth of the remainder of the bulk mantle for scenario (A). In scenario (B), the upper layer is set to be the thickness of the late veneer, and the lower layer is set to be the depth of the upper mantle volume, leaving the lower mantle untouched.

The mantle reservoirs are gradually deformed with convective mixing, where the short length scale of heterogeneity (thickness of the reservoirs) is assumed to exponentially decrease as a function of time:

$$l_t = l_0 e^{-\frac{t}{\tau_{stir}}}$$

Where l is the length scale of heterogeneity, t is time, and τ_{stir} = mixing rate. As discussed in Kellogg et al., (2002), such a relationship is derived from simulations of 3D mantle convection models. The set-up for the mixing of multiple reservoirs has been used in (Kellogg et al., 2007, 2002); however, this particular case is simplified to fit short-lived isotope systems following (Jacobsen and Yu, 2015).

Sampling Function

A random sampling box of size l_s^3 is set to simulate a melting event that samples the mantle mixture consisting of two reservoirs that are isotopically distinct. l_s is set to be 100 km, after the size of a typical melting column. As the short-length scale of heterogeneity are most critical to the problem, each reservoir can be assumed to consist of cubes that are randomly distributed throughout the mantle. The isotopic composition of the sampling box is calculated by considering the isotopic compositions of the reservoirs and the sizes and number of randomly distributed cubes. A sampling rate of 1000 per time step of 100 Myr is employed in order to sufficiently explore the distribution of $\varepsilon^{182}W$ values that likely to be sampled throughout time. We use the algorithm outlined in

Jacobsen and Yu (2015) in calculating the numbers and sizes of the reservoirs per time step for a random sampling scheme.

Mass balance equations

The isotopic composition of the sample is calculated by considering the volumetric proportions, the isotopic compositions, and concentrations involved in the reservoirs through the following relationship:

$$\varepsilon_{W(CHUR),sample} = \varepsilon_{W(CHUR),2}\ x_2\ \frac{C_{W,2}}{W,sample} + \varepsilon_{\mathrm{W(CHUR),3}}(1 - x_2)\frac{C_{W,3}}{C_{W,sample}}$$

where $C_{W,2}$ and $C_{W,3}$ are the W concentrations, and $\varepsilon_{W(CHUR)2}$ and $\varepsilon_{W(CHUR)3}$ are the initial W isotopic compositions of the late veneer and the mantle, respectively, and x_2 corresponds to the mass proportion of the late veneer. $C_{W,sample}$ is defined as the W concentration of the mantle source of the sample, calculated through:

$$C_{W,sample} = C_{W,2}x_2 + C_{W,3}(1 - x_2)$$

We explore values that range from 90.6 and 116.8 ppb for the W concentration of the late veneer. A late veneer of a thickness of 12.5 km from the surface of the Earth corresponds to a volumetric proportion of 0.7% of the mantle. We assume that volume corresponds to mass requires that the density of the mantle be constant with depth. However in such a case, even up to a 25% increase in the late veneer thickness may be considered to be fractional in comparison to the thickness of the whole mantle.

The W concentration for the bulk the mantle is set to be within the range of 12.3–12.5 ppb so the resulting bulk silicate Earth W concentration is around 13 ppb. Assuming constant density throughout the mantle, late veneer that corresponds to 0.2% of the volumetric proportion of the mantle corresponds to a layer that is 3.6 km thick, and while a 16 km thick layer would correspond to 0.9% of the bulk mantle.

Results

Due to mass balance constraints, the range of constraints in which it is possible to solely use CI chondrites as late veneer to completely mix the elevated 0.15 ε^{182}W signature to a bulk silicate Earth value of zero is limited. When considering a W concentration of 90.3 ppb and a ε^{182}W value of –1.9, a late veneer volume constituting 0.9% (the upper limit of the estimate mass of the late veneer, corresponding to a 16 km depth) of the mantle produces a bulk silicate Earth value of 0.024 ε^{182}W from 0.15, indicating a necessity for a more negative ε^{182}W value, a high W concentration, or a higher proportion of late veneer material in comparison to the mantle. When considering the maximum W concentration of the late veneer based on such measurements for Orgueil at 117 ppm, a mass corresponding to 0.8% of the bulk mantle may be considered for the late veneer. When considering the previous estimate of the bulk silicate Earth W concentration of 29 ppb (McDonough and Sun, 1995), mixing the bulk mantle using the same set of parameters results in an elevated bulk silicate Earth ε^{182}W value of 0.077, offset from 0. This type of ε^{182}W elevation would be detectable as in comparison, the long term external reproducibility of ε^{182}W is typically at 2σ = 0.04–0.06 ε (Mundl et al., 2017; Puchtel et al., 2016).

We explore scenario (A) through **Figs. 2-5**, in which a late veneer addition is assumed to be gradually mixed into the entire mantle. **Figs. 4-6**. are focused on exploring scenario (B), in which the late veneer is only initially mixed into the upper volumetric portion of the mantle. **Figs. 2** to **4** lay out the results for the time scales involved in mixing a late veneer mass of 0.7% in comparison to the volume of the bulk silicate Earth. **Fig 2.** lays out the distribution of ε^{182}W isotopes evolving as a function of

time. Following the model of Willbold et al., (2011), the bulk mantle after core-formation here is assumed to represent a reservoir whose dominant $\varepsilon^{182}W$ is 0.15. Invoking a stirring rate of 500 Myr, it is demonstrated that the elevated $\varepsilon^{182}W$ signature would persist throughout the mantle as the dominant signature for a prolonged period of time. Negative $\varepsilon^{182}W$ signatures that result from the mixture of the late veneer and the dominant positive $\varepsilon^{182}W$ mantle composition would have a high likelihood of being sampled close to its full homogenization as recent as 2 Ga (**Fig. 2**). The sampling distribution in the very early history of the Earth is demonstrated to largely biased toward high $\varepsilon^{182}W$ signatures (**Fig. 3**), with a small probability of sampling the late veneer itself being present. Assuming the mixing of a largely solid mantle in the early history of the Earth, invoking a shorter mixing rate of 100 Myr is demonstrated to have the potential to significantly shorten the time scale at which the late veneer may be thoroughly mixed into the mantle after delivery (**Fig. 4**).

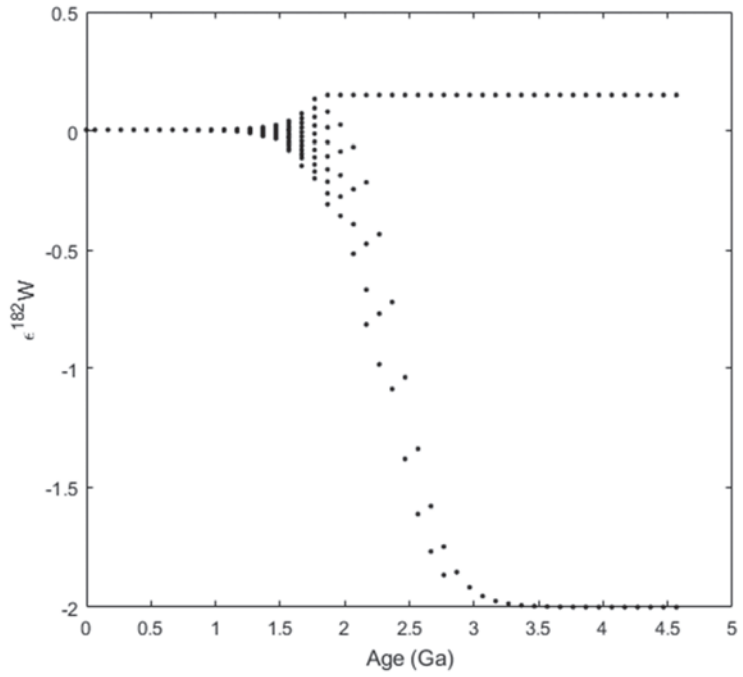

Fig. 2. Distribution of $\varepsilon^{182}W$ isotopes throughout time, assuming a model of two layers, where the upper shallow layer is the late veneer, and the lower reservoir corresponds to the mantle after core-mantle differentiation. The layers are assumed to be of uniform concentrations of W, and $\varepsilon^{182}W$ compositions. A uniform stirring rate of τ = 500 Myr is assumed throughout time. The model demonstrates that such an elevation of $\varepsilon^{182}W$ isotope signatures can persist for close to 3 Gyr after delivery of late veneer. The timing of delivery here in this model is assumed to be 4.57 Ga, but in the context of investigating the persistence of Archean and post-Archean $\varepsilon^{182}W$ signatures through the mixing of late veneer, shifting the initial timing of delivery of the late veneer by up to 200 Myr is shown to be insignificant in comparison.

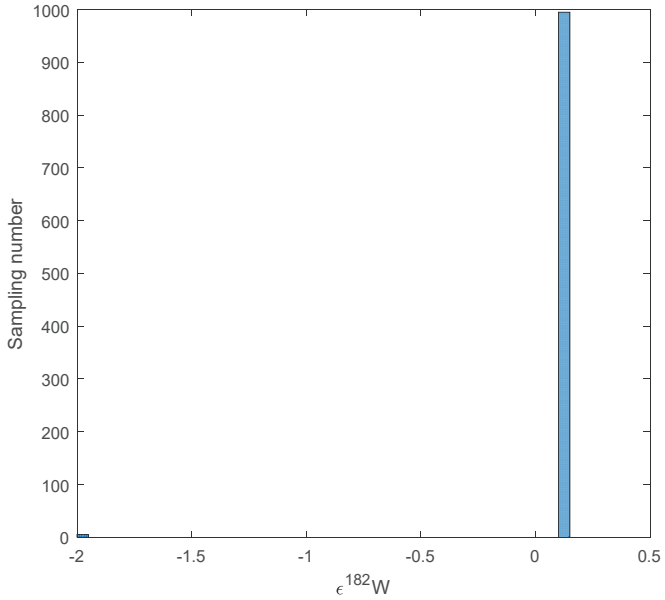

Fig. 3. Histogram demonstrating the probability of sampling a reservoir characteristic of the corresponding ε^{182}W value at 4.37 Ga for sampling occurrences of 1000. In such a scenario, the rock record will mostly reflect the elevated signatures of the mantle after core-formation. It is shown that there is a small probability of "sampling" the late veneer that has not be homogenized into the mantle at this time step (lower left-hand corner of the figure).

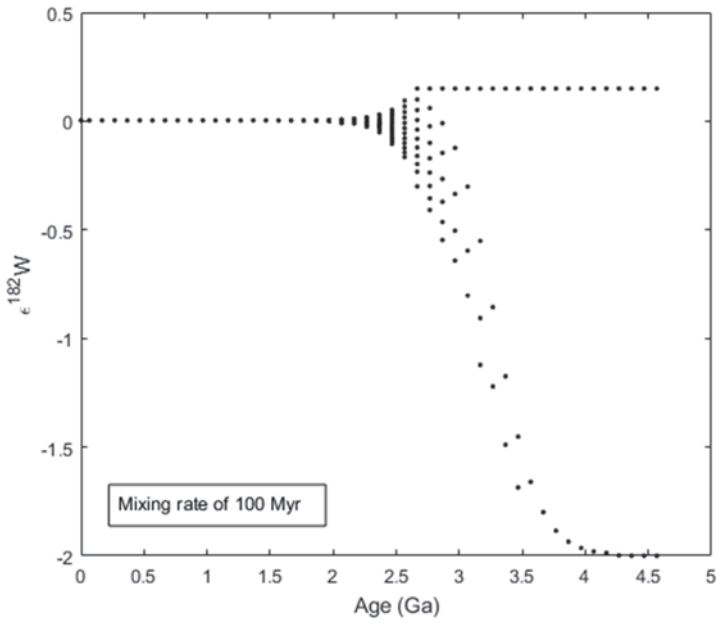

Fig. 4. Invoking a higher mixing rate of 100 Myr, as opposed to 500 Myr, starting from solar system history will mix in the elevated 0.15 signature within the first 1.5 Gyr.

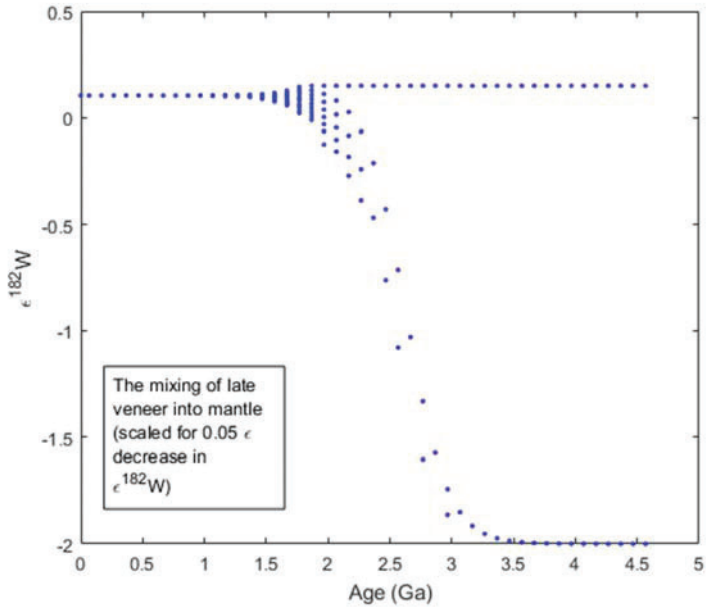

Fig. 5. A model where the bulk $\varepsilon^{182}W$ composition of the mantle decreases by 0.05 $\varepsilon^{182}W$ units as opposed to 0.15. Through comparison with **Fig. 1.,** it may be deduced that that the dominating factor that dictates the evolution of the distribution of $\varepsilon^{182}W$ signatures as a function of time and their convergence, depends heavily on the relative sizes of the reservoirs involved, but not by variables such as the starting $\varepsilon^{182}W$ compositions of the late veneer and the bulk mantle.

In **Fig. 5.,** we show the results of a tested scenario in which the mixing of a late veneer, whose mass balance requirements hypothetically only lowers the bulk silicate Earth $\varepsilon^{182}W$ isotope signature by 0.05. The time scale in which the two reservoirs are fully equilibrated and homogenized are similar to that of the scenario of **Fig. 2**, despite different parameters for the late veneer content.

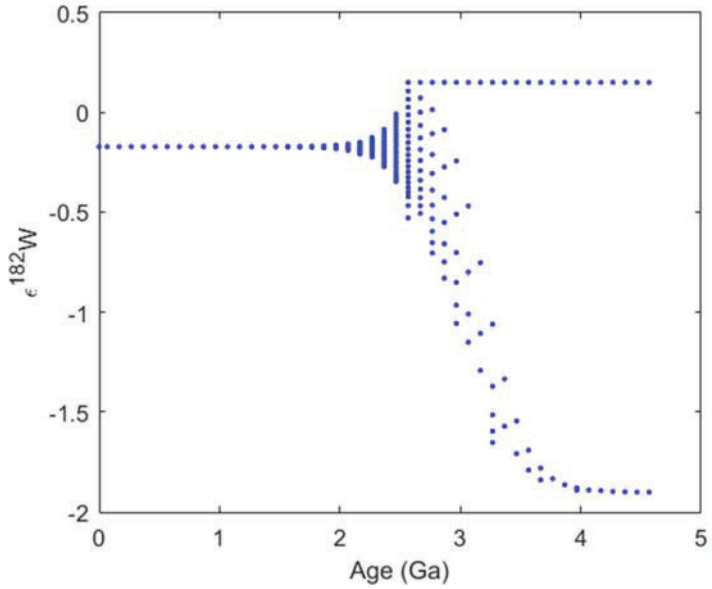

Fig. 6. Scenario in which the late veneer (at a volumetric proportion of 0.7% compared to the bulk silicate Earth) is initially being mixed into a volume that corresponds to the volume of the solid upper mantle at a mixing rate of 500 Myr. The time at which it takes for the homogenization of late veneer into just the upper mantle is less than what it takes for the homogenization into a full mantle. It may be deduced that the volumes of the reservoirs, as well as the absolute sizes of the reservoirs have a role in affecting the time scale at which the late veneer fully is mixed into the mantle. The resulting negative $\varepsilon^{182}W$ value of the mantle may be assumed to be fully mixed into $\varepsilon^{182}W = 0$ with the full mixing of the rest of the lower mantle.

In **Fig. 6,** we show that the distribution of $\varepsilon^{182}W$ as a function of time as the late veneer is being mixed into a reservoir whose size and depth resembles the solid upper mantle volume. The involvement of mixing the late veneer into a smaller volume in comparison to the whole mantle homogenizes the late veneer relatively quickly in comparison to scenario (A) (**Fig. 2.**), shortening the time scale by 0.5 Gyr.

Discussion

We discuss the extent of the different reservoirs, and their relation to the aforementioned models outlined in the Methods section. Model (A) is most capable of

explaining the elevated distribution of $\varepsilon^{182}W$ isotope anomalies that are observed throughout time at a positive value of 0.15, to converge to 0 at modern day. With a consistent 500 Myr mixing rate for the whole mantle, it is possible to explain the presence of $\varepsilon^{182}W$ positive anomalies of $\varepsilon^{182}W = 0.15$ persisting up until 2.7 Ga (Touboul et al., 2012), as the late veneer is not easily mixed into the mantle after its delivery.

The model however, is not capable of producing a potential second positive $\varepsilon^{182}W$ reservoir at a value of 0.11 persisting throughout time, nor a reservoir with a negative $\varepsilon^{182}W$ anomaly of -0.08 without assuming their presence *a priori*. The negative $\varepsilon^{182}W$ reservoir, at a value of –0.08 and dated to be 3.550 Ga old, is attributed to a silicate differentiation event which is likely to have occurred before ^{182}Hf was extinct, within the first 60 Myrs (Puchtel et al., 2016). Due to the low likelihood of sampling the negative $\varepsilon^{182}W$ anomaly as a residual of the late veneer, this reservoir can be excluded from being considered as the residue that is dominated by a late veneer signature. As mentioned in Puchtel et al., (2016), the isotope composition of this reservoir may be best explained by as having been formed post-core formation, through silicate crystal-liquid differentiation before ^{182}Hf was extinct by 60 Myr.

It has been suggested that the $^{142}Nd/^{144}Nd$ record and $^{182}W/^{184}W$ record with respect to terrestrial samples throughout time may be difficult to reconcile with a common mixing rate (Rizo et al., 2016b). This is because both the $^{142}Nd/^{144}Nd$ and $^{182}W/^{184}W$ ratios record signatures of early Earth differentiation, while exhibiting different data trends as a function of time in the rock record. $^{142}Nd/^{144}Nd$ ratios are not affected by the late veneer, while, $^{182}W/^{184}W$ ratios are. $^{142}Nd/^{144}Nd$ ratios tend to have a broader distribution of values ranging in 40 ppm, with a distribution to 30 ppm as recent as 2.7 Ga, whose variations are observed to decline throughout time. $^{182}W/^{184}W$ ratios mostly

tend to exhibit an elevated signature of around 15 ppm throughout most of the Archean and the post Archean (**Fig. 7–8**), with a convergence to $\varepsilon^{182}W = 0$ at time zero (modern day). It is demonstrated that it is possible to apply a consistent mixing rate of 500 Myr to both the ^{182}Hf-^{182}W and ^{146}Sm-^{142}Nd systems (Hyung and Jacobsen, *under review*) to explain a large proportion of how the W isotopic signature is sampled throughout time despite the differences in the data distribution. $\varepsilon^{182}W$ data are shown to be mostly elevated from the terrestrial reference point of 0, whereas $\mu^{142}Nd$ data are demonstrated to more or less have positive and negative anomalies whose distributions are less skewed in one direction over another. Such a disparity in data distribution among the two extinct isotope systems may be a reflection of the differences in the relative sizes of the "enriched" and "depleted" reservoirs for each of the isotope systems.

Contrary to expectations, even if for the involvement of a very small thin layer that is small in terms of mass, our model dictates that a long period of time is necessary to thoroughly mix late veneer material into the mantle, owing to the sheer size of the total mantle. According to scenario (A), the likelihood of sampling the "late veneer" signature material throughout the history of the Earth is very low, until the mantle is close to homogenization.

The delivery of the late veneer is relevant to isotope systems that are characterized to be highly siderophile. A point of consideration is the highly siderophile long-lived ^{187}Re-^{187}Os system (with a half-life of 41.2 Gyr), which consist of HSEs. $^{187}Os/^{188}Os$ isotope signature of Isua samples that are dated to be 3.8 Ga in age. The rock record in terms of Os isotopic composition of most rocks are deemed to be chondritic from the very earliest rock records. Owing to the difference in the partition coefficients of Re and Os, the resulting $^{187}Os/^{188}Os$ of the value after core formation is calculated to have had an

elevated signature compared to chondrites or the modern day mantle at around $^{187}Os/^{188}Os = 0.15$ or higher (Walker, 2009). The early rock record in places such as Isua (Rizo et al., 2016b) has reflected an $^{187}Os/^{188}Os$ composition of around 0.10 In contrast to the early rock record, modern day mantle peridotites are measured to have elevated $^{187}Os/^{188}Os$ isotopic ratios of at around 0.130, which is higher than measured carbonaceous chondrites (at around 0.126) at present day. The $^{187}Os/^{188}Os$ isotopic ratios are most similar to ordinary chondrites, which lack in similarities in the D/H ratios of the oceans, and in bulk volatile content. There is currently no consensus on the exact mechanism involved for the evolution of the Os isotope signatures for the terrestrial rock record throughout time.

The situation dictates a potential necessity for exploring cases of fast mixing in which a chondritic late veneer is fully mixed into the mantle within the first 1 Gyr. In exploring a scenario which employs the initial homogenization of the late veneer into an upper mantle volume (scenario (B)), we find that it is possible to decrease the timing at which the late veneer is thoroughly mixed into the mantle volume, by 20% (0.5 Gyr). Although the involvement of just the upper mantle is still insufficient to decrease the time scale of late veneer homogenization to less than 1 Gyr in such a case, the process may suggest that the 3.8 Ga Isua samples that demonstrate chondritic $^{187}Os/^{188}Os$ values, must be sourced from a mantle reservoir that was small enough to have homogenized quickly. In addition, it is possible to consider that mixing the late veneer into fraction of the mantle as a liquid magma ocean, in contrast to a solid mantle may have possibly induced a faster rate of mixing due to turbulent processes (Tonks and Melosh, 1993). An interpretation involving the delivery of the late veneer into a magma ocean may need care because of its effects on the outgassing of volatiles (Elkins-Tanton, 2012).

In contrast to scenario (A), scenario (B) is capable of potentially forming a distinct silicate reservoir that has formed post-core formation, which neither resembles the dominant mantle $\varepsilon^{182}W$ value after core formation nor the $\varepsilon^{182}W$ signature of the late veneer itself. In such a case, the presence of a reservoir with lower $\varepsilon^{182}W$ value (e.g., at 0.11) than the bulk mantle post-core formation, may be explained without invoking a complementary mantle reservoir according to the fractionation processes involved due to the difference in the partition coefficients of Hf and W while ^{182}Hf is still alive.

The extreme variability of $\varepsilon^{182}W$ discovered in some present-day flood basalts (Rizo et al., 2016b) and ocean island basalts (OIBs) (Mundl et al., 2017) have been attributed to different processes. The extreme positive anomalies varying up to $\varepsilon^{182}W = 0.48$ (**Fig. 7**) have been attributed to large impactors that would have created reservoirs that equilibrated with the core very early on in Earth's history, after a large portion of the Earth's core had already been formed, but prior to the delivery of the late veneer. The negative $\varepsilon^{182}W$ values of modern-day OIBs have been thought to represent sampling from the D" layer near the core-mantle boundary owing to the suggested negative correlation between the $\varepsilon^{182}W$ isotopes and $^{3}He/^{4}He$ ratios. A small fraction of the data are characterized by large variations (up to 0.19) in $^{187}Os/^{188}Os$ ratios. Such indications may hint at either the presence of recycled material or a complex processes involved during the differentiation of the core and the mantle. Although the modern day W isotope distribution affirms pockets of mantle parcels that are not equally mixed to be completely homogenized at present day, an alternative hypothesis may be that the W isotopic composition of the bulk of the terrestrial mantle is still evolving toward a more negative $\varepsilon^{182}W$ isotopic composition, rather than having been homogenized at 0.

Barring the extreme variability of $\varepsilon^{182}W$ discovered in some present-day flood basalts and OIBs (Mundl et al., 2017; Rizo et al., 2016b), with this type of model presented in this study, it is possible to reconcile the difference in the data distribution for the two short-lived isotope systems throughout time, with a consistent rate of mixing. Likely such a distribution disparity of the distribution of data of one system with respect to other isotope systems, is a reflection of the sizes of the reservoirs of the "enriched" (e.g., negative $\mu^{142}Nd$, positive $\varepsilon^{182}W$) and "depleted" (e.g., positive $\mu^{142}Nd$, negative $\varepsilon^{182}W$) reservoirs that have formed due to the different chemical affinities (lithophile, siderphile) of the isotope systems and the extent of their involvement during the early differentiation processes (core-mantle differentiation pertaining to the ^{182}Hf-^{182}W system, silicate mantle differentiation primarily pertaining to the ^{146}Sm-^{142}Nd) of the Earth.

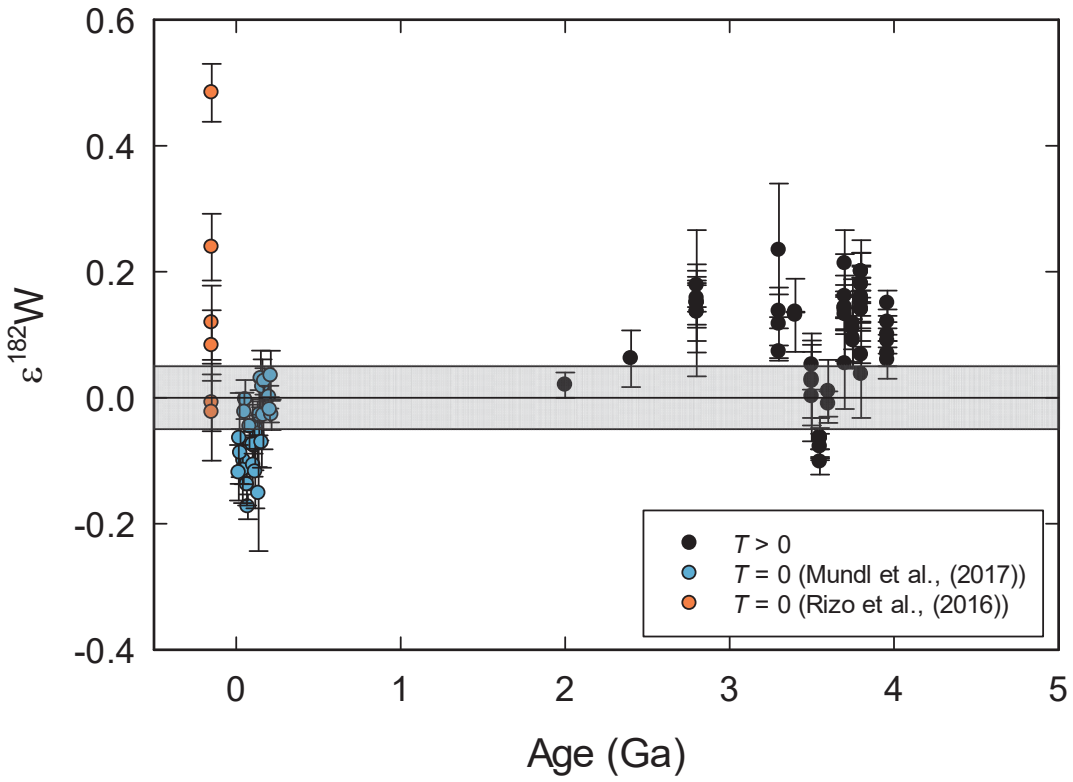

Fig. 7. $\varepsilon^{182}W$ ratios of terrestrial samples, plotted as a function of time. The negative $\varepsilon^{182}W$ measurements for the modern-day OIB samples at around $T = 0$ are slightly offset from their age, for clarity in presentation. Data are from (Liu et al., 2016; Mundl et al., 2017; Rizo et al., 2016b, 2016a, Touboul et al., 2014, 2013, 2012, Willbold et al., 2015, 2011). The $\varepsilon^{182}W$ isotopic values of the Vetreny komatiites at 2.4 Ga are represented by their average (n = 5) and the 2σ standard deviation (Touboul et al., 2013) rather than their individual values as the data is unpublished. The horizontal line at $\varepsilon^{182}W = 0$ represents the present day, well-mixed terrestrial mantle. The shaded bands represent the typical 2σ external reproducibility for $\varepsilon^{182}W$ isotope measurements.

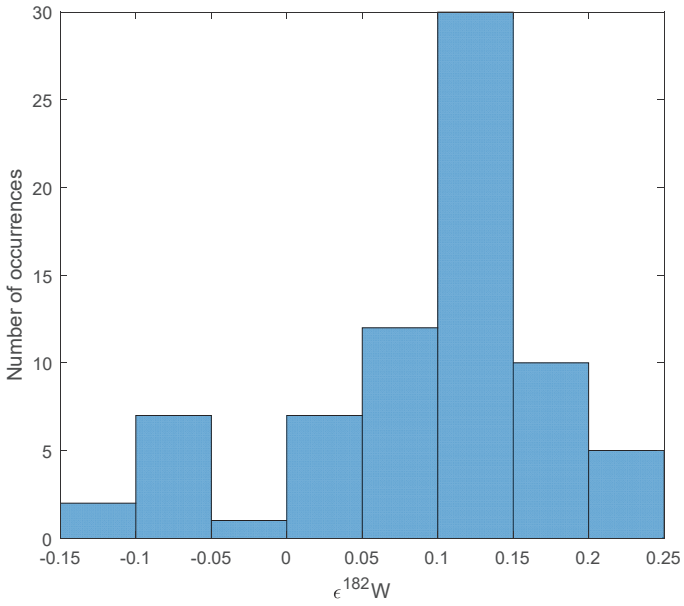

Fig. 8. Measured distribution of ε^{182}W-values, spanning from ages 2.4 Ga to 4 Ga. It is worth noting a peak sample distribution around $\varepsilon^{182}W = 0.15$. The error bars for the samples whose measurements are higher than 0.20 are at 2σ=0.05–0.10 ε units.

Summary and Conclusion

In considering the scenario where a late veneer is mixed into the mantle as a thin layer, we find a number of things:

(a) The late veneer takes a long time to mix into the mantle. It is possible to have the W isotope anomaly of the mantle from core formation that may persist into the late Archean.

(b) The mixing rate and volumetric proportions of the mantle involved have a larger effect on the time scale of the mixing of the late veneer rather than the W concentration and the W isotopic composition of the mantle.

(c) The same rate of mixing can reconcile a positive $^{182}W/^{184}W$ isotope anomaly persisting into the late Archean, as well as the $^{142}Nd/^{144}Nd$ isotope data distribution throughout the Earth.

(d) If a fraction of the mantle was homogenized with the late veneer, it may form a distinct reservoir whose W isotope composition is smaller than that of the mantle after core formation. If the homogenization of the two reservoirs has sufficiently progressed before whole mantle mixing, it may be sampled. In such a case, a complementary W isotopic reservoir is not necessary.

(e) The model affirms the presence of extreme W isotope anomalies at modern day that there are portions of the mantle that preserve isotopic heterogeneity that has formed in the Hadean that has not been equally mixed and sampled.

(f) An early mantle that has homogenized with the late veneer within 1 Gyr, may require a faster rate of mixing, a smaller mantle reservoir that has homogenized with the mantle before whole mantle mixing, or the delivery of a late veneer into a turbulent magma ocean.

References

Arevalo, R., McDonough, W.F., 2008. Tungsten geochemistry and implications for understanding the Earth's interior. Earth Planet. Sci. Lett. 272, 656–665. https://doi.org/10.1016/j.epsl.2008.05.031

Chou, C.L., 1978. Fractionation of siderophile elementsin the Earth's upper mantle. Proc. Lunar Planet. Sci. Conf. 9th 9, 219–230.

Drake, M.J., Righter, K., 2002. Determining the composition of the Earth. Nature 416, 39–44. https://doi.org/10.1038/416039a

Elkins-Tanton, L.T., 2012. Magma oceans in the inner solar system. Annu. Rev. Earth Planet. Sci. 40, 113–139. https://doi.org/10.1146/annurev-earth-042711-105503

Friedman A M, 1966. Alpha decay half-lives of ^{148}Gd, ^{150}Gd and ^{146}Sm. Radiochim. Acta 5, 192–194.

Horan, M.F., Carlson, R.W., Walker, R.J., Jackson, M., Garçon, M., Norman, M., 2018. Tracking Hadean processes in modern basalts with 142-Neodymium. Earth Planet. Sci. Lett. 484, 184–191. https://doi.org/10.1016/j.epsl.2017.12.017

Hyung, E., Jacobsen, S.B., n.d. ^{142}Nd/^{144}Nd variations support a Hadean origin of plate tectonics as well as limited preservation of Hadean heterogeneity in the modern mantle. Nat. Commun.

Jacobsen, S.B., Yu, G., 2015. Extinct isotope heterogeneities in the mantles of Earth and Mars: implications for mantle stirring rates. Meteorit. Planet. Sci. 50, 555–567.

Jochum, K.P., 1996. Rhodium and other platinum-group elements in carbonaceous chondrites. Geochim. Cosmochim. Acta 60, 3353–3357. https://doi.org/10.1016/0016-7037(96)00186-X

Kellogg, J.B., Jacobsen, S.B., O'Connell, R.J., 2007. Modeling lead isotopic heterogeneity in mid-ocean ridge basalts. Earth Planet. Sci. Lett. 262, 328–342. https://doi.org/10.1016/j.epsl.2007.06.018

Kellogg, J.B., Jacobsen, S.B., O'Connell, R.J., 2002. Modeling the distribution of isotopic ratios in geochemical reservoirs. Earth Planet. Sci. Lett. 204, 183–202.

Kinoshita, N., Paul, M., Kashiv, Y., Collon, P., Deibel, C.M., DiGiovine, B., Greene, J.P., Henderson, D.J., Jiang, C.L., Marley, S.T., Nakanishi, T., Pardo, R.C., Rehm, K.E., Robertson, D., Scott, R., Schmitt, C., Tang, X.D., Vondrasek, R., Yokoyama, A., 2012. A shorter ^{146}Sm half-life measured and implications for ^{146}Sm-^{142}Nd chronology in the solar system. Science (80-.). 335, 1614–1617.

Kleine, T., Mezger, K., Münker, C., Palme, H., Bischoff, A., 2004. ^{182}Hf-^{182}W isotope systematics of chondrites, eucrites, and martian meteorites: Chronology of core formation and early mantle differentiation in Vesta and Mars. Geochim.

Cosmochim. Acta 68, 2935–2946. https://doi.org/10.1016/j.gca.2004.01.009

Kleine, T., Münker, C., Mezger, K., Palme, H., 2002. Rapid accretion and early core formation on asteroids and the terrestrial planets from Hf-W chronometry. Nature 418, 952–955. https://doi.org/10.1038/nature00982

Liu, J., Touboul, M., Ishikawa, A., Walker, R.J., Graham Pearson, D., 2016. Widespread tungsten isotope anomalies and W mobility in crustal and mantle rocks of the Eoarchean Saglek Block, northern Labrador, Canada: Implications for early Earth processes and W recycling. Earth Planet. Sci. Lett. 448, 13–23. https://doi.org/10.1016/j.epsl.2016.05.001

Marchi, S., Canup, R.M., Walker, R.J., 2018. Heterogeneous delivery of silicate and metal to the Earth by large planetesimals. Nat. Geosci. 11, 77–81. https://doi.org/10.1038/s41561-017-0022-3

McDonough, W., Sun, S. -s., 1995. The composition of the Earth. Chem. Geol. 120, 223–253. https://doi.org/10.1016/0009-2541(94)00140-4

Morgan, J.W., Walker, R.J., Brandon, A.D., Horan, M.F., Gold, A., 2001. Siderophile Elements in Earth's Upper Mantle and Lunar Breccias: Manifestations of the Same Late Influx. Meteorit. Planet. Sci. 36, 1257–1275.

Mundl, A., Touboul, M., Jackson, M.G., Day, J.M.D., Kurz, M.D., Lekic, V., Helz, R.T., Walker, R.J., 2017. Tungsten-182 heterogeneity in modern ocean island basalts. Science (80-.). 356, 66–69. https://doi.org/10.1126/science.aal4179

Peters, B.J., Carlson, R.W., Day, J.M.D., Horan, M.F., 2018. Hadean silicate differentiation preserved by anomalous142Nd/144Nd ratios in the Réunion hotspot source. Nature 555, 89–93. https://doi.org/10.1038/nature25754

Puchtel, I.S., Blichert-Toft, J., Touboul, M., Horan, M.F., Walker, R.J., 2016. The coupled ^{182}W-^{142}Nd record of early terrestrial mantle differentiation. Geochemistry, Geophys. Geosystems 17, 2168–2193.

Rizo, H., Walker, R.J., Carlson, R.W., Horan, M.F., Mukhopadhyay, S., Manthos, V., Francis, D., Jackson, M.G., 2016a. Preservation of Earth-froming events in the tungsten isotopic composition of modern flood basalts. Science (80-.). 352, 809.

Rizo, H., Walker, R.J., Carlson, R.W., Touboul, M., Horan, M.F., Puchtel, I.S., Boyet, M., Rosing, M.T., 2016b. Early Earth differentiation investigated through ^{142}Nd, ^{182}W, and highly siderophile element abundances in samples from Isua, Greenland. Geochim. Cosmochim. Acta 175, 319–336. https://doi.org/10.1016/j.gca.2015.12.007

Tonks, W.B., Melosh, H.J., 1993. Magma ocean formation due to giant impacts. J. Geophys. Res. 98, 5319–5333.

Touboul, M., Liu, J., O'Neil, J., Puchtel, I.S., Walker, R.J., 2014. New insights into the Hadean mantle revealed by ^{182}W and highly siderophile element abundances of

supracrustal rocks from the Nuvvuagittuq Greenstone Belt, Quebec, Canada. Chem. Geol. 383, 63–75. https://doi.org/10.1016/j.chemgeo.2014.05.030

Touboul, M., Puchtel, I.S., Walker, R.J., 2013. Tungsten isotope heterogeneities in Archean komatiites. Mineral. Mag. 77, 2348.

Touboul, M., Puchtel, I.S., Walker, R.J., 2012. ^{182}W evidence for long-term preservation of early mantle differentiation products. Science (80-.). 335, 1065–1069. https://doi.org/10.1126/science.1216351

Walker, R.J., 2009. Highly siderophile elements in the Earth, Moon and Mars: Update and implications for planetary accretion and differentiation. Chemie der Erde 69, 101–125. https://doi.org/10.1016/j.chemer.2008.10.001

Willbold, M., Elliott, T., Moorbath, S., 2011. The tungsten isotopic composition of the Earth's mantle before the terminal bombardment. Nature 477, 195–8. https://doi.org/10.1038/nature10399

Willbold, M., Mojzsis, S.J., Chen, H.W., Elliott, T., 2015. Tungsten isotope composition of the Acasta Gneiss Complex. Earth Planet. Sci. Lett. 419, 168–177. https://doi.org/10.1016/j.epsl.2015.02.040

Yin, Q.Z., Jacobsen, S.B., Yamashita, K., Blichert-Toft, J., Télouk, P., Albarède, F., 2002. A short timescale for terrestrial planet formation from Hf-W chronometry of meteorites. Nature 418, 949–952. https://doi.org/10.1038/nature00995

CHAPTER 6

Conclusions

Through the studies presented in the dissertation, it is possible to make statements on the state of the mantle. It is shown that the consideration of a realistic Earth composition that includes minor elements is fairly important in the calculation of the lower mantle sound velocity profiles. Notably, the partitioning of Fe-Mg in bridgmanite and ferropericlase at lower mantle conditions can be said to primarily be affected by Al and temperature. Using better constraints, it is possible to modify shear-wave velocity profile calculations of the lower mantle. In considering the possibility of a large-scale magma ocean, if there was a Si-rich mantle that has once formed, the fractionation of $^{176}Hf/^{177}Hf$ as well as with $^{143}Nd/^{144}Nd$ signatures would have been too strong compared to the present day Hf-Nd data array, owing to the involvement of Ca-perovskite and the shear volumetric proportion of the Si-rich bridgmanite in the lower mantle. It can be deduced that the mantle is currently not chemically stratified at the 660-km discontinuity, implying that whole-mantle convection was in operation. It is possible that early large scale features have been erased due to this process.

With advances in the precision of $^{142}Nd/^{144}Nd$ measurements for the thermal ionization mass spectrometer, it has become possible to detect small $^{142}Nd/^{144}Nd$ isotopic anomalies that are unresolvable at $2\sigma = \pm 5$ ppm precision. It is possible for the mantle to preserve small $^{142}Nd/^{144}Nd$ heterogeneities formed in the Hadean in mid-ocean ridge basalts (MORB). The majority of modern-day samples that were selected and measured, have $^{142}Nd/^{144}Nd$ distributions that agree with within $2\sigma < \pm 2$ ppm, implying large-scale

homogenization of the modern-mantle amidst heterogeneity. The distribution of $^{142}Nd/^{144}Nd$ isotopes throughout the Archean and into the post-Archean suggest that plate tectonics may have been operating starting in the Hadean.

Through analyzing Mg isotopes and major elements of Oslo Rift melilities, it is deduced that CO_2 in lavas can be supplied by the background CO_2 of the peridotitic mantle, over an addition of carbonates to the source through carbonated lithologies or metasomatism. The analysis presents the first evidence that HIMU, traditionally thought to be a tracer of recycled oceanic crust, is sourced from the normal peridotitic mantle rather than pyroxenititc (more characteristic of recycled content) sources. The generation of highly fractionated compositions being sourced from the peridotitic mantle, imply the importance of possible factors such as lithospheric thickness than heterogeneous source compositions in their genesis, and provide better constraints for the extent of involvement of recycled crustal material in the genesis of lavas.

Late veneer material, if assumed to have initially been a thin layer on the upper part of the mantle, takes a long time to fully homogenize into the mantle, during which it is possible to sample elevated mantle W isotope signatures generated during core-formation. Despite the vast differences in the data distribution of measured $^{142}Nd/^{144}Nd$ and $^{182}W/^{184}W$ ratios as a function of time, it is still possible to resolve the data through a common mixing rate, which is deduced to be around 500 Myr according to similar models.

Overall, it may be concluded that large-scale mixing processes likely dominated the terrestrial mantle throughout most of its time, with the potential to erase large scale features. Despite the scale at which the mantle was and is currently being mixed, and the process in which the Earth has gone through homogenization over billions of years, it is shown that it

is possible for isotopic heterogeneities to survive over long periods of time. Normal mantle sources for extreme compositions possibly highlight the importance of dynamic processes in producing geochemical heterogeneity. The implications regarding the delivery, extent, and time scale of mixing of the late veneer and presence of plate tectonics in the early history of the Earth, will further elucidate the conditions in which a terrestrial planet may harbor the conditions that are conducive to life.

Appendix I

Supplementary Information to Chapter 2

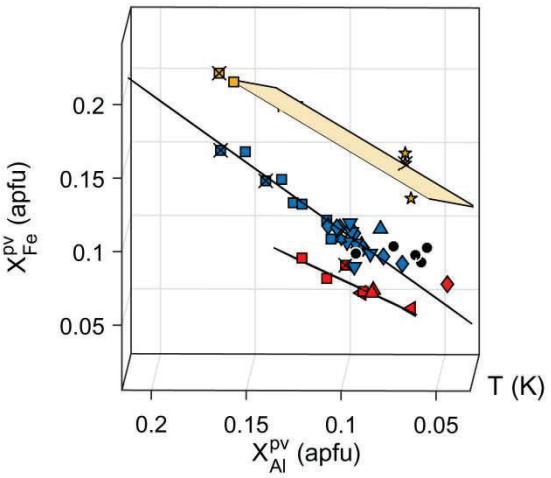

The data of Wood (2000), shown by the black circles, deviate significantly as a group from established trends and were excluded from calculation of regression coefficients.

Reference

Wood, B.J., 2000. Phase transformations and partitioning relations in peridotite under lower mantle conditions. Earth Planet. Sci. Lett. 174, 341–354.

APPENDIX II: Supplementary Information File to Chapter 3

Sample Characterization and Data

Sample characterization

Major and trace element data for the samples are given in Table S1. Rare earth element patterns for the MORBs and OIBs are shown in Fig. S1. KN207-2 (24.913 to 24.920°N, 45.578 to 45.570°W) is an Atlantic N-MORB. CH59-2 (8.000°N, 102.840°W) is also an N-MORB from the East Pacific Rise whose provenance is free from hotspot and subduction zone influences. A12DR44 (35.326°N, 34.859°E) is characterized as an EM1 MORB. HLY102-096 (86.14°N, 31.78°E) is a slightly enriched MORB from the Gakkel ridge (Sohn et al., 2008). RC2806 2D-1 is a HIMU MORB from the south Atlantic (Schilling et al., 1994, 1995). DICE is a depleted Icelandic plume sample that has been used for extensive noble gas isotope studies (Ballentine and Barfod, 2000; Harrison et al., 1999; Mukhopadhyay, 2012). BHVO-2 is an OIB from the Kilauea crater of Hawaii (Weiss et al., 2005).

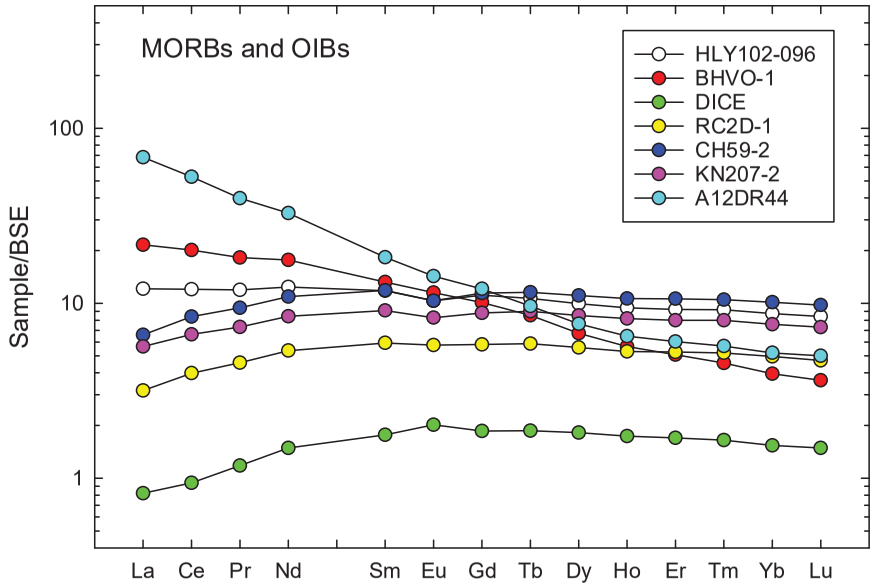

Fig. S1. Plot of REEs for young ($T = 0$) MORBs and OIBs.

Rare earth element patterns for the Baltic Shield samples are shown in Fig. S2. K410 is a sample of the Vinoren gabbro from the Kongsberg sector of S. Norway. It is characterized by a relatively flat MORB-like REE pattern and its age is 1.20 Ga(Jacobsen and Heier, 1978). E-58 (Oevre Eiker) a 1.58 Ga deep crustal granulite facies quartz diorite (Jacobsen and Heier, 1978) from the Kongsberg sector of S. Norway. RAM-3 (Raftsund) is a 1.792 Ga medium-coarse grained deep crustal mangerite rich in K-feldspar (Corfu, 2004) from the Lofoten are of N. Norway. GN-12-03 (Gardnos) is a 1.08 Ga upper crustal granite (Jaret et al., 2016) from right north of the Gardnos impact crater in Hallingdal of S. Norway. HE-5 (Herefoss) is a coarse-grained 0.926 Ga

upper crustal granite[11] with a negative Eu anomaly and from the Bamble sector of S. Norway. K1714 is a trachy-andesite with an age of 288 Ma that is highly enriched in REE (Sundvoll et al., 1990) and from the Krokskogen area of the Oslo Rift of S. Norway.

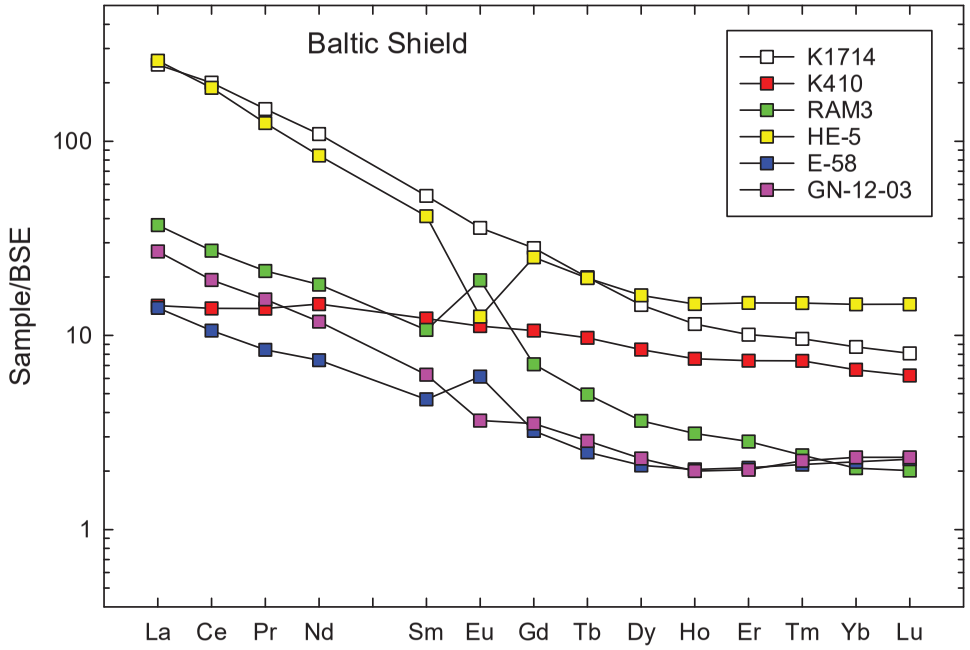

Fig. S2. Plot of REEs for samples from the Baltic Shield. The ages of the samples range from 300 Ma to 1.9 Ga.

Table S1. Major and trace element compositions of the samples

	HLY102-096	BHVO-2	DICE	RC2806 2D-1	CH59-2	KN207-2	A12DR44	K1714	K410	RAM-3	HE-5	E-58	GN-12-03
Major oxides (wt%)													
SiO_2	50.36	49.46	58.50	48.69	49.33	50.82	45.71	52.31	44.66	58.19	68.13	67.96	69.32
TiO_2	1.84	2.77	0.59	1.07	2.08	1.47	2.45	1.61	2.15	0.95	0.53	0.36	0.22
Al_2O_3	16.44	14.42	8.02	18.59	14.66	15.53	17.72	19.86	16.28	19.68	15.21	13.98	16.56
FeO	9.28	10.97	9.09	7.81	11.82	9.46	6.91	5.62	13.77	3.98	3.13	6.98	1.96
MnO	0.16	0.17	0.17	0.15	0.21	0.17	0.13	0.14	0.20	0.09	0.06	0.15	0.04
MgO	7.45	7.41	12.71	8.36	7.28	8.47	9.03	1.53	9.32	1.09	0.69	1.79	0.57
CaO	10.04	11.45	9.86	12.55	11.32	10.74	11.89	6.30	9.74	2.59	2.12	4.73	2.56
Na_2O	3.68	2.45	1.02	2.61	2.95	3.04	3.22	6.30	2.87	5.48	3.65	3.39	4.71
K_2O	0.45	0.63	0.02	0.07	0.14	0.14	2.24	5.54	0.65	7.71	6.33	0.47	3.99
P_2O_5	0.30	0.28	0.02	0.10	0.20	0.16	0.70	0.79	0.35	0.24	0.14	0.19	0.08
Elements (ppm)													
Li	6.92	4.18	2.21	4.68	7.29	6.36	5.04	24.7	5.89	9.23	30.1	6.16	26.6
Be	0.77	0.82	0.10	0.81	0.63	0.45	1.92	9.58	0.86	0.99	5.69	1.34	1.53
B	8.18	0.32	2.75	4.77	1.56	3.37	7.34	7.45	2.58	1.20	3.50	1.28	4.54
Na	27308	18166	7545	19329	21900	22534	23923	46708	21323	40644	27088	25144	34911
Mg	44941	44702	76640	50407	43873	51060	54453	9231	56203	6581	4182	10786	3412
Al	87000	76292	42466	98378	77578	82212	93797	10509 4	86185	10416 8	80504	73994	87663
P	1298	1226	71	449	879	687	3046	3453	1529	1031	625	827	354
K	3695	5222	204	615	1180	1139	18605	46018	5428	63998	52549	3902	33090
Ca	71777	81809	70500	89712	80931	76785	84962	45025	69578	18544	15152	33792	18265
Sc	33.5	31.4	23.4	31.3	43.4	38.1	32.4	11.0	28.5	11.4	6.16	16.9	3.92
Ti	11023	16586	3531	6440	12469	8812	14678	9664	12912	5678	3158	2186	1289

Mn	1274	1311	1315	1127	1659	1344	1045	1060	1556	696	497	1137	315
Fe	72112	85296	70620	60721	91915	73535	53684	43703	10704 0	30925	24320	54286	15249
V	266	307	199	228	377	270	224	70.7	239	34.8	26.5	44.3	9.80
Cr	262	280	535	409	227	326	300	8.27	146	29.8	56.6	36.3	39.7
Co	40.0	43.8	77.8	38.9	43.8	41.5	36.6	22.4	69.5	3.40	4.45	12.1	2.27
Ni	130	116	555	141	75	136	187	9.52	218		1.86	3.20	3.21
Cu	58.7	133	84.4	74.8	64.5	67.4	64.5	25.7	74.8	6.74	6.91	35.6	3.97
Zn	137	106	103	86.4	131	104	115	198	154	91.5	99.7	79.9	61.4
Ga	17.5	20.5	9.27	14.2	18.2	15.4	20.3	42.9	20.0	20.2	34.0	12.8	17.5
Rb	4.82	9.09	0.21	0.37	0.85	1.21	42.9	167	13.1	72.2	288	4.24	113
Sr	168	362	81.8	128	118	127	642	1955	235	272	195	211	338
Y	41.8	25.4	7.05	23.6	47.7	35.1	28.5	49.1	34.5	14.1	72.5	9.57	9.93
Zr	153	161	9.33	66.3	139	103	303	1372	71.7	8.13	259	4.08	54.8
Nb	9.1	17.8	0.50	1.32	2.70	2.81	68.1	203	4.30	6.22	35.5	1.61	5.04
Mo	1.13	0.90	0.101	0.67	0.57	0.46	2.23	4.53	0.66	0.79	17.4	1.01	0.77
Ag	0.060	0.079	0.018	0.019	0.055	0.046	0.107	0.271	0.053	0.039	0.090	0.001	0.027
Cd	0.161	0.087	0.066	0.115	0.158	0.118	0.134	0.164	0.123	0.035	0.045	0.039	0.039
Sn	1.23	2.01	0.32	0.84	1.43	0.98	3.41	6.08	1.15	1.02	3.62	0.41	2.03
Sb	0.045	0.162	0.019	0.067	0.041	0.043	0.098	0.360	0.162	0.036	0.075	0.131	0.115
Cs	0.0577	0.0937	0.001 8	0.0038	0.009 3	0.014 4	0.64	2.08	0.65	0.19	2.20	1.20	7.04
Ba	71.7	133	4.89	4.54	8.1	12.1	369	1009	160	2411	735	143	580
La	7.84	14.0	0.53	2.05	4.27	3.66	44.2	161	9.23	24.0	168	8.98	17.5
Ce	20.1	33.7	1.58	6.67	14.1	11.1	88.5	335	23.1	45.8	316	17.7	32.3
Pr	3.03	4.64	0.30	1.16	2.39	1.86	10.1	37.2	3.50	5.46	31.5	2.14	3.90
Nd	15.5	22.1	1.86	6.70	13.6	10.53	40.9	136	18.1	22.8	105	9.31	14.7
Sm	4.79	5.37	0.72	2.41	4.81	3.70	7.43	21.2	4.96	4.34	16.7	1.90	2.55
Eu	1.59	1.77	0.31	0.89	1.59	1.28	2.20	5.52	1.72	2.96	1.93	0.94	0.56
Gd	6.05	5.49	1.01	3.16	6.22	4.79	6.58	15.3	5.77	3.86	13.7	1.75	1.91
Tb	1.06	0.84	0.19	0.58	1.14	0.89	0.95	1.97	0.96	0.49	1.96	0.25	0.28
Dy	6.70	4.54	1.23	3.76	7.47	5.73	5.14	9.67	5.70	2.45	10.8	1.44	1.56
Ho	1.40	0.84	0.26	0.79	1.59	1.22	0.96	1.71	1.13	0.47	2.16	0.30	0.30

Er	4.04	2.22	0.74	2.30	4.65	3.50	2.65	4.42	3.24	1.24	6.44	0.91	0.89
Tm	0.62	0.31	0.11	0.35	0.71	0.54	0.39	0.65	0.50	0.16	1.00	0.15	0.15
Yb	3.85	1.74	0.68	2.19	4.48	3.35	2.29	3.84	2.93	0.91	6.38	0.98	1.04
Lu	0.57	0.25	0.101	0.32	0.66	0.49	0.34	0.55	0.42	0.14	0.98	0.16	0.16
Hf	3.64	3.84	0.34	1.72	3.57	2.72	7.22	26.7	1.89	0.24	7.58	0.13	1.55
Ta	0.55	1.02	0.07	0.12	0.19	0.17	3.80	10.5	0.27	0.23	2.18	0.04	0.39
W	0.29	0.26	0.026	0.11	0.08	3.47	2.20		0.19	0.10	0.35	0.054	0.35
Tl	0.12	0.039	0.001 1	0.013	0.011	0.011	0.090	0.059	0.11	0.43	1.98	0.033	0.93
Pb	0.87	1.98	0.103	0.28	0.52	0.46	3.11	13.7	2.40	16.0	35.3	2.74	15.3
Bi	0.014	0.011	0.005 0	0.0066	0.008 6	0.007 0	0.0109	0.0064	0.0269	0.0039	0.034 0	0.018 8	0.064 5
Th	0.67	1.10	0.019	0.067	0.15	0.20	4.23	28.9	0.86	0.48	95.6	0.26	3.17
U	0.29	0.36	0.008 6	0.055	0.067	0.067	1.05	7.37	0.29	0.17	15.2	0.12	1.10

Isotopic measurements

Table S2. $^{142}Nd/^{144}Nd$ measurements of standards

	RED1
NdA	1.1418412
NdA	1.1418412
NdA	1.1418397
NdA	1.1418393
NdA	1.1418408
NdA	1.1418404
NdA	1.1418401
NdA	1.1418397
NdA	1.1418409
NdA	1.1418390
NdA	1.1418403

NdA	1.1418409
NdA	1.1418400
NdA	1.1418416
NdA	1.1418398
NdA	1.1418392
JNdi	1.1418390
JNdi	1.1418394
JNdi	1.1418396
JNdi	1.1418400
JNdi	1.1418401
JNdi	1.1418391
JNdi	1.1418381
JNdi	1.1418397
JNdi	1.1418402
JNdi	1.1418399
Nd-β	1.1418421
Nd-β	1.1418418
Nd-β	1.1418415
Nd-β	1.1418419
Nd-β	1.1418402
Nd-β	1.1418402
Nd-β	1.1418406
Nd-β	1.1418413

SI Figure 3.

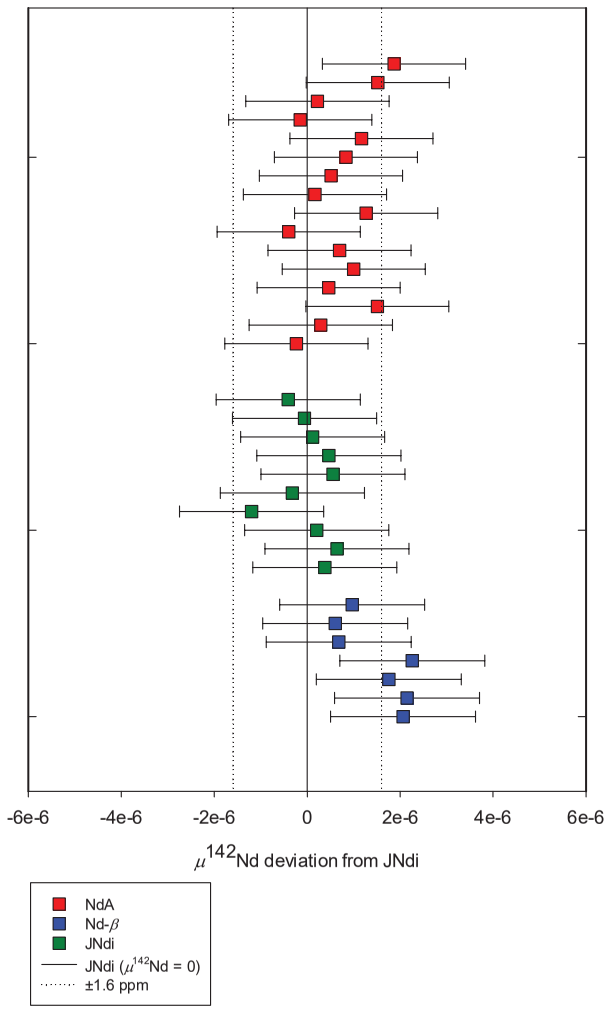

Fig. S3. Measurements of various standards and their 2σ internal standard error precision (in grey), plotted with external precision (solid). The measurements agree well within one another to within an external reproducibility level of a 2σ standard deviation of ±1.6 ppm. The average for each of the standards are 1.1418402 for Nd-A (2SE = 0.39 ppm), 1.1418395 for JNdi (2SE = 0.40), and 1.1418412 for Nd-β (2SE = 0.54) when the data is reduced through Reduction Method 1 (RED1).

Table S3. Isotopic measurements of samples

Sample name	Age (Ga)	$^{147}Sm/^{144}Nd$	$^{143}Nd/^{144}Nd$	2σ	□$^{143}Nd(0)$	2σ	$^{142}Nd/^{144}Nd$	2σ	$\mu^{142}Nd$	2σ	N
KN207-2	0	0.2213	0.5131555	3.85E-06	10.03	0.14	1.14183605	1.18E-06	-3.02	1.27	2
CH59-2	0	0.2223	0.5131645	3.83E-06	10.27	0.12	1.14183915	2.21E-06	-0.31	0.42	2
HLY102-096	0	0.1948	0.5132583	2.14E-06	12.10	0.39	1.14183955	2.07E-06	0.04	1.56	2
A12DR44	0	0.1147	0.5126785	2.68E-06	0.79	0.14	1.14184125	1.53E-06	1.53	0.42	2
RC2806 2D-1	0	0.2267	0.5132176	1.94E-06	11.31	0.39	1.14183935	2.21E-06	-0.13	0.14	2
DICE	0	0.2432	0.5130640	3.52E-06	8.31	0.14	1.14184023	2.17E-06	0.64	0.94	2
BHVO-2	0	0.1564	0.5129673	1.84E-06	6.42	0.12	1.14183987	2.85E-06	0.32	0.23	3
K1714	0.290	0.1027	0.5126077	3.81E-06	-0.59	0.12	1.14183903	2.00E-06	-0.41	0.70	3
HE-5	0.926	0.0971	0.5118780	2.24E-06	-14.83	0.14	1.14184210	1.20E-06	2.28	1.60	3
K410	1.200	0.1707	0.5125769	1.90E-06	-1.19	0.12	1.14184130	1.87E-06	1.58	1.60	1
GN-12-03	1.080	0.1091	0.5118885	1.09E-06	-14.62	0.12	1.14183660	1.82E-06	-2.54	1.41	2
E-58	1.580	0.1289	0.5120823	2.89E-06	-10.84	0.12	1.14184200	2.88E-06	2.19	1.60	1
RAM-3	1.792	0.1172	0.5114208	2.02E-06	-23.74	0.12	1.14184223	1.69E-06	2.49	0.98	2

2σ errors for $^{142}Nd/^{144}Nd$ are determined by the standard deviations of multiple measurements. 2σ uncertainties for single measurements are indicated by the external reproducibility based on standards (N=34) in this study.

References

Ballentine, C.J., Barfod, D.N., 2000. The origin of air-like noble gases in MORB and OIB. Earth Planet. Sci. Lett. 180, 39–48.

Corfu, F., 2004. U–Pb Age, Setting and Tectonic Significance of the Anorthosite-Mangerite-Charnockite-Granite Suite, Lofoten-Vesteralen, Norway. J. Petrol. 45, 1799–1819.

Harrison, D., Burnard, P., Turner, G., 1999. Noble gas behaviour and composition in the mantle: Constraints from the Iceland plume. Earth Planet. Sci. Lett. 171, 199–207. https://doi.org/10.1016/S0012-821X(99)00143-0

Jacobsen, S.B., Heier, K.S., 1978. Rb-Sr isotope systematics in metamorphic rocks, Kongsberg sector, south Norway. Lithos 11, 257–276.

Jaret, S.J., Hemming, S.R., Rasbury, E.T., Ramezani, J., Jacobsen, S.B., 2016. The Case for an Impact at the Gardnos Impact Structure at 385 Ma, in: 79th Annual Meeting of the Meteoritical Society. p. LPI Contribution No. 1921, id.6476.

Mukhopadhyay, S., 2012. Early differentiation and volatile accretion recorded in deep-mantle neon and xenon. Nature 486, 101–104. https://doi.org/10.1038/nature11141

Schilling, J., Hanan, B.B., Mccully, B., Kingsley, R.H., 1994. Influence of the Sierra Leone mantle plume on the equatorial Mid-Atlantic Ridge: A Nd-Sr-Pb isotopic study. J. Geophys. Res. 99, 5–12.

Schilling, J.G., Ruppel, C., Davis, a N., Mccully, B., Tighe, S. a, Kingsley, R.H., Lin, J., 1995. Thermal Structure of the Mantle beneath the Equatorial Mid-Atlantic Ridge - Inferences from the Spatial Variation of Dredged Basalt Glass Compositions. J. Geophys. Res. Earth 100, 10057–10076. https://doi.org/Doi 10.1029/95jb00668

Sohn, R.A., Willis, C., Humphris, S., Shank, T.M., Singh, H., Edmonds, H.N., Kunz, C., Hedman, U., Helmke, E., Jakuba, M., Liljebladh, B., LInder, J., Murphy, C., Nakamura, K., Sato, T., Schlindwein, V., Stranne, C., Tausenfreund, M., Upchurch, L., Winsor, P., Jakobsson, M., Soule, A., 2008. Explosive volcanism on the ultraslow-spreading Gakkel ridge, Arctic Ocean. Nature 453, 1236–1238.

Sundvoll, B., Neumann, E.-R., Larsen, B.T., Tuen, E., 1990. Age relations among Oslo Rift magmatic rocks: implications for tectonic and magmatic modelling. Tectonophysics 67–87.

Weiss, D., Kieffer, B., Maerschalk, C., Pretorius, W., Barling, J., 2005. High-precision Pb-Sr-Nd-Hf isotopic characterization of USGS BHVO-1 and BHVO-2 reference materials. Geochem. Geophys. Geosyst. 6.

APPENDIX III

Supplementary Information File to Chapter 4

Materials and Methods

Analytical methods

All sample preparations and measurements were performed in the isotope laboratories at the Department of Earth and Planetary Sciences, Harvard University. Rocks were crushed in a shatter-box with a stainless steel mortar to under a 0.006 mm diameter grain size for efficiency in dissolution. 100 mg samples were digested in CEM PFA Teflon microwave vessels, first in a mixed solution of high purity HF-HNO_3 and then in a mixture of high purity H_2O-HCl-HNO_3, at 180ºC for one hour. Each step was followed by dry down. The resulting residue was dissolved in 1 N HNO_3 for ion exchange column chemistry and major and trace element analyses. Cation exchange chromatography was performed on an aliquot to separate and purify Mg using Bio-Rad AG50W-X8 resin. The sample aliquot was passed through the column twice to eliminate elements of interference. Pure Mg solutions were dried down and re-dissolved in 2% HNO_3 for elemental and isotopic measurements. Another small aliquot from the 1N HNO_3 solution was for major and trace elemental analyses using an iCAP RQ mass spectrometer (Thermo Scientific Quadrupole ICPMS). Isotopic analysis was performed with a Nu Plasma II MC-ICPMS in low resolution mode. Magnesium isotope ratios were measured using wet analysis procedures and the standard-sample bracketing method. The results are reported in δ notation (‰), where $\delta^{X}Mg = [(^{X}Mg/^{24}Mg)_{sample}/(^{X}Mg/^{24}Mg)_{standard} - 1] \times 1000$, x can be 25 or 26. The Mg standard is DSM3, a solution made from pure Mg metal

(Galy et al., 2003). Reproducibility of Mg isotopic measurements is better than ±0.03‰ (2σ) for the methods used in this study.

Supplementary Text

Summary of Results

Our measurements show that the samples to have low SiO_2 contents (35.5–40.0 %), high contents of MgO (7.13–12.68%), TiO_2 (3.87–4.57%), moderate to high total alkalis of Na_2O + K_2O (3.51–8.35%), and CaO contents of 14.3–20.5%. Following nomenclature(Le Bas, 1989), the samples are classified as melilitites. The concentrations of compatible elements, such as Ni, range from 91 to 223 ppm, while those of Cr range from 25 to 562 ppm. La/Yb_N ratios are very high (39.4–46.5). The data generally lie on the Mg isotope mass fractionation line (**Fig. S1**).

The $\delta^{26}Mg$ values in the five samples span from -0.362 to -0.300, with an average of -0.319 (**Table 1**). The $\delta^{26}Mg$ values of the samples are on average, marginally lower than the $\delta^{26}Mg$ of the normal peridotitic mantle (-0.25 ± 0.07‰). Gd/Yb (concentration) ratios based on measurements are calculated to range from 8.1 to 9.8, similar to those reported from kimberlites (Becker and Le Roex, 2006). Bulk silicate Earth (BSE) normalized Gd/Yb_N ratios range from 6.5 to 7.3, an extreme in comparison to the New Zealand intraplate lavas(Wang et al., 2016), and alkali basalts from the West Qinling orogeny (Dai et al., 2017).

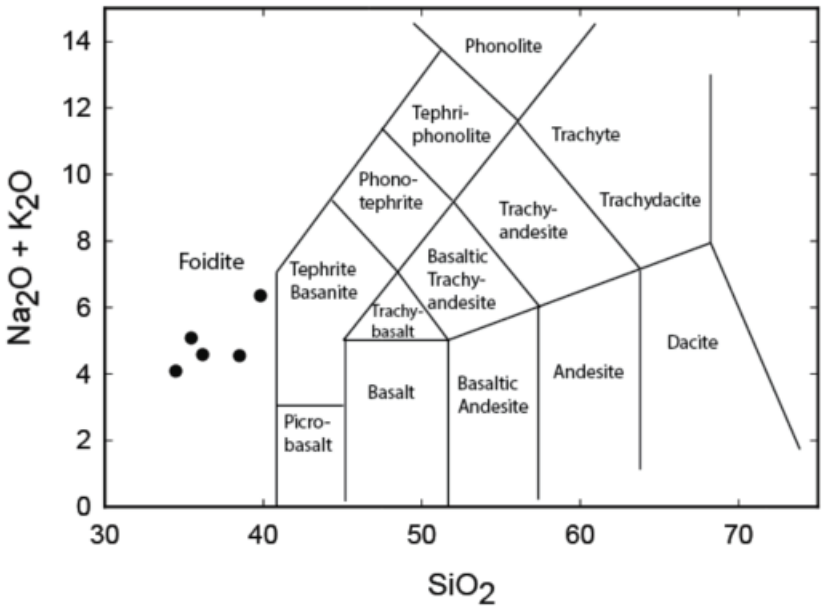

Fig. S1. Plot of sample compositions with respect to the IUGS classification. The samples can be classified as melilitites (Le Bas, 1989).

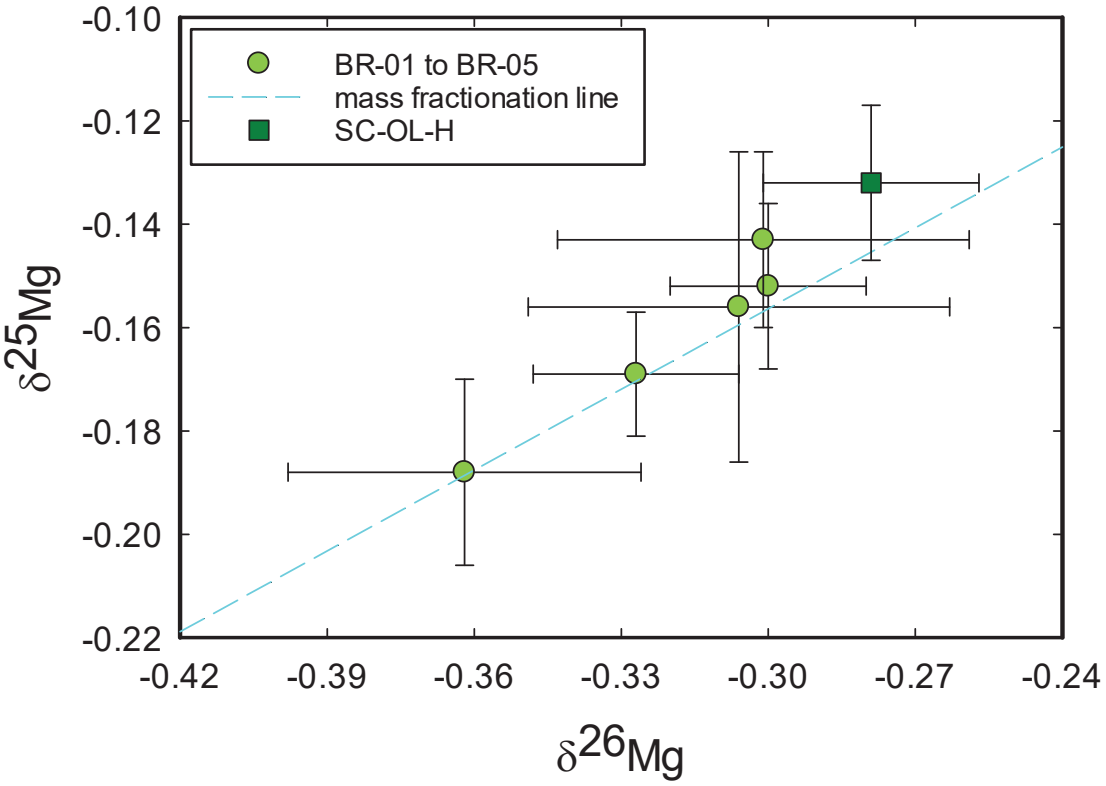

Fig. S2. Measurements of Mg isotopes for BR-01 through BR-05 (green circles), compared with San Carlos Olivine (green square – SC-OL-H). The samples and SC-OL-H are shown to plot close to a mass fractionation line (diagonal blue broken line) with a slope of 0.521 (Young and Galy, 2004). Error bars are 2σ.

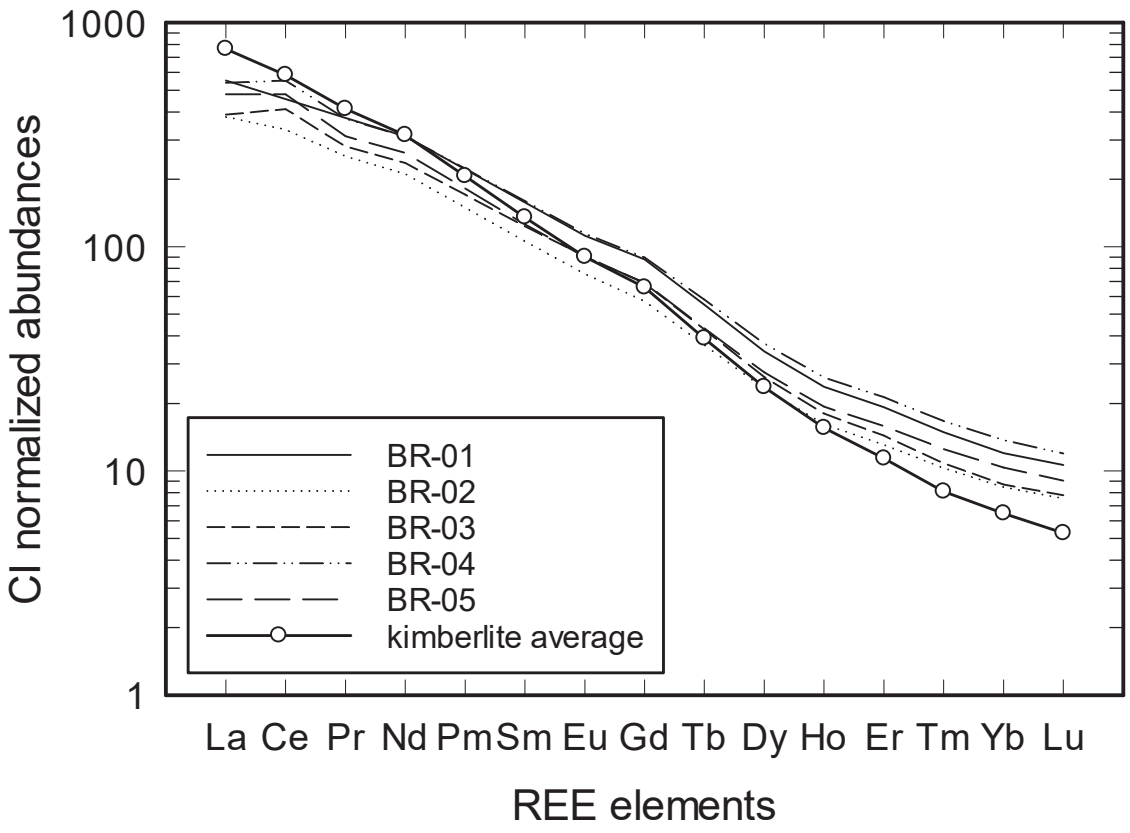

Fig. S3. REE plots of the Brunlanes basalts. All samples show extreme REE fractionation, similar to the Group I on-craton kimberlite average (Becker and Le Roex, 2006).

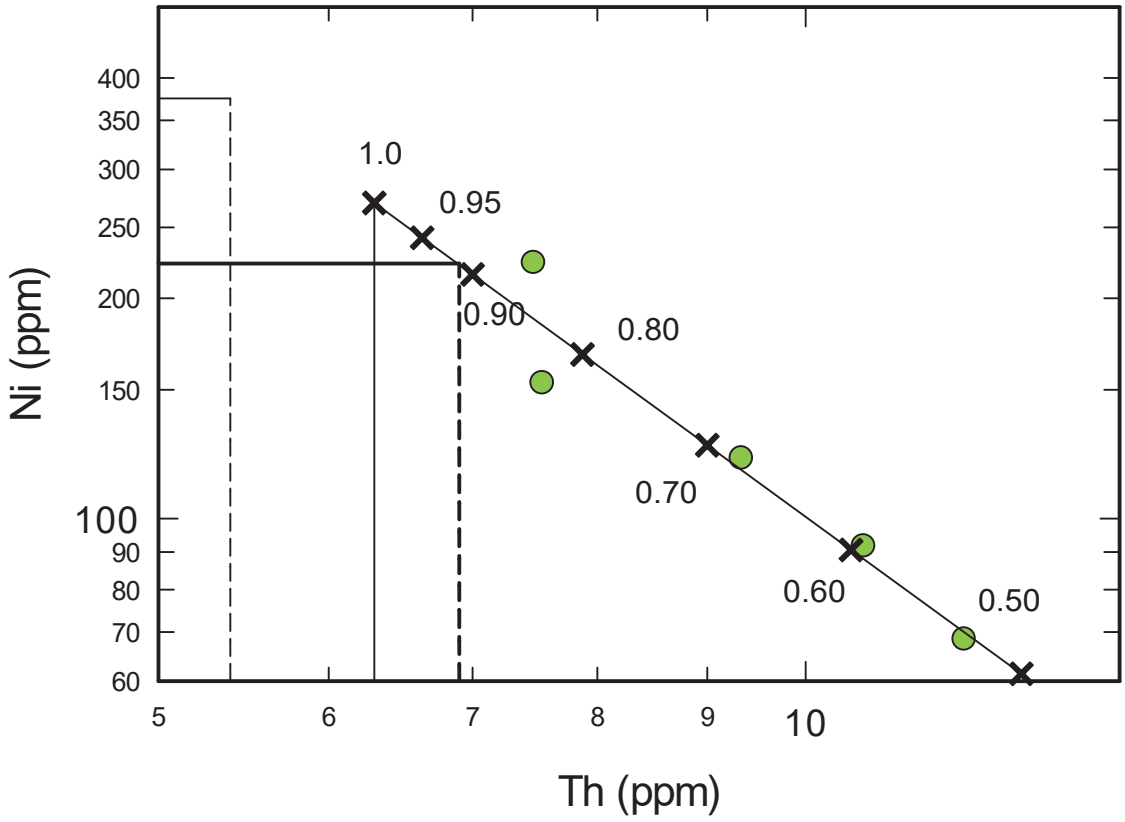

Figure S4. Measured Ni and Th concentrations (ppm) for the Brunlanes basalts plotted on a log-log scale. Plotted together with the data (line with crosses) are modeled melts with varying degrees of remaining fraction of liquid, using a Rayleigh fractional crystallization model that runs through the best fit line, derived using least-squares linear regression through the data. The numbers from the top left to bottom right in the plot (1.0 to 0.50) indicate the modeled remaining fraction of liquid. The two dotted vertical lines bracket a range of Th concentrations possible in the source magma, where the upper bound (in bold) is constrained by the concentration of Ni in the sample with the highest concentration. The vertical solid line indicates the initial Th concentration chosen for the model. The Ni vs Th plot supports the notion that the Ni concentrations evolved during the fractional crystallization of a partially melt from the peridotitic mantle. The relationship deduced from this fractionation model suggests that BR-02 must have been the most primitive of the Brunlanes samples, with BR-04 being the least primitive in development. Least squares linear fitting to the data yields a slope of –2.14 and a *y*-intercept of 4.14, with 1σ uncertainties of 0.365 and 0.354, respectively.

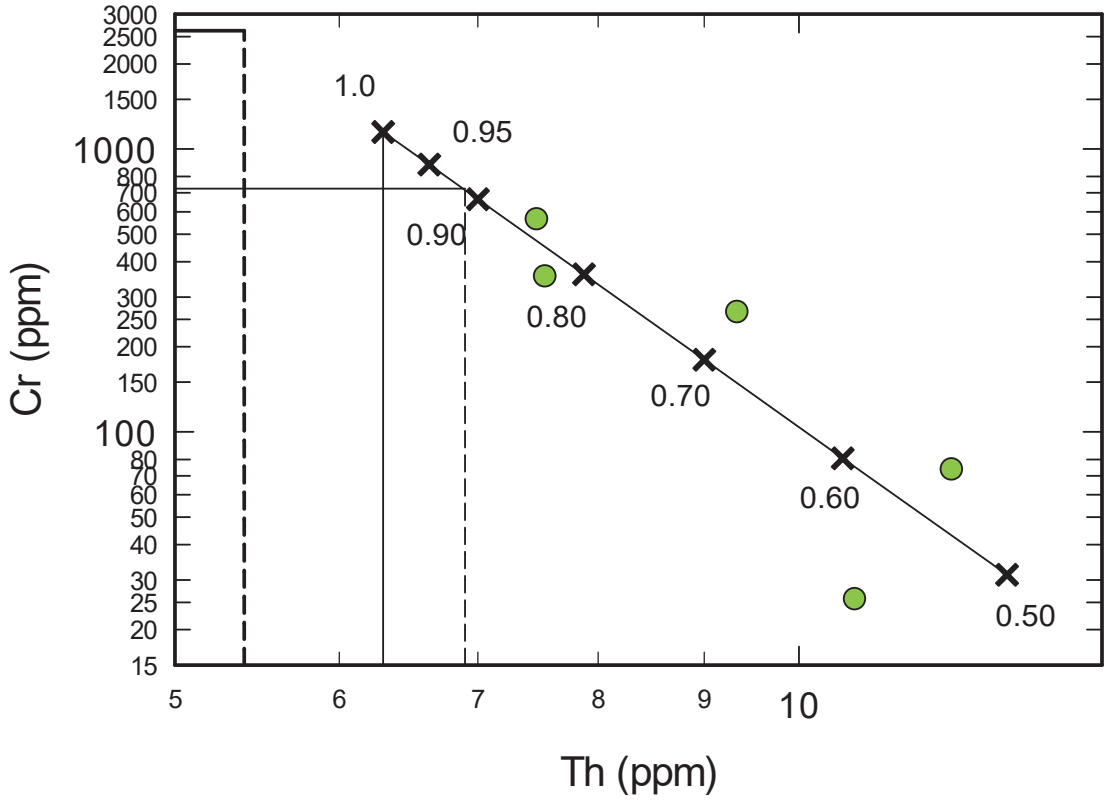

Fig. S5. Measured Cr and Th concentrations (ppm) for the Brunlanes basalts plotted on a log-log scale. Plotted with the data (line with crosses) are modeled melts with varying degrees of remaining fraction of liquid using a Rayleigh fractional crystallization model that runs through the best fit line, derived using least-squares linear regression through the data. The numbers near the crosses from the top left to bottom (1.0 to 0.50) indicate the degree of remaining fraction of liquid. The two dotted vertical lines bracket a calculated range of Th concentrations possible in the source magma, where the lower bound (in bold) is constrained by the concentration of Cr in the Bulk Silicate Earth (McDonough and Sun, 1995). The Cr vs Th plot exhibits a similar trend to the Ni vs Th plot, reflecting the common fractional crystallization process involved in the evolution of Ni and Cr element concentrations. Least squares linear fitting to the data reveal a slope of –5.20 and a *y*-intercept of 7.22, with 1σ uncertainties of 1.93 and 1.87, respectively.

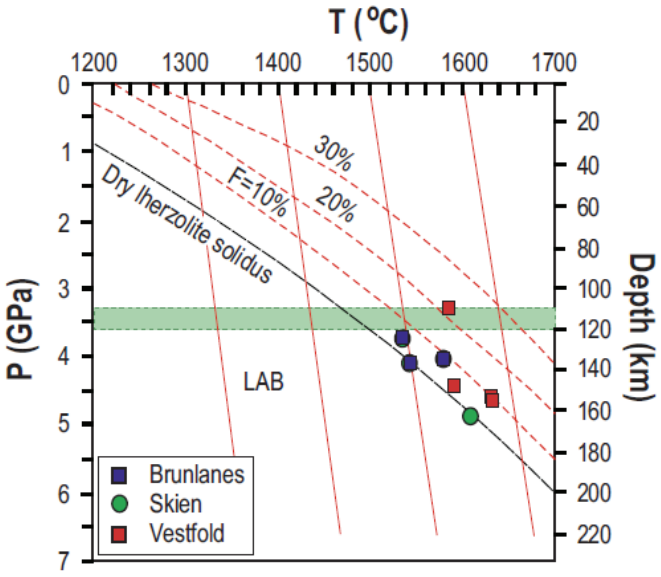

Fig. S6. Temperatures and pressures calculated for basalts from Brunlanes (B1) in the southern part of the Oslo Graben, based on data (Neumann et al., 2002; *Neumann, unpublished data*), on the basis of the thermobarometer utilized (Lee et al., 2009), based on whole rock compositions. Basalt compositions for the Brunlanes basalts are represented by data from another study, as the barometer cannot be used for strongly silica-undersaturated rocks (SiO_2 <43 wt%), as the ones analyzed in the study. The results suggest a pressure of origin of 3.7–4.1 GPa and temperatures in the range 1540–1580 ºC to a first degree, supporting the notion of a deep-seated origin for the Brunlanes melilitites. The Brunlanes samples overlap with data on SiO_2-undersaturated rocks from the nearby Skien area. The thermobarometer estimates primary magma compositions by assuming pure olivine fractionation at low pressures to an olivine composition of Fo_{90}.The basaltic rocks for which *P* and *T* is estimated should therefore have MgO > 9.0 wt%. fO_2 is taken to be close to the fayalite-magnetite-quartz (FMQ) buffer. Underestimating fO_2 gives over-estimated temperatures (Lee et al., 2009). Lherzolite solidus and melt percent isopleths (F) (Katz et al., 2003) are indicated on this plot. Data on the Oslo Rift indicates that also high TiO_2 contents (>>3.0) may give over-estimated temperatures and pressures. LAB: Lithosphere-Asthenosphere Boundary, based on tomographic data (Kolstrup et al., 2015; Maupin et al., 2013). Red solid lines correspond to isentropic melting adiabats.

Table S1. Compositions

Concentrations in ppm Element	BR-01	BR-02	BR-03	BR-04	BR-05
Li	6.44	4.67	9.67	7.26	6.73
Be	2.54	1.96	2.15	2.65	2.37
B	18.0	17.1	5.65	27.5	21.4
O	396222	391475	391894	386388	405193
Na	8071	16742	12066	5346	28954
Mg	42982	76473	61297	51157	59292
Al	40008	45712	42122	43927	57460
Si	180556	161212	169373	165910	186903
P	11243	4128	5906	5804	5132
K	29290	15645	25116	36909	21415
Ca	142862	138905	123658	146335	102246
Sc	19.8	41.1	31.5	24.5	21.7
Ti	27393	26029	34343	28553	23179
V	531	492	607	412	409
Cr	25.5	562	353	73.4	264
Mn	2426	1865	2120	2694	2113
Fe	113474	116335	126323	121359	102292
Co	52.9	72.0	62.5	55.9	56.8
Ni	91.6	223.5	153.1	68.4	120.8
Cu	162	122	103	128	132
Zn	190	560	177	205	197
Ga	30.8	24.2	29.2	29.7	26.1
Ge	5.59	3.76	4.47	5.32	4.44
As	2.84	1.59	2.03	2.60	1.93
Rb	54.8	25.3	55.8	84.0	40.7
Sr	1930	1468	2192	1692	2135
Y	34.8	23.6	24.4	35.2	25.9
Zr	534	332	453	672	393
Nb	147	241	113	170	306
Mo	0.778	0.86	0.418	0.346	0.509
Ag	0.133	0.085	0.115	0.178	0.098
Cd	0.161	0.105	0.105	0.196	0.089
Sn	3.373	3.45	3.738	3.602	3.319
Sb	0.150	0.136	0.143	0.137	0.193
Cs	0.885	0.586	0.838	0.863	0.583
Ba	934	763.9	831	1160	990
La	131	90.2	92	128	114
Ce	280	204.8	253	339	294

Pr	34.9	23.47	25.9	34.6	28.9
Nd	142	96.34	108	142	120
Sm	23.3	15.66	18.2	23.7	18.6
Eu	6.30	4.26	5.10	6.44	5.08
Gd	17.47	11.36	13.65	17.80	13.72
Tb	1.99	1.31	1.54	2.09	1.56
Dy	8.40	5.73	6.45	9.09	6.76
Ho	1.30	0.88	0.98	1.42	1.06
Er	3.08	2.09	2.30	3.41	2.53
Tm	0.368	0.254	0.267	0.411	0.309
Yb	1.93	1.36	1.40	2.21	1.66
Lu	0.261	0.185	0.192	0.294	0.223
Hf	10.03	8.01	10.58	13.73	8.74
Ta	9.26	10.32	9.26	11.18	16.86
W	0.825	0.29	0.335	0.593	0.421
Au	0.0112	0.0120	0.0107	0.0129	0.0191
Tl	0.0398	0.0148	0.0393	0.0463	0.0279
Pb	6.90	5.71	4.39	5.08	6.44
Bi	0.0275	0.0236	0.0287	0.0298	0.0258
Th	10.65	7.48	7.55	11.86	9.34
U	3.78	4.30	3.86	3.83	11.11
Total	1000000.00	1000000.00	1000000.00	1000000.00	1000000.00

Concentrations of oxides in weight percent

wt %	**BR-01**	**BR-02**	**BR-03**	**BR-04**	**BR-05**
SiO_2	38.63	34.49	36.23	35.49	39.98
MgO	7.13	12.68	10.16	8.48	9.83
FeO	14.60	14.97	16.25	15.61	13.16
Al_2O_3	7.56	8.64	7.96	8.30	10.86
CaO	19.99	19.44	17.30	20.48	14.31
Cr_2O_3	0.00	0.08	0.05	0.01	0.04
TiO_2	4.57	4.34	5.73	4.76	3.87
MnO	0.31	0.24	0.27	0.35	0.27
Na_2O	1.09	2.26	1.63	0.72	3.90
K_2O	3.53	1.88	3.03	4.45	2.58
P_2O_5	2.58	0.95	1.35	1.33	1.18
NiO	0.01	0.03	0.02	0.01	0.02
CoO	0.01	0.01	0.01	0.01	0.01
Total	100.00	100.00	100.00	100.00	100.00

Table S2. Parameters used in fractional crystallization modeling

	Th	Ni	Cr
D	0	3.14	6.2
Initial concentrations C^0 (ppm)	6.3	270	1150

The D values for the Ni and Th are determined assuming $D_{Th} = 0$. Initial concentrations (C^0) are estimates, chosen to simultaneously reproduce the y-intercepts of the plots. Concentrations are calculated using the Rayleigh fractionation law: $C_l = C^0_l F^{(D-1)}$, where F is the fraction of residual melt, D is the bulk partition coefficient, C^0_l the initial concentration, and C_l the concentration of the residual liquid. Considering the Bulk Silicate Earth value (McDonough and Sun, 1995) of Cr (2625 ppm) and the Ni content of a sample with the highest concentration (223 ppm) as constraints, the initial magma is found to have Th in the range 5.4 to 6.9 ppm; we chose 6.3 ppm for our calculations. The Th concentrations (with D=0) leads to a degree of mantle melting of 1.3 % to produce the primary magma.

Geology and Samples

Melilitites, nephelinites and basanites are the most Si-undersaturated basaltic rocks in the Carboniferous-Permian Oslo Rift in SE Norway. The rift is a continental rift structure striking N-S through the Precambrian crust of the Baltic Shield. The long-lived magmatism and high volcanism lasted from latest Carboniferous to the end of Permian, about 60 million years (Larsen et al., 2008; Sundvoll et al., 1990).

The tectono-magmatic development of the rift is divided into six stages, with magmatism in all six stages. Volcanism on the other hand are only found in stage 2, 3 and 4. Volcanism in these three stages were different both petrologically and volcanologically and were also distributed different throughout the rift. Both basaltic, intermediate and felsic volcanism occurred. Stage 2 named "The initial rift and first basaltic volcanism". All volcanism during this stage were basaltic, varying from the most Si-undersaturated to tholeiitic, and occurred in the southern part of the rift. Most of the basalts during this stage were however, alkali olivine basalts(Neumann et al., 2002, 1990), and locally exceeding 1 km of stratigraphic thickness banking up against the eastern master fault (Schou-jensen and Neumann, 1988). The undersaturated nephelinites and melilitites in Brunlanes and Skien in the SW were formed during this stage.

The melilitites/nephelinites in this study were formed during stage 2, in the southern part of the Oslo Rift, and are the oldest volcanic rocks erupted during an early stage of the rift formation (Corfu and Dahlgren, 2008). The five samples analyzed are all from the Brunlanes basalt area in Vestfold. The samples are in stratigraphical order from the lowest BR-01, BR-

02, BR-05, BR-03 and the uppermost BR-04, covering about 600 m of the total 800 m Brunlanes basalt stratigraphy (Corfu and Dahlgren, 2008).

***P-T* estimates**

We have derived independent estimates for temperatures and pressures of origin for the primary melts that gave rise to basaltic rocks in the Oslo Graben, using a thermobarometer (Lee et al., 2009). The results are shown in **Fig. S5**. A series of limitations (Lee et al., 2009) to the use of this thermobarometer is as follows:

- Because the thermobarometer estimates primary magma compositions by assuming pure olivine fractionation at low pressures, the basaltic rocks for which P and T are to estimated should have MgO>9.0 wt%.
- fO_2 is taken to be close to the fayalite-magnetite-quartz (FMQ) buffer. Underestimating fO_2 gives over-estimated temperatures.
- The barometer cannot be used for silica-undersaturated rocks, and can therefore not be used for nephelinites or other strongly silica-undersaturated rocks with SiO_2 less than about 43 wt%.

The uncertainty for barometry is ±0.20 GPa (Lee et al., 2009), and uncertainties in temperature of ± 3%, corresponding to ~40º for a temperature of 1400 ºC.

A large proportion of the Brunlanes basalts of the B1 unit in the Oslo Graben has MgO <9.0 wt%, some have SiO_2 <43 wt%. Therefore the thermobarometer of (Lee et al., 2009) could only be used on a minority of the samples. An additional problem seems to be associated with high TiO_2 concentrations. With very few exceptions the basaltic lavas on which the thermobarometer of (Lee et al., 2009), is based have TiO_2 <3.0. wt%). Estimated

temperatures and pressures for high-Ti rocks show a rough positive correlation between TiO_2 and pressure, and, in spite of some scatter, a correlation between TiO_2 and temperature. However, the *P-T* results obtained for the Brunlanes samples (3.9-5.7 wt%) do not appear to be affected by their high TiO_2 contents.

In **Fig. S6** we show the results obtained for the Oslo B1 basalts with MgO >9 wt%, SiO_2 >43 wt%. The Skien B1 basalts cover a *P-T* range of 3.7-4.9 GPa and 1540-1610 ºC (**Fig. S5**), and fall on, or close to the dry lherzolite solidus, indicating <10% melting. The two basalts from Vestfold give a lower pressure, ~3.3 GPa, and temperatures of 1520 and ca. 1590 ºC, that suggests ~10 to ~22% partial melting.

Based on tomographic data from the TopoScandiaDeep (part of the TOPOEUROPE study) the present day depth of the lithosphere-asthenosphere boundary (LAB) is suggested to increase from ~120 km beneath the western part of the Oslo Graben, to about 200 km beneath the Proterozoic basement east of the rift (Kolstrup et al., 2015; Maupin et al., 2013).

References

Becker, M., Le Roex, A.P., 2006. Geochemistry of South African on- and off-craton, group I and group II kimberlites: Petrogenesis and source region evolution. J. Petrol. 47, 673–703. https://doi.org/10.1093/petrology/egi089

Corfu, F., Dahlgren, S., 2008. Perovskite U-Pb ages and the Pb isotopic composition of alkaline volcanism initiating the Permo-Carboniferous Oslo Rift. Earth Planet. Sci. Lett. 265, 256–269. https://doi.org/10.1016/j.epsl.2007.10.019

Dai, L.-Q., Zhao, Z.-F., Zheng, Y.-F., An, Y.-J., Zheng, F., 2017. Geochemical Distinction between Carbonate and Silicate Metasomatism in Generating the Mantle Sources of Alkali Basalts. J. Petrol. 58, 863–884. https://doi.org/10.1093/petrology/egx038

Galy, A., Yoffe, O., Janney, P.E., Williams, R.W., Cloquet, C., Alard, O., Halicz, L., Wadhwa, M., Hutcheon, I.D., Ramon, E., Carignan, J., 2003. Magnesium isotope heterogeneity of the isotopic standard SRM980 and new reference materials for magnesium-isotope-ratio measurements. J. Anal. At. Spectrom. 18, 1352. https://doi.org/10.1039/b309273a

Katz, R.F., Spiegelman, M., Langmuir, C.H., 2003. A new parameterization of hydrous mantle melting. Geochemistry, Geophys. Geosystems 4, 1–19. https://doi.org/10.1029/2002GC000433

Kolstrup, M.L., Hung, S.H., Maupin, V., 2015. Multiscale, finite-frequency P and S tomography of the upper mantle in the southwestern Fennoscandian Shield. Geophys. J. Int. 202, 190–218. https://doi.org/10.1093/gji/ggv130

Larsen, B.T., Olaussen, S., Sundvoll, B., Heeremans, M., 2008. The permo-Carboniferous Olso Rift through six stages and 65 million years. Episodes 31, 52–58.

Le Bas, M.J., 1989. Nephelinitic and basanitic rocks. J. Petrol. 30, 1299–1312. https://doi.org/10.1093/petrology/30.5.1299

Lee, C.T.A., Luffi, P., Plank, T., Dalton, H., Leeman, W.P., 2009. Constraints on the depths and temperatures of basaltic magma generation on Earth and other terrestrial planets using new thermobarometers for mafic magmas. Earth Planet. Sci. Lett. 279, 20–33. https://doi.org/10.1016/j.epsl.2008.12.020

Maupin, V., Agostini, A., Artemieva, I., Balling, N., Beekman, F., Ebbing, J., England, R.W., Frassetto, A., Gradmann, S., Jacobsen, B.H., Köhler, A., Kvarven, T., Medhus, A.B., Mjelde, R., Ritter, J., Sokoutis, D., Stratford, W., Thybo, H., Wawerzinek, B., Weidle, C., 2013. The deep structure of the Scandes and its relation to tectonic history and present-day topography. Tectonophysics 602, 15–37. https://doi.org/10.1016/j.tecto.2013.03.010

McDonough, W., Sun, S. -s., 1995. The composition of the Earth. Chem. Geol. 120, 223–253. https://doi.org/10.1016/0009-2541(94)00140-4

Neumann, E.R., Dunworth, E.A., Sundvoll, B.A., Tollefsrud, J.I., 2002. B1basaltic lavas in Vestfold-Jeløya area, central Oslo rift: Derivation from initial melts formed by progressive partial melting of an enriched mantle source. Lithos 61, 21–53. https://doi.org/10.1016/S0024-4937(02)00068-3

Neumann, E.R., Sundvoll, B., Øverli, P.E., 1990. A mildly depleted upper mantle beneath southeast Norway: evidence from basalts in the Permo-Carboniferous Oslo Rift. Tectonophysics 178, 89–107. https://doi.org/10.1016/0040-1951(90)90461-G

Schou-jensen, E., Neumann, E.-R., 1988. Volcanic rocks on Jeløya, central Oslo Region: the mafic lavas. Nor. Geol. Tidsskr. 68, 289–308.

Sundvoll, B., Neumann, E.-R., Larsen, B.T., Tuen, E., 1990. Age relations among Oslo Rift magmatic rocks: implications for tectonic and magmatic modelling. Tectonophysics 67–87.

Wang, S.J., Teng, F.Z., Scott, J.M., 2016. Tracing the origin of continental HIMU-like intraplate volcanism using magnesium isotope systematics. Geochim. Cosmochim. Acta 185, 78–87. https://doi.org/10.1016/j.gca.2016.10.009

Young, E.D., Galy, A., 2004. The Isotope Geochemistry and Cosmochemistry of Magnesium. Rev. Mineral. Geochemistry 55, 197–230. https://doi.org/10.2138/gsrmg.55.1.197

APPENDIX IV

Code documentation for Chapters 3 and 5

The following Matlab codes have been written by Gang Yu, and modified slightly by Eugenia Hyung, to simulate the homogenization of the enriched and depleted isotopic reservoirs and sampling process:

Earth.m

sampling.m

Calculations can be performed by changing numerical values for initial conditions. After saving the codes under the same folder, calculations can be run typing "Earth" into the Matlab command window. Each set of codes should be saved as separate files. The code is designed to calculate results for the different sampled isotopic compositions of the reservoirs according to length scale of sampling, sampling number, and sampling time intervals. "Earth_m.m" is a modified version of "Earth.m" to better incorporate two different mixing rates throughout the history of the Earth. Results may be plotted by typing commands such as "plot(tAll1,ewm,'b.')" into the command window. Additional utility codes for plotting may be found by contacting Eugenia Hyung.

Earth.m

```
% By Gang Yu
 clear all;
global ewm nsam volm2 volm
```

```
% parameters
deltaT = 4567;  % time for convection (Myr)
nsam = 1000; % change number of samples per time step here

% initial state
r = 6371; %km.. radius of the (target) planet   6371 is the
radius of the Earth in units of km.
rc = 6371-2890; %r*0.6; %km..radius of the planet's core;
"2890" is the depth of the mantle in km
l03 = sqrt(1-(1-(rc/r)^2)*44/136)*r-rc; % upper mantle
depth (km)
l02 =r-rc-l03;  % lower mantle depth (km)
% volume
volp = 4/3*pi*r^3;  % volume of the planet
volc = 4/3*pi*rc^3;  % volume of planet's core
volm = volp-volc;  % volume of planet's mantle
volm2 = volp - 4/3*pi*(r-l02)^3; % volume of upper mantle
%volm3 = volm - volm2;

ew2 = 1;%2.23; initial epsilon(W or Nd) value of reservoir
"2", where 2 in this case is the upper mantle
cw2 = 0.055;%4; initial W or Nd concentration of reservoir
"2"
ew3 = 5;%.15; initial epsilon(W or Nd) value of reservoir
"3", where 3 indicates the lower mantle
cw3 = 0.01; %8; initial W or Nd concentration of reservoir
"3"

% predefining dimensions of variables for code to run
faster:
cwm = zeros(1,nsam);
samples = zeros(3,nsam);
massf = zeros(1,nsam);


tt = 4; %Ga $time at which mixing rate is set to change
taoAll = [500,500]; % mixing rates of mantle for 4.57 Ga -
tt, and 0 to tt, respectively. The code is intended to be
able to incorporate two different mantle mixing rates
consecutively.

%taoAll = [500, 1000, 1500, 2000, 2500]; % mantle
convection rate (Myr-1)
%tao = 500;
```

```
%n = length(taoAll);
%ewm = zeros(n,nsam);


%ls0All = [1, 3, 10, 30, 100, 300]; % sampling size
ls0 = 100; % length scale of sampling
%n = length(ls0All);
%ewm = zeros(n,nsam);


tAll =  [0,67:100:4567]; % produces a vector consisting of
47 numbers including 0, then 67 (Ma) to (4567) Ma in 100
Myr increments
tAll1 = fliplr(tAll)/1000; % tAll flipped to decrease
monotonically in units of Gyr

% predefining dimensions for code to run faster:
n = length(tAll);
ewm = zeros(nsam,n);
lt2 = zeros(1,n);
lt3 = zeros(1,n);

temp =0;

for j = 1:n

%Convection


%tao = taoAll(j);
%ls0 = ls0All(j);
t = tAll(j);


if t<=4567-tt
tao = taoAll(1);

%Reduction of mantle heterogeneity by convection, assuming
exponential decay of the length scale of heterogeneities
due to toroidal motion :
lt2(j) = l02*exp(-t/tao);
lt3(j) = l03*exp(-t/tao);

else
    if temp ==0
```

```
        l02 = lt2(j-1);
        l03 = lt3(j-1);
        temp = 1;
    end
    tao = taoAll(2);
    lt2(j) = l02*exp(-(t-4567+tt)/tao);
    lt3(j) = l03*exp(-(t-4567+tt)/tao);
end


% Sampling


% sampling
samples = sampling(ls0, lt2(j), lt3(j));
% This line calls in the sampling function. Earth.m and
sampling.m must be in the same file for "Earth.m" to run.

% mixing

massf = samples(3,:);

% calculation of the total concentration of W or Nd of
sampling box (for however many samples[=nsam] per time
step):
cwm = cw2.*massf + cw3.*(1-massf);
% calculation of the resulting epsilon values [nsam] for
each time step:
ewm(:,j) = ew2*cw2./cwm.*massf + ew3*cw3./cwm.*(1-massf);



end
```

---

sampling.m

```
function samples = sampling(ls0, lt2, lt3 )

%   The sampling algorithm is outlined in Jacobsen and Yu
(2015).
```

```
 global nsam volm2 volm

samples = zeros(3,nsam);

for i = 1:nsam

    ls = ls0;
    vm2 = volm2;
    vm = volm;
    samples2 =0;
    samples3 = 0;

    p2 = vm2/vm;
    %p3 = 1-p2;

        nsmax = min(ls^3/lt2^3,ls^3/lt3^3);

    while nsmax > 500
        nsampling =nsmax - 499;
        samples2 = nsampling*p2;
        samV2 = samples2*lt2^3;
        vm2 = vm2 - samV2;

        samples3 = nsampling-samples2;
        samV3 = samples3*lt3^3;

        vm = vm - samV2-samV3;
        ls =(ls^3-samV2-samV3)^(1/3);

        nsmax = min(ls^3/lt2^3,ls^3/lt3^3);

        samples(1,i) = samples(1,i) + samples2;
        samples(2,i) = samples(2,i) + samples3;
        samples2 = 0;
        samples3 = 0;

    end



    while nsmax > 10
         ran = rand;
```

```
      if ran < p2
          samples(1,i) = samples(1,i)+1;
          samV = lt2^3;
          vm2 = vm2 - samV;
      else
          samples(2,i)=samples(2,i)+1;
          samV = lt3^3;
      end

      vm = vm - samV;
      ls =(ls^3-samV)^(1/3);
      nsmax = min(ls^3/lt2^3,ls^3/lt3^3);
end

while (ls>0)

    %probability
    p2 = vm2/vm;
    %p3 = 1-p2;


    pin2 = abs((ls-lt2)^3/((ls+lt2)^3));
    %pedge2 = 1 - pin2;
    %pout = 1-pin-pedge;
    pin3 = abs((ls-lt3)^3/((ls+lt3)^3));
    %pedge3 = 1 - pin3;


    r1 = rand;
    if r1<=p2  % upper mantle
        if ls>=2*lt2
            samples2 = 1;
        else
            r2 = rand;
            if r2 <=pin2;
                samples2=1;
            else
                 samples2=rand;
            end
        end

        samV =lt2^3*samples2;

        if ls^3<samV
```

```
                samV =ls^3;
                samples2 = samV/lt2^3;
            end
            vm2 = vm2 - samV;

        else
            if ls>=2*lt3
                samples3 = 1;
            else

                r2 = rand;
                if r2 <=pin3;
                    samples3=1;
                else
                    samples3=rand;
                end

            end

            samV =lt3^3*samples3;

            if ls^3<samV
                samV =ls^3;
                samples3 = samV/lt3^3;
            end

        end

        vm = vm - samV;
        ls =(ls^3-samV)^(1/3);

        samples(1,i)=samples(1,i)+samples2;
        samples(2,i)=samples(2,i)+samples3;

        samples2 = 0;
        samples3 = 0;

    end

    samples(3,i)=samples(1,i)/(samples(1,i)+samples(2,i));



end
```

```
end
```

The following code, "Earth_m.m" is modified from Earth.m to better incorporate two different consecutive mixing rates into calculating the homogenization and sampling of the enriched and depleted reservoirs via mantle mixing throughout time

---

```
 % By Gang Yu; modified by Eugenia Hyung
clear all;
global ewm nsam volm2 volm
% parameters
deltaT = 4567;  % time for convection (Myr)
nsam = 1000; % number of samples

% initial state
r = 6371; %km.. radius of the planet   6371
rc = 6371-2890; %r*0.6; %km..radius of the planet's core


% upper mantle, lower mantle
%%%
%%%l03 = sqrt(1-(1-(rc/r)^2)*44/136)*r-rc+131.4; % upper
mantle depth (km)
%%%l02 =r-rc-l03;  % lower mantle depth (km)
%%%

% crust, upper mantle
%%%
l03 = sqrt(1-(1-(rc/r)^2)*44/136)*r-rc+131.4; % upper
mantle depth (km)
l02 =r-rc-l03-2;  % lower mantle depth (km)
%%%

% volume
```

```
volp = 4/3*pi*r^3;  % volume of the planet
%volc = 4/3*pi*(rc)^3;  % volume of planet's core
volc = 4/3*pi*(rc)^3;  % volume of planet's core
volm = volp-volc;  % volume of planet's mantle
volm2 = volp - 4/3*pi*(r-l02)^3; % volume of upper mantle
%volm3 = volm - volm2;

%%%ew2 = -0.442;%w1;%2.23;
%%%cw2 = 2.32;%w0.055;%4;
%%%ew3 = 0.665;%w5;%.15;
%%%cw3 = 0.739;%w0.01; %8;

ew2 = -0.2;%w1;%2.23;
cw2 = 1.935;%w0.055;%4;
ew3 = 0.2;%w5;%.15;
cw3 = 0.9232;%w0.01; %8;


cwm = zeros(1,nsam);
samples = zeros(3,nsam);
massf = zeros(1,nsam);

%% Here starts the first part of the code that deals with
different mixing rates for mantle mixing
tt = 4.0; %Ga
% The two different mixing rates should be incorporated
into the code by modifying:
taoAll = [500,500];
%This part of the code (until the next "%%") is specific to
the early part of Earth's history.

%taoAll = [500, 1000, 1500, 2000, 2500]; % mantle
convection rate (Myr-1)
%tao = 500;
%n = length(taoAll);
%ewm = zeros(n,nsam);


%ls0All = [1, 3, 10, 30, 100, 300]; % sampling size
ls0 = 100;
%n = length(ls0All);
%ewm = zeros(n,nsam);
```

```
tAll =  [0,67:100:4567];
tAll1 = fliplr(tAll)/1000;

n = length(tAll);
ewm = zeros(nsam,n);
lt2 = zeros(1,n);
lt3 = zeros(1,n);

temp =0;

% change the point in time in which the mixing rate changes
by modifying the following:
a=5;
% unit of "1" is 100 Ma from 4.567 Ga ago

for j = 1:a

%Convection


%tao = taoAll(j);
%ls0 = ls0All(j);
t = tAll(j);


if t<=4567-tt
tao = taoAll(1);

%Reduction of mantle heterogeneity by convection
lt2(j) = l02*exp(-t/tao);
lt3(j) = l03*exp(-t/tao);

else
    if temp ==0
        l02 = lt2(j-1);
        l03 = lt3(j-1);
        temp = 1;
    end
    tao = taoAll(2);
    lt2(j) = l02*exp(-t/tao);
    lt3(j) = l03*exp(-t/tao);
end


% Sampling
```

```
% sampling
samples = sampling(ls0, lt2(j), lt3(j));

% mixing

massf = samples(3,:);

cwm = cw2.*massf + cw3.*(1-massf);
ewm(:,j) = ew2*cw2./cwm.*massf + ew3*cw3./cwm.*(1-massf);



end
ewm;
massf;

%% Here starts the second part of code that deals with
mixing rate for more recent times

% The two different mixing rates should be incorporated
into the code by modifying:
taoAll = [500,500];


tAll(40);

for j = a:n

%Convection


%tao = taoAll(j);
%ls0 = ls0All(j);
t = tAll(j-a+1);


if t<=4567-tt
tao = taoAll(2);
% The first number in taoAll indicates the mixing rate for
the earlier history of the Earth (from 4.567 Ga to 4.567 Ga
- a*0.1 Ga), while the second number in taoAll indicates
the mixing rate for recent history
```

```
%Reduction of mantle heterogeneity by convection
lt2(j) = lt2(a)*exp(-t/tao);
lt3(j) = lt3(a)*exp(-t/tao);

else
  %  if temp ==0
  %      l02 = lt2(j-1);
  %      l03 = lt3(j-1);
  %      temp = 1;
  %  end
    tao = taoAll(2);
    lt2(j) = lt2(a-1)*exp(-t/tao);
    lt3(j) = lt3(a-1)*exp(-t/tao);
end


% Sampling


% sampling
samples = sampling(ls0, lt2(j), lt3(j));

% mixing

massf = samples(3,:);

cwm = cw2.*massf + cw3.*(1-massf);
ewm(:,j) = ew2*cw2./cwm.*massf + ew3*cw3./cwm.*(1-massf);



end


massf

ewm;
```